Investigation of Two Dimensional Floquet Topological Insulator Using Microwave Network

Hu Wenchao

Supervisors

Prof. Shum Ping

School of Electrical & Electronic Engineering

A thesis submitted to the Nanyang Technological University
in partial fulfillment of the requirements for the degree of
Doctor of Philosophy

2017

Statement of Originality

I hereby certify that the intellectual content of this thesis is the product of my original research work and has not been submitted for a higher degree to any other University or Institution.

....

Date Hu Wenchao

Acknowledgements

During the past three and half years, I received plenty of help. At first, I would like to thank my supervisor Prof. Shum Ping for bring me into the world of research and providing me a opportunity to pursue my PhD degree in NTU. Then I would like to thank my advisor Prof. Chong Yidong for guiding me during my PhD career and introducing me into the world of open source. It is a great honor to have both of you as my mentors.

Then I would like to thank all the friends I met in Singapore. I want to say thank you to Giorgio, Qiang Bo, and Han Song for helping me a lot during my research. I am also very grateful to Li Yao, Li Ye and so on for having all the happy moment in the playground every Tuesday and Friday afternoon. More importantly, I am very happy that I met Chen Zhenghua and Chen Yi, two friends those I would like to keep in contact for my whole life.

Finally, I would like to thank my family members: my father, my mother, my sister and my girlfriend Cui Dongyao for supporting me all the time. Without anyone of you, it is impossible for me to finish my PhD. I want to say I love you.

Abstract

Topological insulators are one of the most profound discoveries in condensed matter physics during the past few decades. They are "topologically distinct" from conventional insulators, because they are insulating in the bulk while supporting metallic states on surfaces. The most extraordinary physical property of certain classes of 2D topological insulators is the existence of uni-directional transmission along the edge, which is robust to imperfections and exhibits no back-reflection. In 2005, Haldane and Raghu introduced the topological insulator concept into photonics by theoretically proposing a photonic analogue of the quantum Hall effect in photonic crystals. Wang *et al.* experimentally confirmed this idea by observing a uni-directional transmission line in a gyromagnetic photonic crystal operating in the microwave frequency range. "Topological photonics" has also been realized with resonator lattices and waveguide lattices subsequently. However, in all these experiments, edge propagation measurements serve exclusively as the proof of topological nontrivial system due to the lack of a direct analog of the Hall conductance or similar linear response-based quantity. During my PhD career, my research has focused on the investigation of two-dimensional Floquet topological insulators using microwave networks. The first part of my work involves experimentally measuring a topological edge invariant which consists of the integer winding numbers of scattering matrix eigenvalues in a microwave network. The second part of my study concerns the relation between topological edge invariants and exceptional points by introducing controllable loss and gain into the microwave network.

The network model we used to measure topological edge invariants is a two-dimensional network which is mapped into a microwave network using Laughlin's topological pump idea. The experiment setup is a two-port network system with variable phase shifters. By measuring the scattering matrix of the two-port network, we can observe the winding behavior of the eigenvalues. We implemented this experiment using microwave components at 5 GHz and successfully observed

the non-zero winding behavior for non-trivial topological system and zero winding behavior for trivial topological system, as predicted by theoretical arguments but never previously found in an experiment.

Due to the existence of loss, the system we used to measure topological edge invariants is non-Hermitian; furthermore, in the standard theory of the topological pump, we can never observe rigorously non-zero winding in a finite system, since there is always a gap in the projected band structure. Moreover, non-Hermitian effects introduce the novel physical feature of exceptional points into the band-structure which is easy to study by introducing controllable loss and gain into our experiment setup. Hence, we re-implemented our experiment setup at 900 MHz and added digital variable attenuators into the system. By controlling gain and loss, we demonstrate, theoretically and experimentally, a direct relationship between a Hermitian topological invariant and exceptional point winding numbers.

In summary, my PhD research has concentrated on the investigation of two dimensional Floquet topological insulators using microwave networks. Two major works have been finished, one is the experimental measurement of topological edge invariants in the form of scattering matrix eigenvalue winding numbers in a microwave network. The other is theoretically and experimentally proving the relation between Hermitian topological invariant and exceptional point winding numbers.

Contents

List of Figures

List of Tables

Chapter 1

Introduction

1.1 Mathematical topology

In mathematics, topology is a field which studies the unchanged properties of space under continuous deformations. The term *topology* was first introduced by Johann Benedict Listing in 19th century, the idea of topological space was formed a century later, and topology developed into a major branch of mathematics at the middle of the 20th century [1].

Topology is one of the most fundamental ideas of mathematics and it appears in almost every branch of mathematics. The motivation behind topology is that some geometric problems are determined by the way how the objects connect rather than the exact shape of the objects. In 17th century, Leonhard Euler wrote a paper

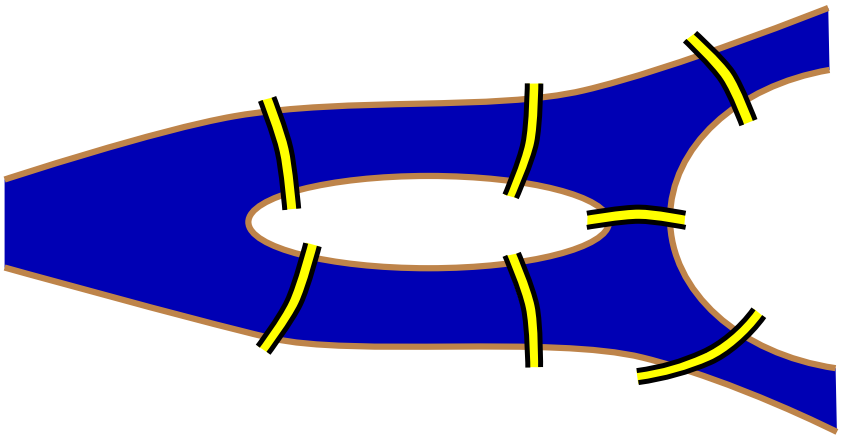

FIGURE 1.1: Schematic map of seven bridges problem.

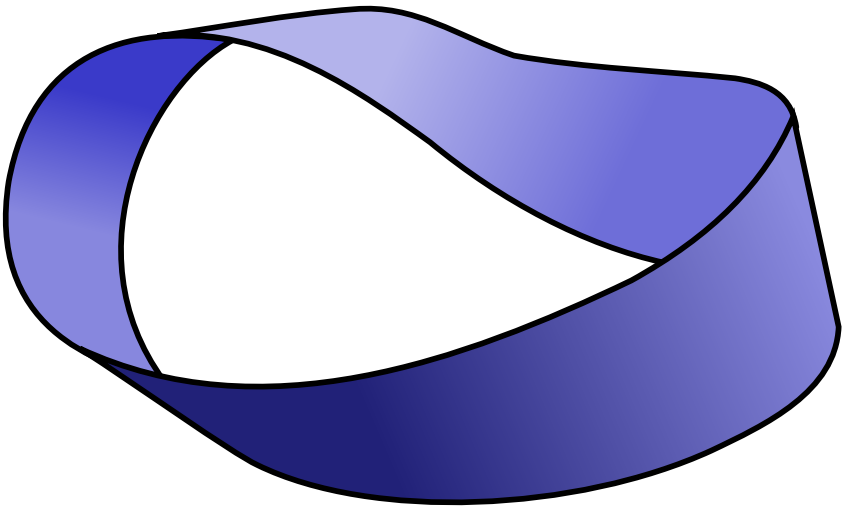

FIGURE 1.2: Mobius strip is a surface with only one boundary and only one side.

to investigate a famous problem — the *Seven Bridges of Königsberg*. This paper demonstrated that there is no route which can cross each of the seven bridges in the town of Königsberg exactly once. Fig. 1.1 shows the schematic map of Königsberg. The significant feature of this problem is that the solution is determined only by connectivity properties rather than anything else such as the lengths of the bridges. Another famous example in topology is the Möbius strip, as shown in Fig. 1.2, which has only one boundary and only one surface. All these interesting phenomena lead us into the wonderful world of mathematical topology.

The most important topics of topology research are general topology (dealing with the basic set-theory definitions and constructions), algebraic topology (searching for algebraic invariants using tools from abstract algebra), differential topology (studying differentiable functions on differentiable manifolds), and geometric topology (focusing on low-dimensional manifolds and their interaction with geometry). Topology research has wide applications in various fields such as biology, computer science, physics, and robotics.

1.1.1 Topological invariants

A topological invariant is a property of a topological space which is invariant under continuous transformation. Here, I will use the three dimensional surface in Fig. 1.3 to explain the concept of topological invariant. In this topological space,

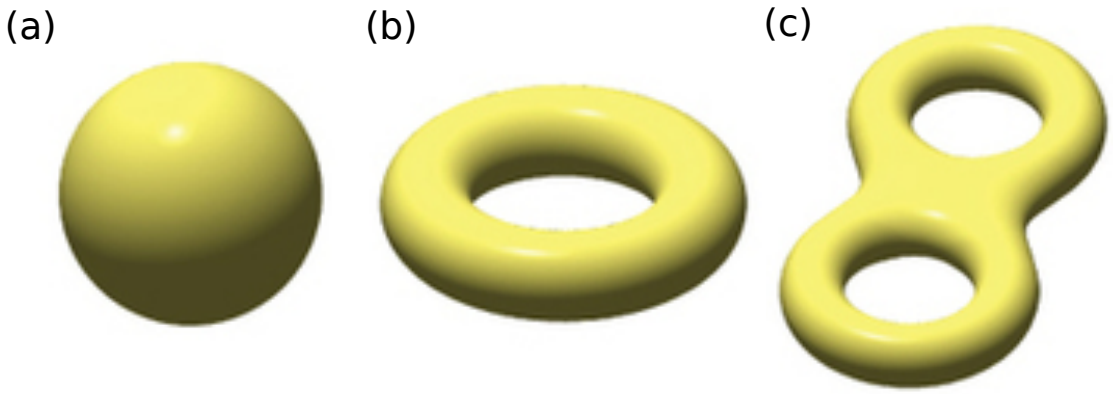

FIGURE 1.3: Three dimensional surfaces with different topological invariants. (a) sphere, topological invariant is 0; (b) torus, topological invariant is 1; (c) double torus, topological invariant is 2.

the topological invariant called the "genus" is defined as the number of holes in the surface. Fig. 1.3(a) is a spherical surface which has no holes at all and its topological invariant is 0. Fig. 1.3(b) is a torus surface with one hole inside and its topological invariant is 1. Fig. 1.3(c) is a double torus surface with two holes and its topological invariant is 2. Under continuous deformations such as tearing or stretching, but not piercing, cutting, and gluing, it is impossible to go from a sphere to a torus, or from a torus to a double torus. The topological invariant (the number of holes in the surface) is always the same under all kinds of continuous deformation. If you want to change its topological invariant, a topological phase transition such as piercing a hole or gluing a hole is needed.

1.2 Topological insulator

Topological insulators are novel phases of material which support conducting states at their surface while remain insulating at their bulk.

Before the discovery of topological insulators, materials were classified into metal and insulator by the mobility of outer electrons. The underlying reason is that the bandstructure of metals is gapless at the Fermi level while there is a bandgap in the bandstructure of insulators. A bandstructure schematic for a conventional insulator is presented in Fig. 1.4(a). A gap exists between upper conduction band and lower valence band, the Fermi level falling inside the gap.

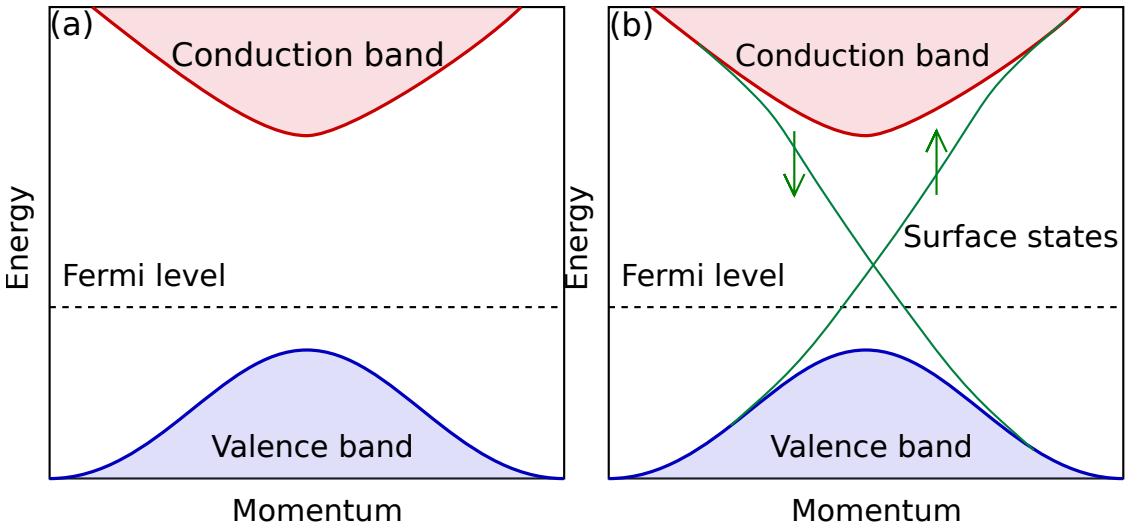

FIGURE 1.4: (a) Bandstructure of conventional insulator, bandgap exist, Fermi level falling between conduction band and valence band. (b) Bandstructure of topological insulator, surface states exist inside the bandgap.

Fig. 1.4(b) is the bandstructure for a topological insulator which is very similar to the bandstructure of a conventional insulator except the existence of surface states in the bandgap. These surface states contribute to unidirectional transmission lines at the edge of the material. Moreover, these transmission lines are protected by the topological features of the bandstructure, and are robust to defects such as imperfection and impurities in the material.

1.2.1 Origin and history of topological insulators

In condensed-matter physics, scientist often try to understand a phase of matter by investigating its response to some influence. In 1980s, a major discovery was that in a strong magnetic field, electrons that are confined to two dimensions present a completely novel phase — a topological phase which underlies the quantum Hall effect [3, 4]. A unique feature of this new phase is the existence of a metallic boundary simultaneously with an insulating bulk. The metallic boundary originates from topological invariants which cannot change without a topological phase transition and this unusual metal at the surface serves as the main experimental signature for topological insulator behavior.

The first reported 2D topological insulator is the quantum Hall gas [5] shown in Fig. 1.5(a). A droplet is surrounded by an ordinary insulator and a strong magnetic

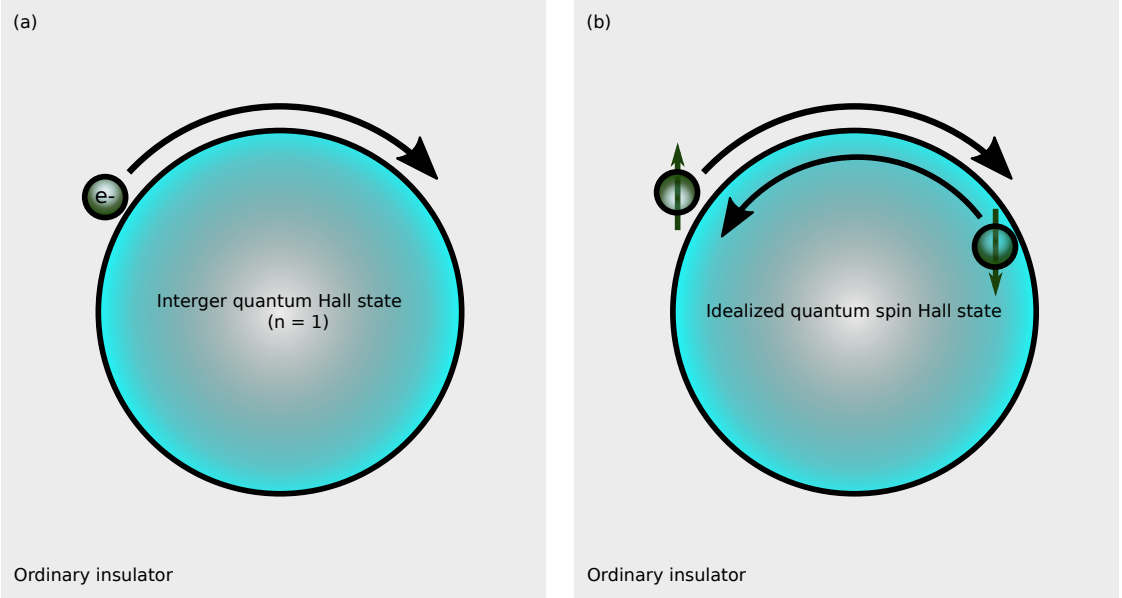

FIGURE 1.5: Topological order in two dimensions. (a). Edge of an integer quantum Hall state. The electrons (e^-) are confined to a 2D insulating droplet with a metallic edge. Along the edge, electrons propagate only in one direction, which is determined by the sign of the applied magnetic field perpendicular to the droplet. One integer, n, the topological invariant, determines the Hall conductance and the number of propagating edge modes. (b). Edge of an idealized quantum spin Hall state (that is, a 2D topological insulator). Along the edge, spin-up electrons move clockwise, whereas spin-down electrons move anticlockwise. Spin-up and spin-down electrons are independent and are in oppositely directed quantum Hall states. An applied electrical field generates a spin current but no charge current. Each droplet is surrounded by an ordinary insulator. Figure taken from reference [2].

field perpendicular to the plane is applied to the system, the resultant consequence is perfect quantum Hall edges wrapping around the 2D sample. The figure presents the edge of this integer quantum Hall state. The electrons (e^-) are confined to a 2D insulating droplet with a metallic edge and they can only propagate in one direction, which is determined by the sign of the the applied magnetic field. Meanwhile, the Hall conductance and the number of propagating edge modes are determined by one integer, n, the topological invariant.

After the discovery of the topological phases of quantum Hall system under strong magnetic fields, scientists searched for possible realizations of topological order without magnetic flux through the system. In late 1980s, Semenoff investigated a "2D graphite" model using tight-binding method but not succeeded [7]. Following Semenoff's work, Haldane proposed a 2D condensed matter lattice model with a

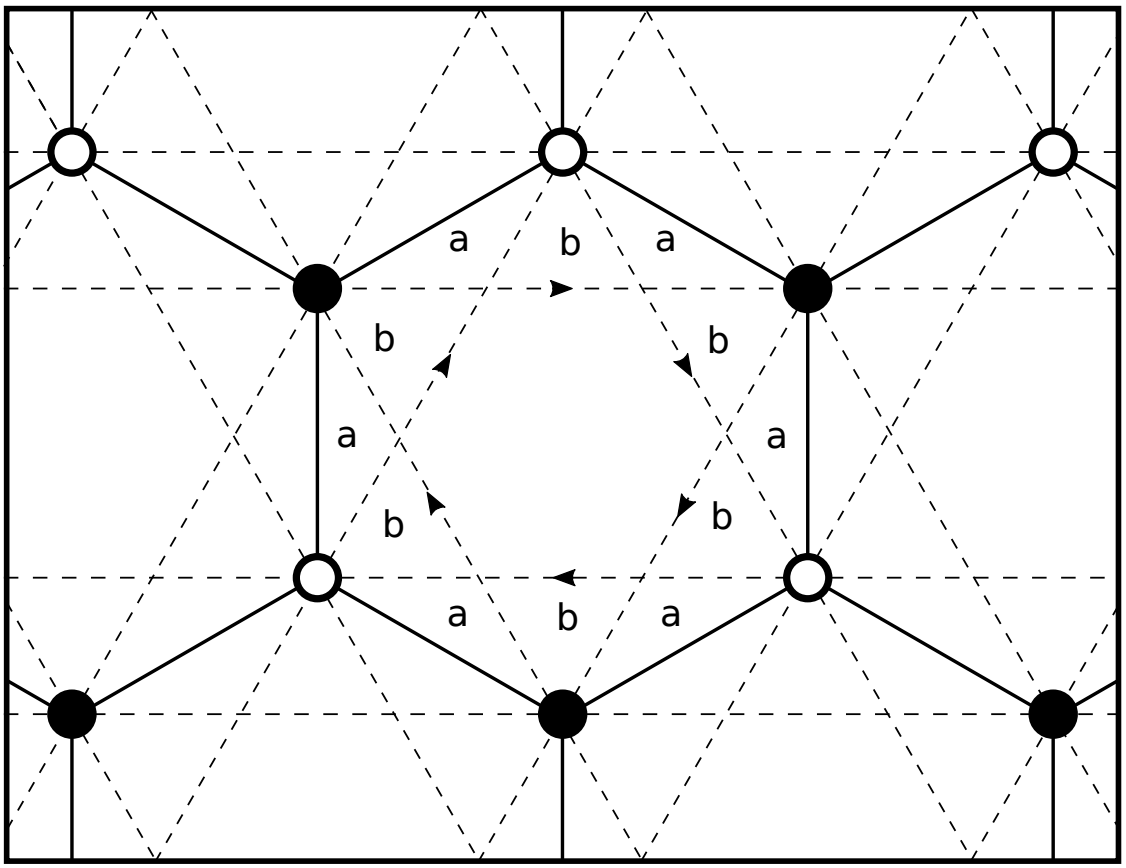

FIGURE 1.6: The honeycomb-net model consists of two interpenetrating triangular sublattices. Arrows on second-neighbor bonds indicate the directions of positive phase hopping used to break time-reversal symmetry. Figure taken from reference [6].

nonzero quantization of the Hall conductance with zero net magnetic flux through each unit cell in the network [6].

Usually, in the quantum Hall effect, under the influence of external magnetic field, the spectrum splits into Landau levels and forms a gap at the Fermi level. The 2D semimetal scenario considered by Haldane is different. In this model, a degeneracy forms at isolated points in the Brillouin zone between the top of the valence band and the bottom of the conduction band, that is associated with the presence of both inversion symmetry and time-reversal invariance. If a gap opens because one of the symmetries is broken, the system will becomes a normal insulator ($v = 0$) for inversion symmetry breaking and becomes a integer QHE state ($v = \pm 1$) for time-reversal symmetry breaking. If both symmetries are broken, the system remains in the normal insulator phase if the relative strength of time-reversal symmetry break is stronger, and the system will turn into topological phase if inversion-symmetry

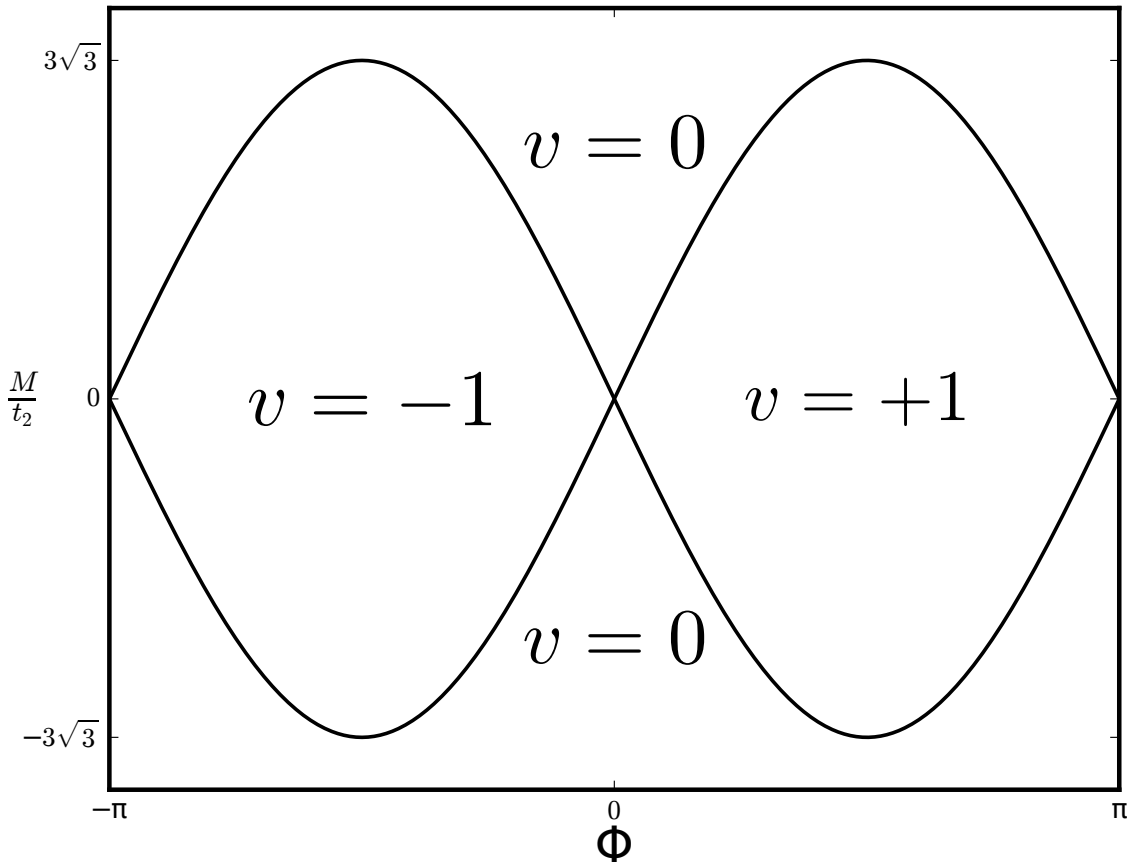

FIGURE 1.7: Phase diagram of the spinless electron model with $|t_2/t_1| < \frac{1}{3}$. If $|M/t_2| < 3\sqrt{3}|\sin\phi|$, zero-field quantum Hall effect phases ($v = \pm 1$) will occur. Figure taken from reference [6].

broken is stronger [8]. These situations are presented in Fig. 1.8.

The lattice used by Haldane is a "2D graphite" model as shown in Fig. 1.6. It is a honeycomb net structure, containing two interpenetrating triangular lattices ("black" and "white" sublattices). These two sublattices will interchange with each other after a π rotation. A t_1 real hopping matrix element exists between nearest points and a t_2 real hopping term exists between nearest-neighbor sites on the same sublattices. To break time-reversal symmetry, a periodic local magnetic field is added to the system in the direction normal to the 2D plane which ensures zero total flux through each unit cell with proper symmetry. As a result, the closed paths of first-neighbor hops (t_1) enclose complete unit cells will no net flux, while closed paths of second-neighbor hops (t_2) acquire a phase $\phi = 2\pi(2\Phi_a + \Phi_b)/\Phi_0$, where Φ_a and Φ_b are the fluxes through the regions of the unit cell marked a and b in Fig. 1.6, $\Phi_0 = |h/e|$ is the flux quantum. The effect of inversion- symmetry-breaking on-site energy $+M$ on black sites and $-M$ on white sites is also considered.

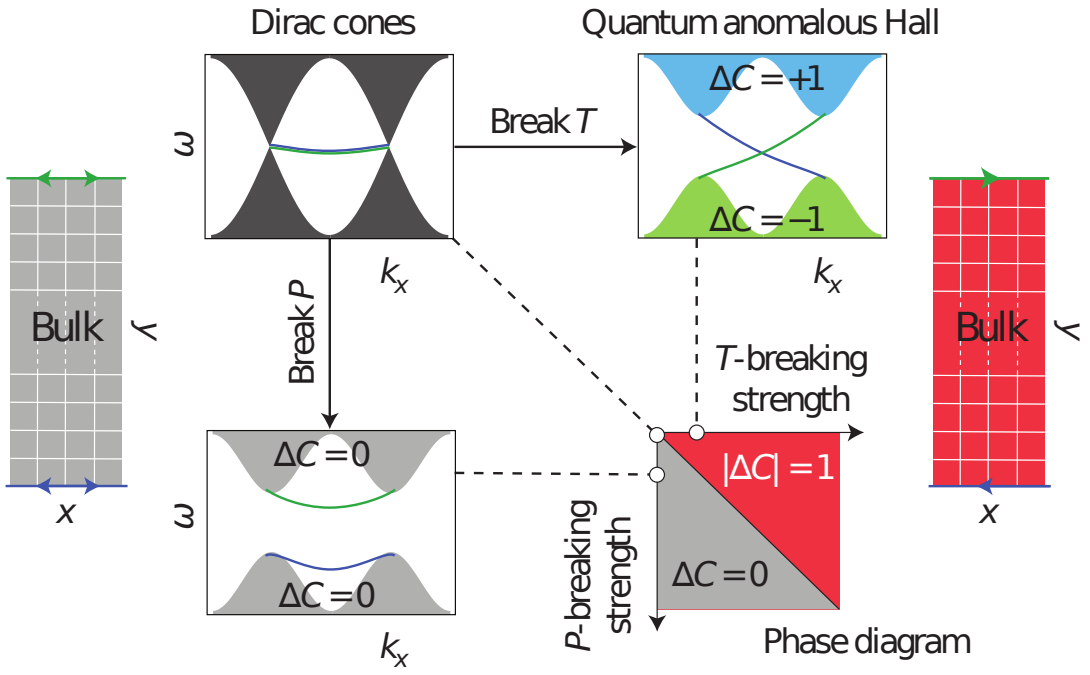

FIGURE 1.8: Symmetry breaking of the 2D quantum Hall system. The top-left image shows a band diagram of edge states in which the bulk dispersions form a pair of Dirac cones (gray) protected by PT symmetry. The green and blue lines represent edge dispersions on the top and bottom edges. When either P or T are broken, a bandgap can form in the bulk but not necessarily on the edges. When T-breaking is dominant, the two bulk bands split and acquire Chern numbers of ± 1. Thus, there exists one gapless edge dispersion on each of the top and bottom interfaces, assuming the bulk is interfaced with topologically trivial insulator. This T-breaking phase of non-zero Chern numbers is the quantum Hall phase, plotted in red in the phase diagram. Figure taken from reference [8].

After rigorous calculation, Haldane found that if $|t_2/t_1| < \frac{1}{3}$, zero-field quantum Hall effect phases ($v = \pm 1$) occur under the condition that $|M/t_2| < 2\sqrt{3}|\sin\phi|$, the result is shown in Fig. 1.7. This results means under proper condition, with zero net magnetic flux through the system, it is possible to realize a non-trivial photonic topological system which is one of the most important discovery in the development of photonic topological insulator.

Subsequent developments on topological insulators are based on spin-orbit coupling, which cannot induce the quantum Hall effect since it does not break time-reversal symmetry as a magnetic field would. However, in around 2003, a simplified model proved that spin-orbit coupling can lead to a quantum spin Hall effect [9–11], in which spin-up and spin-down electrons move in opposite directions along the sample edge without the influence of an external magnetic field, as shown in

Fig. 1.5(b). This figure show the edge of an idealized quantum Hall state in a 2D topological insulator. Along the edge, spin-up electrons move clockwise, whereas spin-down electrons move anticlockwise. Spin-up and spin-down electrons are independent and are in oppositely directed quantum Hall states. An applied electrical field generates a spin current but no charge current.

In 2005, Kane and Mele [12] made a key theoretical breakthrough by finding a new type of topological invariant. It enabled scientists to predict whether a realistic 2D material has a stable edge state and compute its topological invariant in the absence of external magnetic field. Subsequently, Bernevig, Hughes and Zhang predicted that 2D topological insulator behavior can be observed in (Hg,Cd)Te quantum wells [13, 14].

In 2006, scientists made another theoretical breakthrough by realizing that the topological insulator idea can be realized in genuinely 3D states [15–18]. Stacks of a 2D topological insulator can form a 3D 'weak' one which is not robust to disorder. To form a 'strong' 3D topological insulator, spin-orbit coupling is required and must mix all components of the spin. 3D topology insulators have metallic surface states which are protected by topological properties, serving as the major experimental observable.

In 2008, using angle-resolved photoemission spectroscopy (ARPES), Hsieh discovered the first 3D topological insulator, the alloy Bi_xSb_{1-x} [19, 20]. In searching for topological insulator materials, heavy-element, small-bandgap semiconductors such as Bi_2Se_3 and Bi_2Te_3 stand out for having higher temperatures topological state, larger bulk bandgaps (more than 0.1 eV), and simplest surface state [21–23]. In a 3D topological insulator, the surface state is closely related to the Dirac electronic structure of graphene [24]. Graphene has two spin-degenerate Dirac points, while the surface of a topological insulator has only one Dirac point without spin degeneracy; this difference provides various possible applications for topological insulators [25–33].

Recently, the successful synthesization of nanoribbons of Bi_2Se_3 [34] and growing thin films of Bi_2Se_3 with controlled thickness down to a single cell [35] has made it more promising for proposed applications of topological insulator in spintronics and other fields [36].

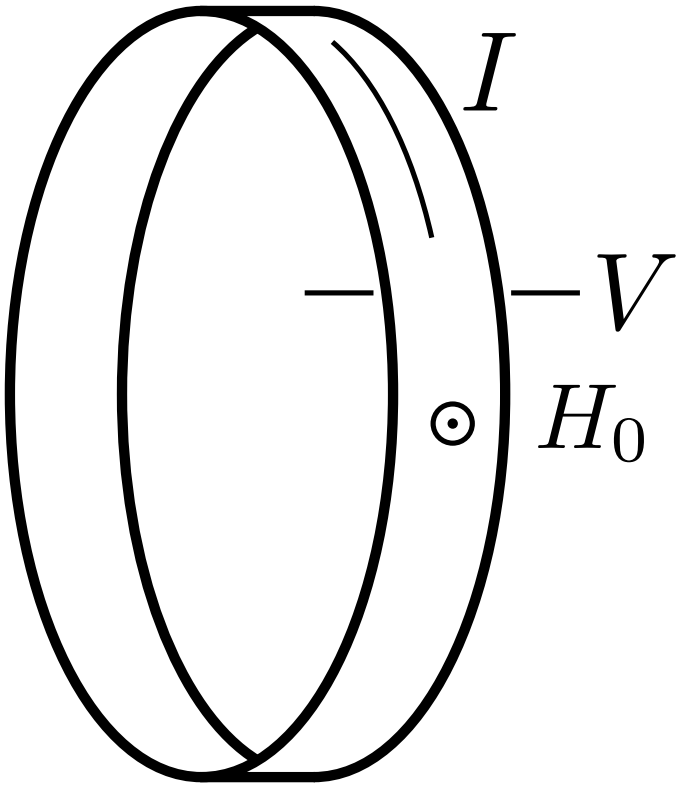

FIGURE 1.9: Topological pump schematic. A 2D ribbon is wrapped into a loop and magnetic field H_0 perpendicular pierced through the ribbon surface. Around the ribbon, net current I flow around the loop and voltage difference V exist between two edges of the ribbon, figure taken from reference [37].

1.2.2 Topological pump ideas/Laughlin's model

In early 1980s, von Klitzing et al. and Tsui et al. discovered that the Hall conductivity of an inversion layer can quantized to better than one part in 10^5 to integral multiples of e^2/h [37, 38]. In order to investigate the accuracy of this quantization, based on adiabatic theorem, Laughlin proposed the famous "adiabatic pumping" experiment which indicate a possible way to measure this quantization. Fig. 1.9 is the adiabatic pumping setup. A 2D ribbon is wrapped into a loop with circumference L, and magnetic field H_0 perpendicularly pierced through the ribbon surface. Around the loop surface, net current I flows around the ribbon and the voltage drop from one edge to the other edge is V. After rigorous computation, the relation between current I and voltage drop V can be written as

$$I = c\frac{neV}{\Delta\phi} = \frac{ne^2V}{h}, \tag{1.1}$$

where ϕ is the magnetic flux through the loop. This equation means by increasing the magnetic flux ϕ through the ribbon, the particles at one edge can be pumped into the other edge. However, even though this experiment is nicely designed, due to the difficulty in realizing the experimental setup, including the ribbon geometry and the unusual configuration of the applied magnetic fields, it has always been considered a "thought experiment" and has never been experimentally realized.

1.3 Photonic topological insulator

After the exciting development of topological insulators in solid-state physics [39, 40], Haldane and Raghu introduced the concept into photonics in 2005 [41, 42] by theoretically proposing the photonic analogue of the quantum Hall effect in photonic crystals [43]. In ordinary waveguides, back-reflection and loss borders large-scale optical integration. Topological photonics allows for unique unidirectional edge waveguides, which do not experience back-reflection even in the presence of imperfections and impurities. This special characteristic has promising applications in many areas of photonics.

1.3.1 Topological invariants in photonic topological insulator

When we investigate a certain topological space, we usually use some kind of topological invariant to characterize this set. A closed surface can be smoothly deformed into various geometries without cutting and pasting. The GaussBonnet theorem [44] of Eq. 1.2 below, which connects geometry to topology, states that the total Gaussian curvatures (K) of a 2D closed surface is always an integer. This topological invariant, named genus (g), characterizes the topology of the surface; that is, the number of holes within. Examples of surfaces with different geni are shown in Fig. 1.3.

$$\frac{1}{2\pi}\int_{surface} K\mathrm{d}A = 2(1-g), \tag{1.2}$$

A two dimensional Brillouin zone is also a closed surface with the same topology of a torus due to its periodic boundary conditions (Fig. 1.10). Integrating the Berry curvature ($\Delta_k \times A(k)$) over the torus surface yields the topological invariant

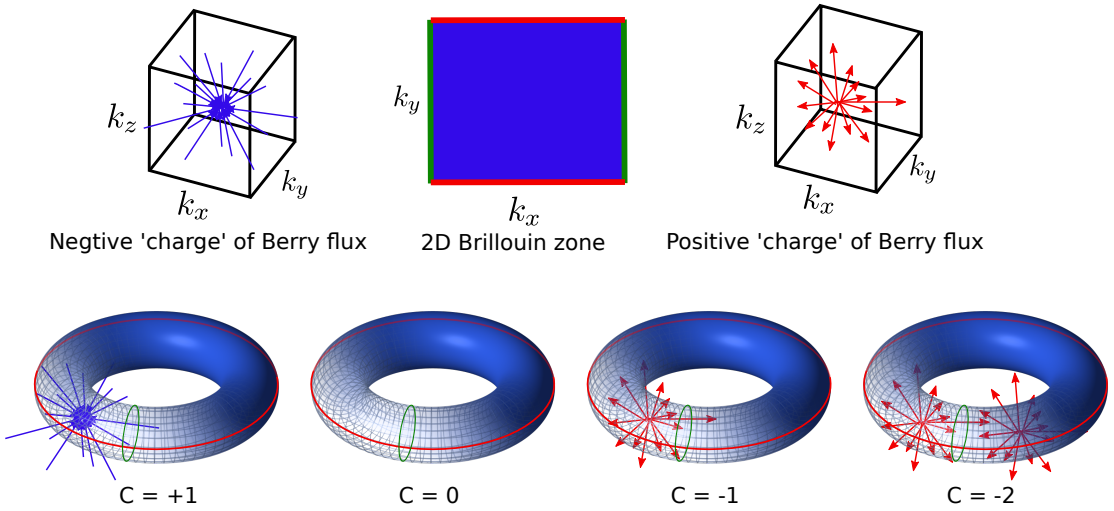

FIGURE 1.10: Chern number is the integration of Berry curvature over a closed surface and can be viewed as number of monopoles of Berry flux insided. A 2D Brillouin zone has the same topology as a 2D closed torus surface because of its periodic boundary conditions.

known as the Chern number, as shown in Eq. 1.3, which gives a measure of the total quantized Berry flux of the 2D surface. The Chern number can be viewed as the number of monopoles of Berry flux inside a closed surface, as illustrated in Fig. 1.10.

$$C = \frac{1}{2\pi} \oiint \Delta_k \times A(k) \dot{ds} \tag{1.3}$$

In our network model, as described in Section. 1.3.2, it is impossible to directly measure the Chern number of the system bands. Therefore, another topological invariant (a winding number [45], which describes the total number of times of a 2D curve travels counterclockwise around a given point in a plane) is used to characterize the system [46]. If the system is in a topological trivial phase, this winding number will be zero. If the system is in a topological nontrivial phase, this winding number will be a nonzero integer. Fig. 1.11 presents several curves with different winding numbers.

1.3.2 Network model for Floquet photonic topological insulator

In 2011, Hafezi designed a robust optical delay line model as shown in Fig. 1.12, and experimentally realized this model by observing uni-directional optical transmission

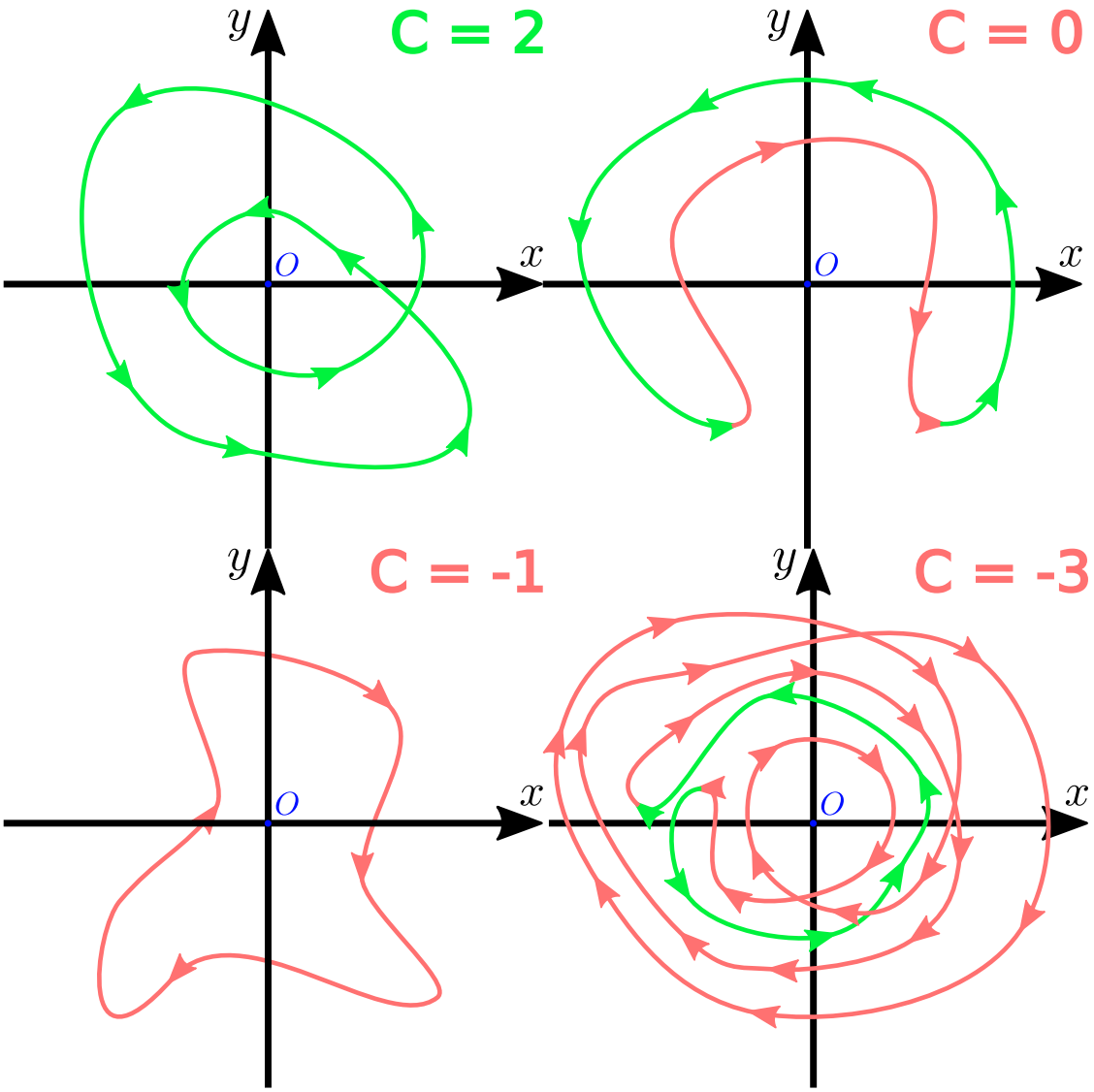

FIGURE 1.11: Winding number is defined as total times of a 2D curve travels counterclockwise around a given point (here is the Origin O). Curve segments moving clockwise are colored in red while segments moving counterclockwise are colored in green.

line along the edge on a silicon-based microfabricated resonator lattice [47, 48]. In Hafezi's model, a resonator array (gray disks) which supports counter-clockwise optical transmission is connected together by waveguides (white eclipses) which supports clockwise transmission. All the resonators are exactly the same and the resonator frequency is designed to be different from that of the waveguides. For the waveguides connecting resonators in the vertical direction, the connecting point is at the center which ensures the phase hopping in the left edge is equal to that in the right edge. As for the waveguides connecting resonators in the horizontal direction, the connecting points are shifted a little compared to the lower one on

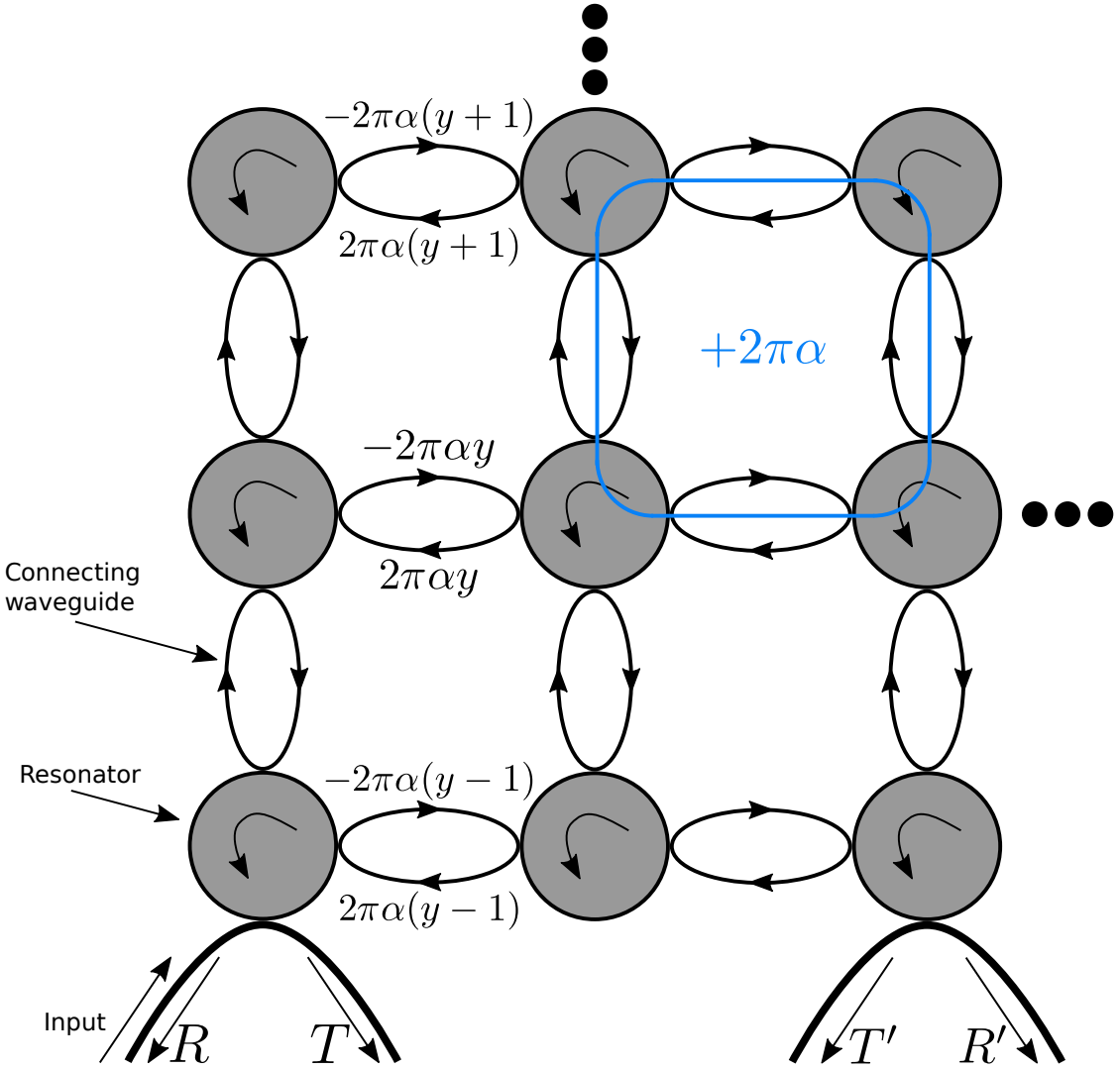

FIGURE 1.12: Hafezi's network model. Resonators (gray disks) which supports counter-clockwise transmission are connected together by waveguides (empty eclipses) which supports clockwise transmission. The connecting point of waveguides in the horizontal direction are shift a little compare to the lower one. This shift acquire addition $2\pi\alpha$ phase after travelling a loop through the blue square which is equivalent to an external magnetic flux.

the same column. When traveling a whole loop as indicated by the blue line, two vertical edges and two horizontal edges will be touched. The left vertical edge and right vertical edge are of equal length and zero phase hopping will be introduced. However, the upper horizontal edge is different with the lower horizontal edge, as a result, travelling through a loop as indicated by the blue square will acquire an additional $2\pi\alpha$ phase which is equivalent to a magnetic flux α through the cell. In this way, Hafezi effectively breaks the time-reversal symmetry for a given direction of circulation, without an external magnetic field.

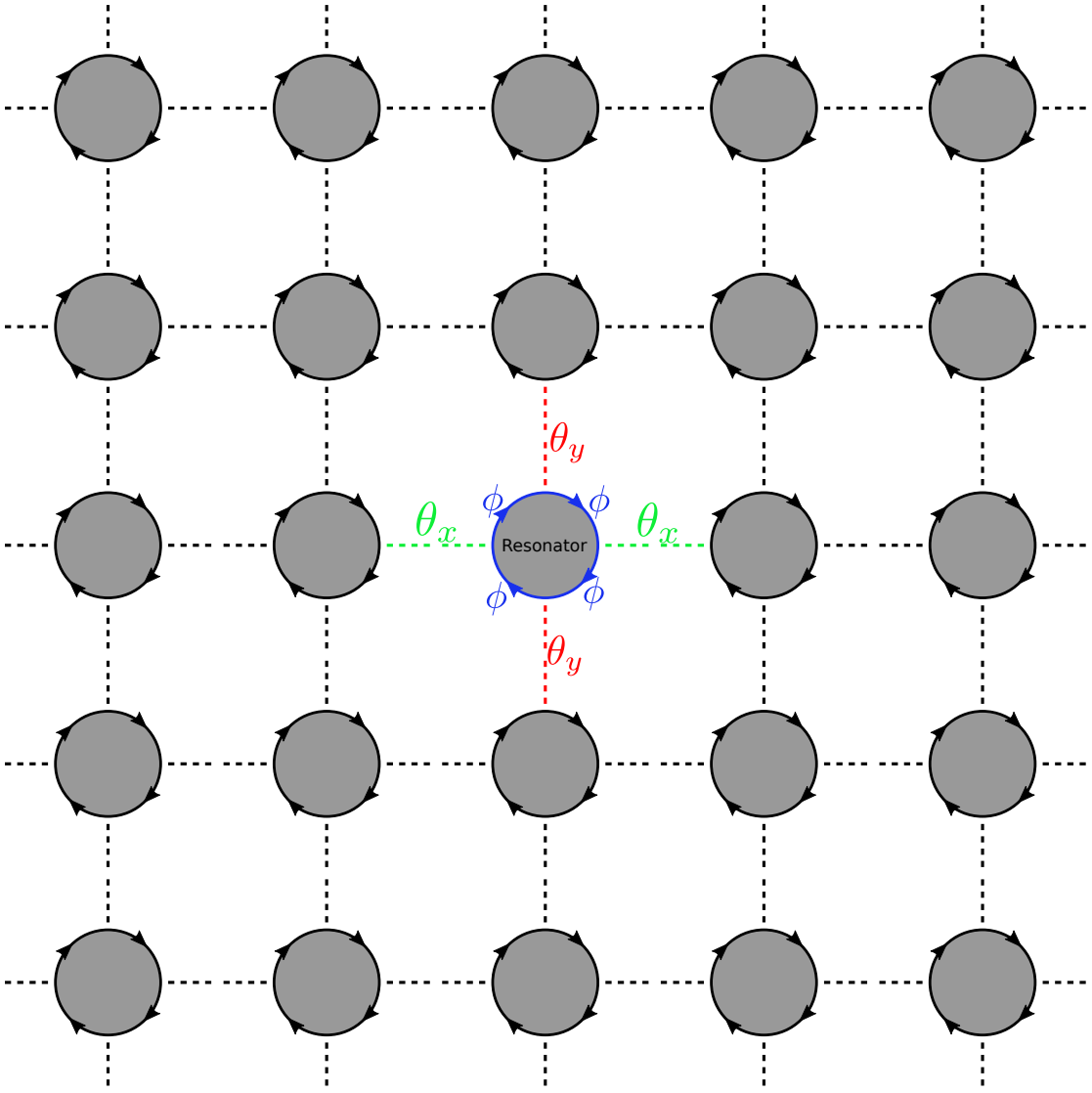

FIGURE 1.13: Our network model. All the resonators are exactly the same and only support clockwise transmission. Neighboring resonators are coupled together and the coupling strength is described by θ_x and θ_y. Each resonator are divided into four equal quarter rings with ϕ phase delay.

Following Hafezi's work, it was found that the system can still exhibit a topological phase without the synthetic magnetic field under proper condition [49–52]. Our network design is shown in Fig. 1.13; all the resonators are exactly the same and they are coupled with neighboring resonators. The coupling strength is described using θ_x in the x direction and θ_y in the y direction, each resonator is divided into four equal quarter rings by the coupling points and the phase delay of each quarter ring is ϕ. Here, we assume $\theta = \theta_x = \theta_y$ and restrict our attention to clockwise transmission. Actually, this resonator-and-waveguide photonic topological insulator can be modeled as networks of the sort developed by Chalker and Coddington

in the 1980s to study the Anderson transition in quantum Hall systems [53]. The Bloch modes of periodic network models can be mapped onto the Bloch-Floquet states of driven lattices. After calculation, we found that the system is in a normal insulator phase if $\theta_x + \theta_y < \pi/2$ (or $\theta < \pi/4$) and the system will exhibit a topological nontrivial phase if $\theta_x + \theta_y > \pi/2$ (or $\theta > \pi/4$) [51], this result will be rederived later in Section 2.4.

1.3.3 Experiment realization of photonic topological insulator

In 2008, Wang et al. realized the idea proposed by Haldane and Raghu [6, 41, 42] at microwave frequencies [54–56]. They designed a gyromagnetic photonic crystal as shown in Fig. 1.14(a). This 2D square lattice photonic crystal is an array of gyromagnetic ferrite rods which is confined within two parallel horizontal copper plates separated by 7.0 mm. This kind of structure can support TEM modes, with magnetic fields parallel to the copper plates and electric fields normal to the plates, up to 21 GHz. One edge of the structure is precisely designed for measuring edge states while the other three edges are filled with microwave-absorbing foam pieces which absorb unwanted edge states and protect the system from external interference.

According to their theoretical calculations [54], if this system is place under strong magnetic field perpendicular to the plate, time-symmetry will be broken and a single topologically protected edge mode will appear between the second and third band which both have non-zero Chern numbers, as shown in Fig. 1.14(b). This red dispersion line inside the second bandgap has only positive group velocities at around 4.5 GHz. Fig. 1.14(c) shows the numerical simulation results. The figure also shows unidirectional transmission line and the robustness of this transmission line against obstacles such as a long metallic scatterer. Fig. 1.14(d) gives the experimental results, which show that forward-transmission is five orders of magnitude stronger than back-reflection, in accordance with theoretical predictions. In this way, they successfully demonstrate a photonic crystal that contains non-zero Chern numbers. Similar single-mode one-way waveguides can also be realized using different structures [57–61] and it also promises plenty of applications [62–66].

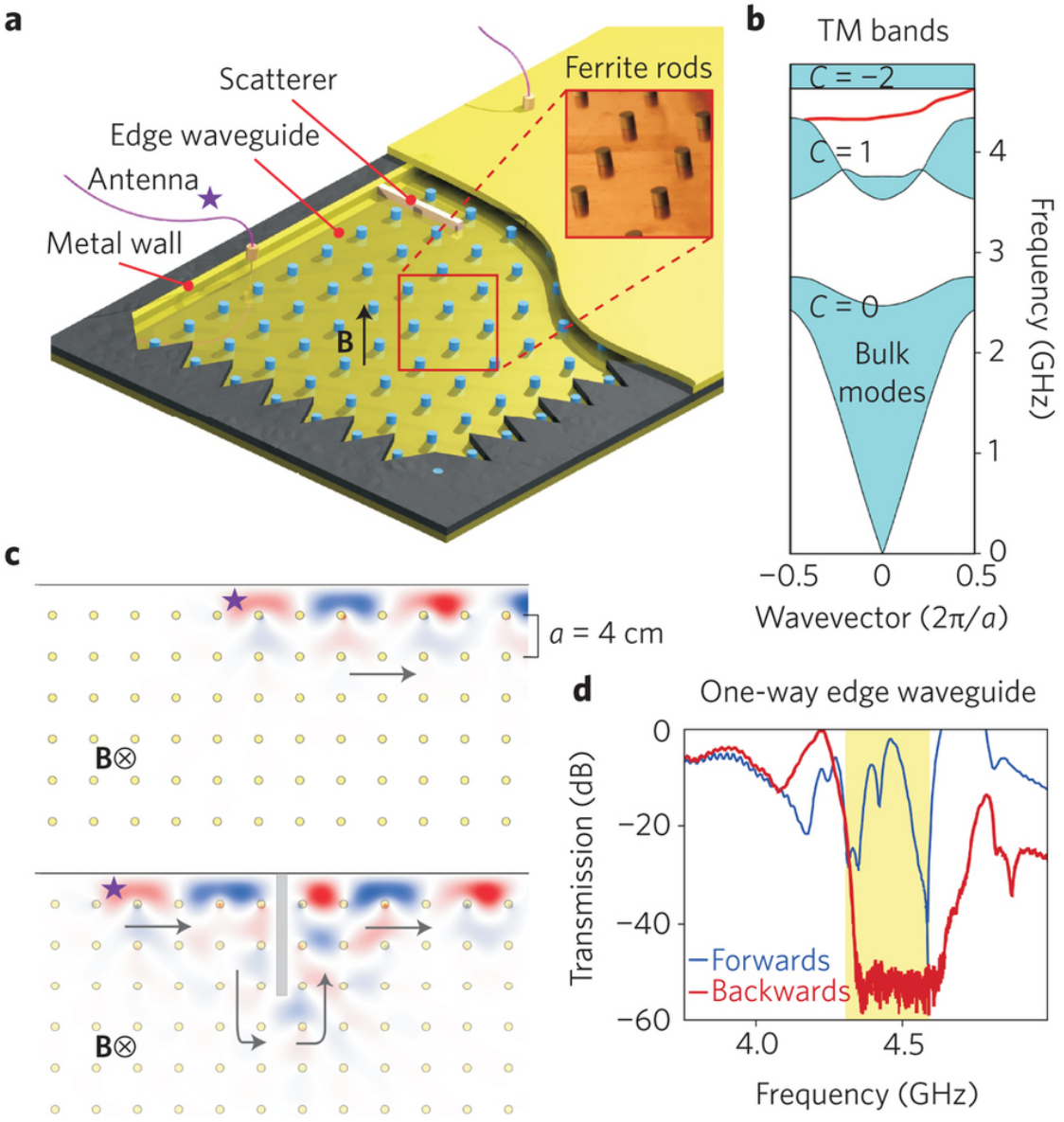

FIGURE 1.14: First experimental demonstration of the topologically protected one-way edge waveguides in microwave frequencies. (a) Experimental setup, a photonic crystal consisting of gyromagnetic rods, the lattice period is 4 cm. This structure can support 2D TM modes at 4.5 GHz which is parallel to the copper plate. (b) Red line is the one-way edge modes between two band with nonzero Chern number. (c) Numerical simulation results show the uni-directional transmission line and its robustness to long metallic scatter obstacle. (d) Experimental results, the forward transmission is five order of magnitude stronger than back-reflection. Figure taken from reference [8].

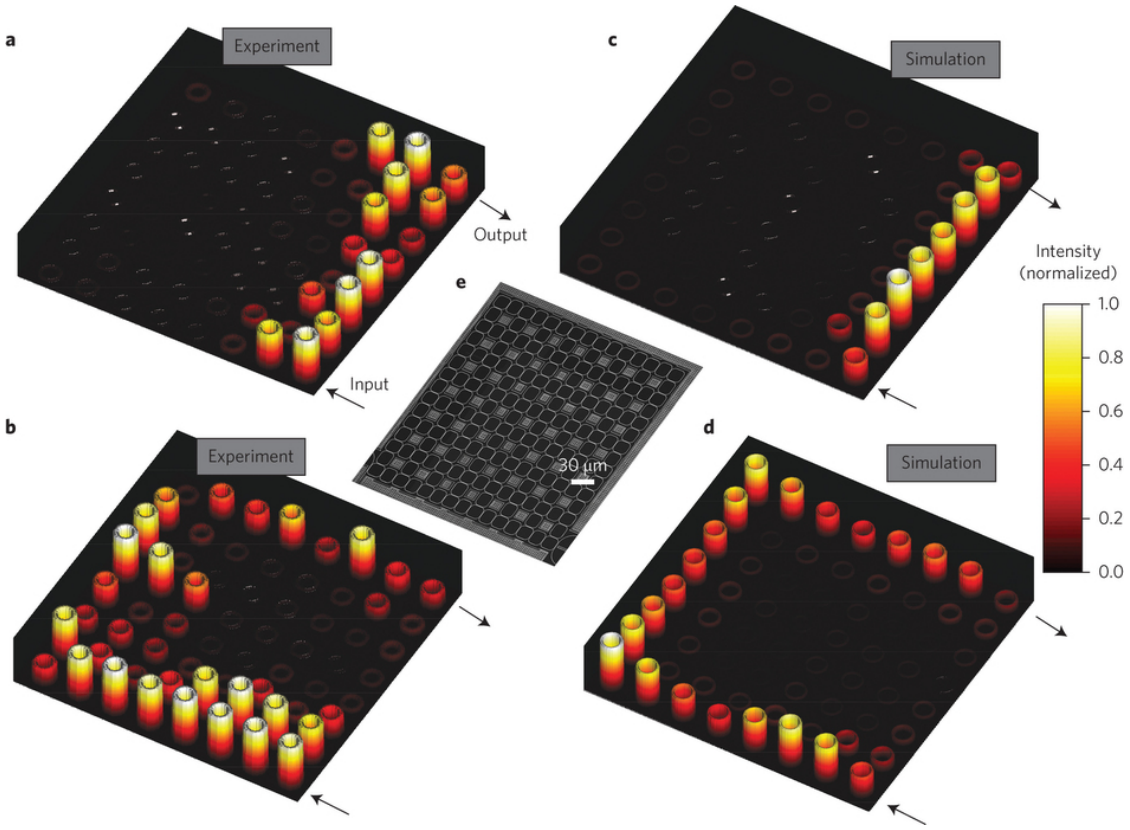

FIGURE 1.15: **a-d**, edge state propagation results. Depending on input frequency, the light takes the short edge (**a**) or the long edge (**b**). The experiment results (**a,b**) match the simulation results (**c,d**) well. **e**, SEM image of the system. Figure taken from reference [48].

In 2013, based on his model described in Section. 1.3.2, Hafezi et al. implemented this idea by fabricating a 2D array of coupled optical ring resonator using silicon-on-insulator (SIO) technology [67–73]. On this experiment, details are specifically designed to ensure single-mode propagation of the transverse electric (TE) light at telecom wavelength ($\approx 1.55\mu m$), different resonant frequencies for waveguides and resonators, negligible bending loss, and reduced surface roughness. All these details contribute to the successful realization of his idea. Fig. 1.15 presents the simulation and experimental results of this experiment. Depending on the input frequency, the light takes the short edge (a) or the long edge (b). The experimental results (a, b) match the simulation results (c, d) well. The uni-directional edge modes demonstrate the topological properties of the system.

In 2013, Rechtsman et al. experimentally realized the Floquet topological phase [75, 76] for the first time. Starting from a 2D resonator array (show in Fig. 1.16

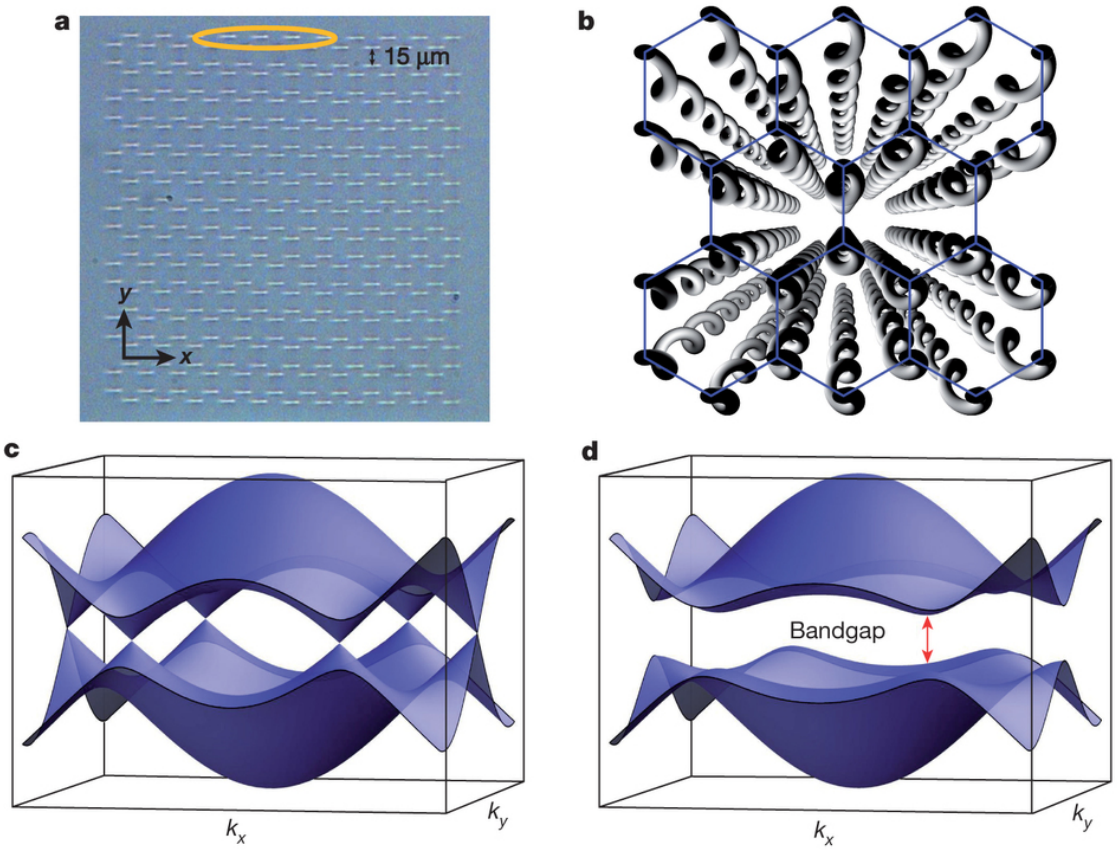

FIGURE 1.16: Geometry and band structure of honeycomb Folquet topological insulator lattice. **a**, microscope image of the input facet of the photonic lattice. **b**, helical waveguide structure. **c**, band structure for non-helical waveguide honeycomb lattice, no bandgap and edge states. **d**, band structure for helical honeycomb lattice, z-symmetry breaking opens up band structure and forms a bandgap with symmetry-protected edge states. Figure taken from reference [74].

(a)), the array is extended in the z direction by rotating periodically to form a helical structure as show in Fig. 1.16 (b). If the waveguides are non-helical 2D network, the band structure is show in Fig. 1.16 (c); the bandgap is closed and there are no edge states in the system, which means the system is in a topologically trivial state. By introducing a helical structure in the z direction, the periodic helical modulations [77, 78] play the role of time and break z-symmetry, which is equivalent to time-domain modulations that break T-symmetry. This symmetry-breaking opens up the bandgap and forms a topologically non-trivial bandgap with symmetry-protected gapless edge modes (Fig. 1.16 (d)). This topologically nontrivial state is called a Floquet topological insulator. To experimentally demonstrate this idea, Rechtsman fabricated the helical structure using fentosecond laser writing, and successfully observed the symmetry-protected edges states.

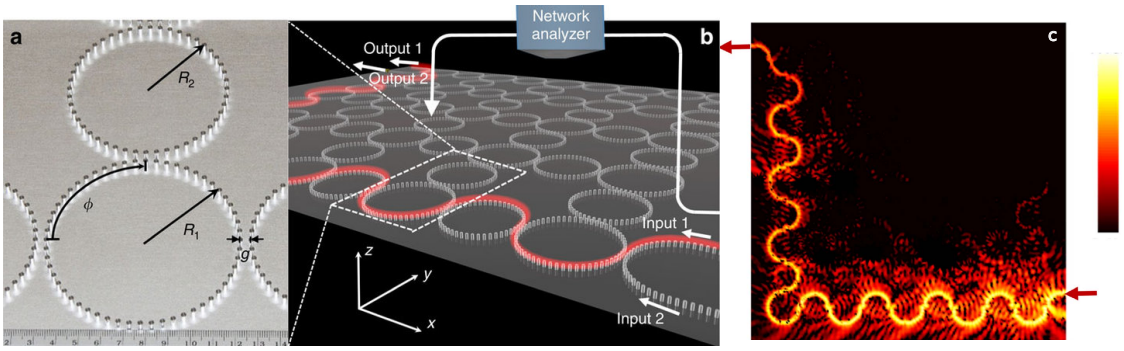

FIGURE 1.17: (a) Photos of experiment implementation. Each resonator ring consists of 56 metallic rods and each coupling rings contains 48 metallic rods. Rods are arranged carefully to forms the network model. (b) Schematic of experiment lattice. The topological phase state is demonstrated by observing robust edge states in the system. (c) Experiment result for observed edge state at frequency 11.3GHz. Figure taken from reference [79].

In 2016, Gao et al. experimentally realized the "anomalous" Floquet topological edge states using a unique designer surface plasmon structure [79]. The network model of Gao's experiment is the same as our model which is described in detail in Section. 1.3.2. The major difference between Gao's experiment and other coupled-ring resonator implementations is that a row of coupled metallic rods are used to take the place of traditional waveguides. The structure of Gao's experiment is shown in Fig. 1.17(a), each resonator ring consists of 56 metallic rods and each coupling ring is composed of 48 metallic rods with rods. All the parameters such as rod height, rod distance, rod diameter, and inter-ring distance are carefully designed to ensure that desired modes can survive in the system and successfully hopping between neighboring rods. Fig. 1.17(b) shows the experimental results including the uni-directional edge transmission which demonstrates the system is in a topological non-trivial phase.

Except for all the works mentioned in this section, scientist have also tried many other ideas to realize topological phases by creating effective magnetic fields for neutral particles [80], using synthetic gauge fields in optical lattices [81], in optomechanics [82], and radiofrequency circuits [83]. Meanwhile, the topological idea has also been extended to 3D systems and lots of effort has been applied to implement it [84–90].

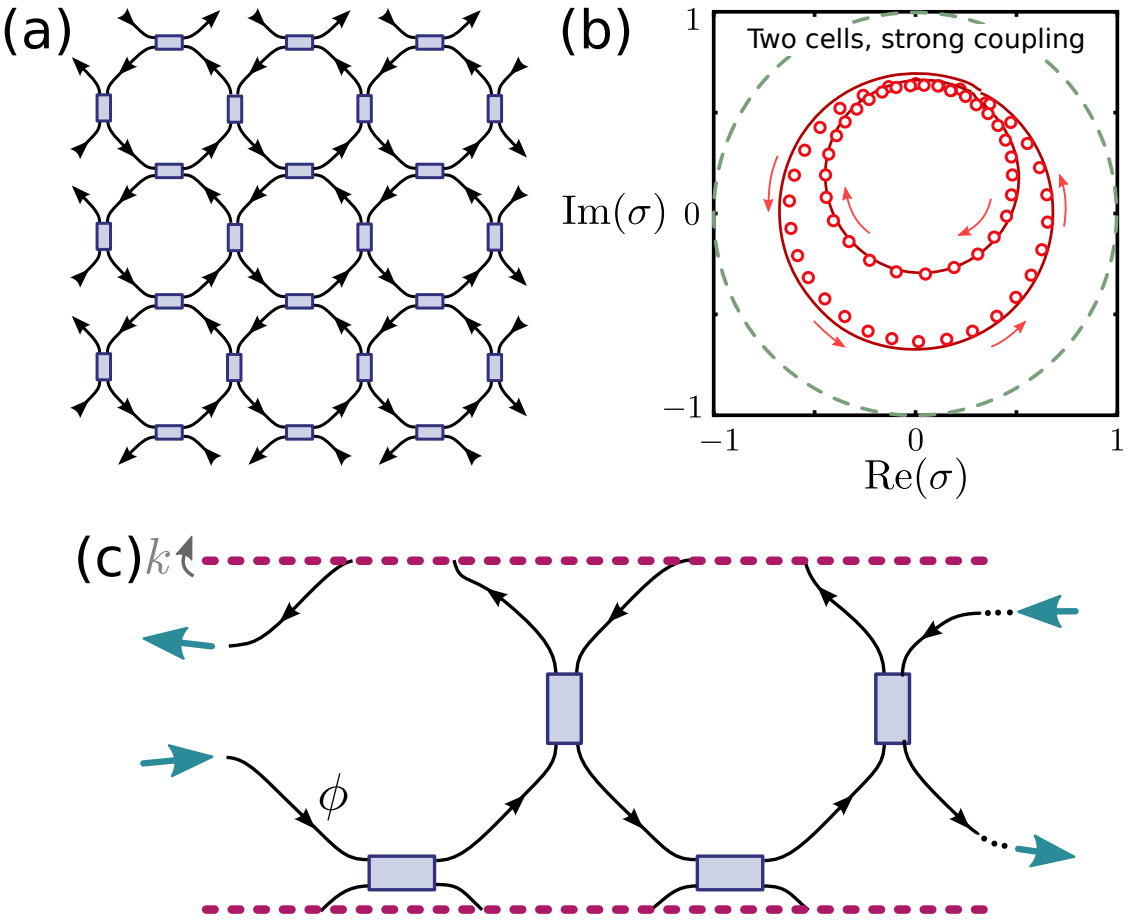

FIGURE 1.18: (a) 2D coupled ring resonator network structure. (b) Experiment result for a two cells, strong coupling (topological nontrivial) system, the winding number of two eigenvalues are ±1. (c) Two port network model mapped from the 2D structure shown in (a).

1.3.4 Measurement of topological invariants in photonic topological insulator

In condensed-matter systems, the most important physical consequence of topologically nontrivial band structures is that they cause certain macroscopic transport properties to be precisely quantized. Most famously, in the integer QH effect, the Hall conductance is quantized to integer multiples of the inverse von Klitzing constant to nearly one part in 10^9 [37]. An influential explanation for this was supplied by Thouless et al. [91], who showed using linear response theory that the QH conductance is tied to the Chern numbers of the bands, which are "topological invariants" restricted to integer values. In photonics, however, there is no direct analog of the Hall conductance or similar linear response-based quantity, due to the

absence of a fermionic ground state [41, 42]; this is why edge propagation measurements have served almost exclusively as the signature for topologically nontrivial photonic band structures.

From the previous description of topological invariants in Section. 1.3.1, we know that certain winding numbers measured in "topological pumping" experiments are topological invariants equivalent in function to the Chern number and can be used to describe the topological phase of a system. Hence, it is possible to map the 2D coupled ring resonator network (Fig. 1.18(a)) into a two-port network as shown in Fig. 1.18(c). Moreover, this two-port network can be experimentally realized in the microwave regime and the S matrix of the system can be measured using a network analyzer [52]. The result is shown in Fig. 1.18(b). The eigenvalues of the S matrix for a two-cell, strong coupling system encircle the origin with winding numbers ± 1 as k goes from 0 to 2π. If the system is in a topological trivial state, no winding behavior can be observed. Later, in 2016, Hafezi et al. directly measure a topological invariant in experiment [92] by realize the model proposed by in him in 2014 [93].

1.4 Exceptional points

In the mathematical field of complex analysis, a exceptional point (EP, also know as branch point) of a multi-valued function is a point such that the function is discontinuous when going around an arbitrarily small circuit around the point[94]. For example, Fig. 1.19 shows the Riemann surface [95] for the function $f(z) = \sqrt{z}$, here the exceptional point is the origin because the analytic continuation of any solution around a closed loop containing the origin will result in a different function.

In physics, EPs occur generically in eigenvalue problems that depend on a parameter [96–99]. If the parameter is real, the system Hamiltonian is Hermitian and has no EPs. However, if the parameter value is complex, the system become non-Hermitian, EPs will form and properties associated with degeneracy of Hermitian operators becomes invalid.

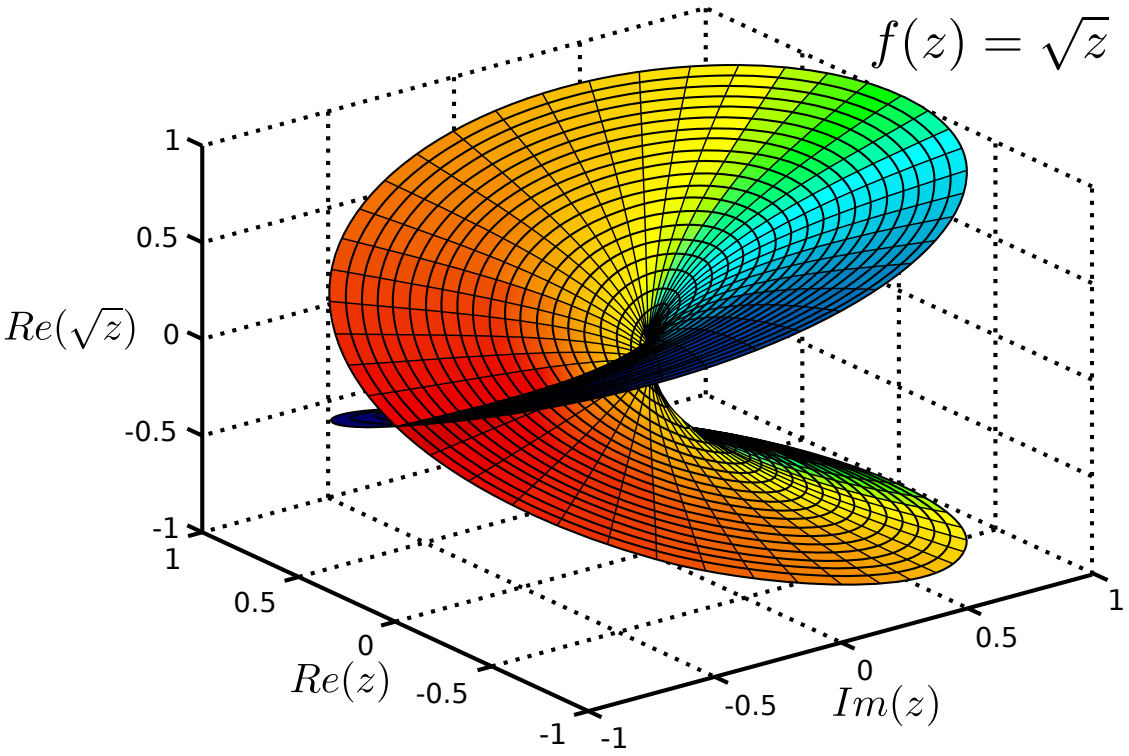

FIGURE 1.19: Riemann surface for the function $f(z) = \sqrt{z}$.

Consider the following eigenvalue problem

$$\begin{aligned} H(\lambda) &= H_0 + \lambda V \\ &= \begin{bmatrix} \omega_1 & 0 \\ 0 & \omega_2 \end{bmatrix} + \lambda \begin{bmatrix} \epsilon_1 & \delta_1 \\ \delta_2 & \epsilon_2 \end{bmatrix}, \end{aligned}$$

where ω_k and ϵ_k determine the non-interacting resonance energies $E_k = \omega_k + \lambda\epsilon_k, k = 1, 2$. All the parameters can be complex but $[H_0, V] \neq 0$ must be satisfied to ensure the problem is non-trivial. Owing to the interaction invoked by the matrix elements δ_k, the two levels do not cross but repel each other. The eigenvalue equation of this problem is:

$$\left[\begin{bmatrix} \omega_1 & 0 \\ 0 & \omega_2 \end{bmatrix} + \lambda \begin{bmatrix} \epsilon_1 & \delta_1 \\ \delta_2 & \epsilon_2 \end{bmatrix} \right] \psi = E\psi. \tag{1.4}$$

To solving this equation, we have:

$$\begin{bmatrix} \omega_1 + \lambda\epsilon_1 - E & \lambda\delta_1 \\ \lambda\delta_2 & \omega_2 + \lambda\epsilon_2 - E \end{bmatrix} = 0. \tag{1.5}$$

This equation is equivalent to:

$$E^2 - (\omega_1 + \lambda\epsilon_1 + \omega_2 + \lambda\epsilon_2)E + (\omega_1 + \lambda\epsilon_1)(\omega_2 + \lambda\epsilon_2) - \lambda^2\delta_1\delta_2 = 0. \tag{1.6}$$

At the exceptional points, the two levels coalesce at specific values of λ in the vicinity of the level repulsion, where $E_1 = E_2$, therefore, we have:

$$(\omega_1 + \lambda\epsilon_1 + \omega_2 + \lambda\epsilon_2)^2 - 4[(\omega_1 + \lambda\epsilon_1)(\omega_2 + \lambda\epsilon_2) - \lambda^2\delta_1\delta_2] = 0, \tag{1.7}$$

this can be simplified to:

$$[(\omega_1 + \lambda\epsilon_1) - (\omega_2 + \lambda\epsilon_2)]^2 + 4\lambda^2\delta_1\delta_2 = 0. \tag{1.8}$$

The final expression for two EPs are:

$$\lambda_1 = \frac{-i(\omega_1 - \omega_2)}{i(\epsilon_1 - \epsilon_2) + 2\sqrt{\delta_1\delta_2}}$$
$$\lambda_2 = \frac{-i(\omega_1 - \omega_2)}{i(\epsilon_1 - \epsilon_2) - 2\sqrt{\delta_1\delta_2}}.$$

At these EPs, the system exhibits various unique properties that make it significantly different from a normal Hermitian system. First, EPs are different from eigenvalue degeneracies encountered for Hermitian operators. At the EP, there is only one eigenvector rather than two for degeneracy case. Second, the matrix $H(\lambda)$ cannot be diagonalized due to the existence of only one eigenvector [100]. Third, the derivative with respect to λ of the eigenvalues and eigenvectors is infinity at the EPs. Forth, a chiral behaviour exists when going around the EPs, going clockwise and counterclockwise will give opposite sign.

All these mathematical properties related to EPs have their own physical meanings and lots of work has been done in realizing them in physical systems [101–103]. As for our work on photonic topological insulators, the intrinsic loss of components will make our system non-Hermitian and introduce EPs. We theoretically and experimentally demonstrate a direct relationship between these non-Hermitian EPs and Hermitian topological edge invariants.

1.5 Motivation of our work

Proving the existence of topological nontrivial band structure is a very important in the area of topological insulator research. In condensed-matter systems, topologically nontrivial band structures will cause certain macroscopic transport properties to be precisely quantized. Most famously, in the integer QH effect, the Hall conductance is quantized to integer multiples of the inverse von Klitzing constant to nearly one part in 10^9 [37]. Thouless provided an influential explanation for this [91], which showed using linear response theory that the QH conductance is tied to the Chern numbers of the bands, which are "topological invariants" restricted to integer values. Therefore, the existence of topological nontrivial state can be proved by direct measurement of the Chern number in the system.

In photonics, the situation is different from that in condensed physics, there is no direct analog of the Hall conductance or similar linear response-based quantity, due to the absence of a fermionic ground state [41, 42]. As a result, direct measurement of "topological invariant" becomes very difficult and edge propagation measurements [55, 74, 79, 93] have served almost exclusively as the signature for topologically nontrivial photonic band structures.

In order to provide a new platform for the research of floquet topological insulator and a new method to demonstrate the existence of topological nontrivial band structure in this kind of network system, we borrow the idea of "topological pump" [104] proposed by Laughlin et al., and map the network system into a two-dimensional two-ports system. We further proves the direct relation between the winding behavior of the eigenvalues of system S matrix and the topological edge invariant in the original photonic topological system. By measuring the winding behavior of system eigenvalues, we are able to distinguish topological nontrivial band structure from normal insulators. In this way, we provide a totally new method which is completely different from edge mode propagation measurement for the research of photonic topological insulators. Meanwhile, our works proves similar network structure can also be mapped into this kind of system which will give them a practical way to investigate the properties of the original system.

Later, based on the first experiment, we want to provide a better platform for the research of photonic topological insulator by compensating losses in the system. During this process, fortunately, we found it is possible to introduce exceptional

points into the system using balanced gain and loss. This discovery provide numerous possibility for our platform, which means the system can be used to investigate topological edge invariant and exceptional points at the same time.

1.6 Summary

In this chapter, we started from the concept of topology in mathematics and introduced the idea of topological invariants which are used to characterize topological spaces. Then, the topological insulator, one of the most important discoveries in physics in the past few decades, was discussed. The differences between this new phase and normal insulators, the history of topological insulator, the topological pump idea, and the network models for topological insulator were all described in detail. We then discussed the development process of photonic topological insulators, which are recently discovered variety of topological insulator and is the major topic of this thesis. Later, the concept of exceptional points was introduced. After all these, our motivation to build a platform for photonic topological insulator is presented.

The structure of the following parts of this thesis are as follows. Chapter 2 presents our first experimental measurement of a topological edge invariant in a microwave network, based on winding numbers of eigenvalues of the S matrix. Chapter 3 will show our improved experiment setup which demonstrates a direct relationship between a Hermitian topological edge invariant and non-Hermitian exceptional points. Chapter 4 will give a summary for all the works in this thesis.

Chapter 2

Measurement of a Topological Edge Invariant

In this chapter, I will introduce Hafezi's coupling resonator model and our understanding of this model first. Then, the bandstructure of this kind of topological network model will be presented. Later, combining the idea of topological pump, I will describe the process of mapping two-dimensional Floquet topological insulators into microwave network. After that, the transfer matrix description method of the system will be analyzed in detail. Finally, our simulation and experimental result will be shown.

2.1 Network model

Hafezi's system design is very similar to coupled resonator optical waveguide (CROW) structures. Hence, I will discuss CROW structures first, then present Hafezi's design, and finally describe our variant of this coupled resonator system.

2.1.1 CROW structure

To implement an optical waveguide, many mechanisms have been proposed and realized. The most widely used one is based on total internal reflection as shown in Fig. 2.1(a). The reflection happens at the interface between two different dielectric

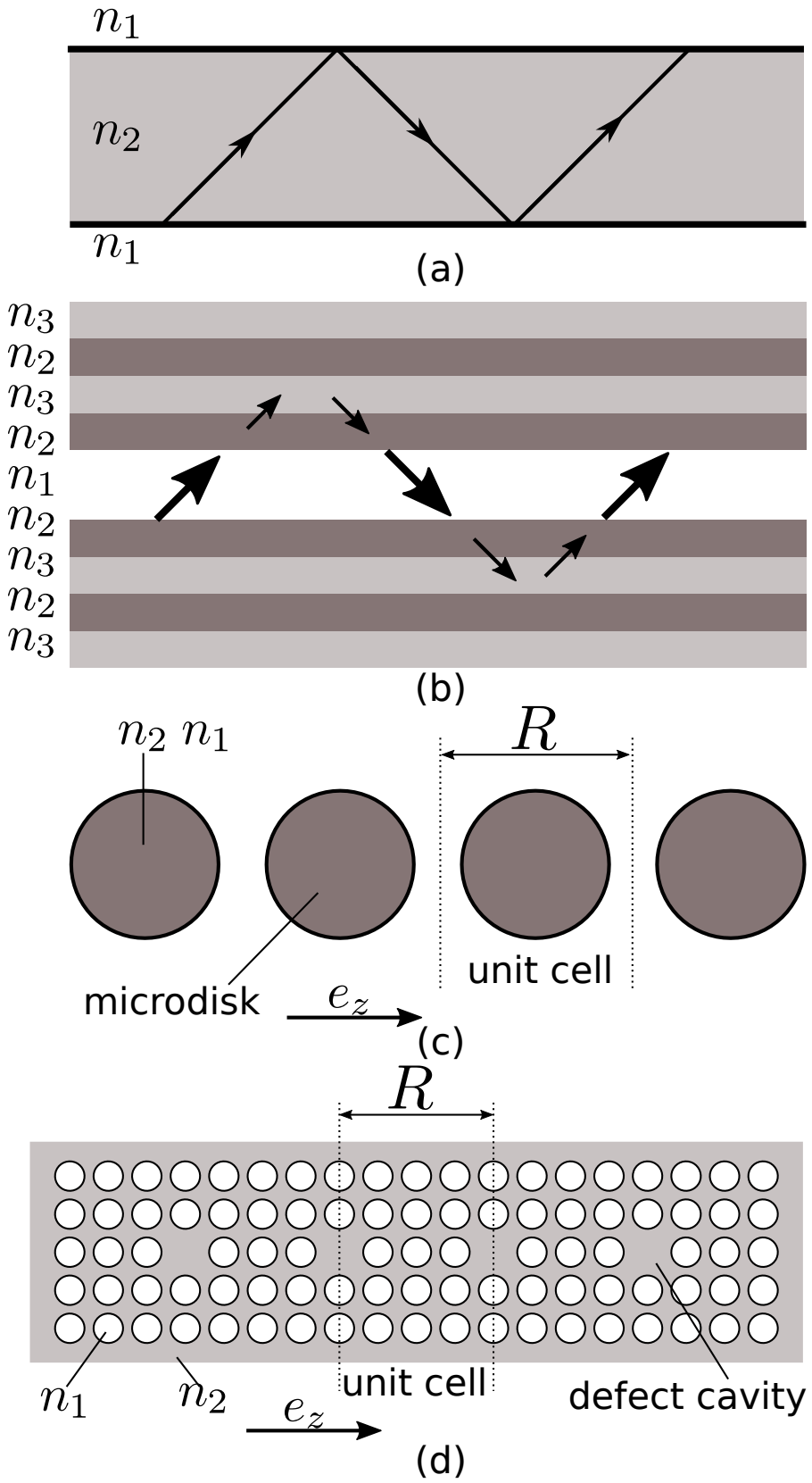

FIGURE 2.1: Three types of waveguiding. (a) total internal reflection waveguide, where total reflection happens at the interface between two different dielectric media with refractive index n_1 and n_2, $n_2 > n_1$. (b) Bragg waveguide, implemented using Bragg stacks. (c) CROW, achieved through coupling between individual microdisks. (d) CROW, realized by coupling of individual defect cavities in a 2D photonic crystal. R is the diameter of unit cell, and e_z is the direction of the periodicity for the coupled resonators.

media, with reflection index n_1 and n_2 where $n_2 > n_1$. According to Snell's law, if the incident angle is larger than the critical angle, total reflection occurs. Conventional optical fibers are the most successful application of this kind of optical waveguide. Another important optical waveguide, shown in Fig. 2.1(b) is achieved through Bragg reflection from a periodic structure. A third kind of optical waveguide is the CROW. One type of CROW is based on coupling between individual microdisks as shown in Fig. 2.1(c). When two resonators are close to each other, there will be evanescent coupling between them and the coupling strength is related to the separation distance. By controlling this gap width, we can modulate the transmission through a line of resonators. Another CROW design is based on coupling of individual defect cavities in a 2D photonic crystal as shown in Fig. 2.1(d). By carefully designing the structure, the resonator frequency of defect resonators falls into the band gap of the surrounding photonic crystal, and energy can be transported via coupling through a line of defect resonators.

2.1.2 Hafezi's theory of coupled resonator system

Based on 1D CROW theory [105], Hafezi *et al.* designed a 2D resonator network which is a 2D arrangement of ring resonators, shown in Fig. 2.2. In this network, ring resonators support degenerated clockwise and counter-clockwise modes which act as two pseudo-spins. Photons travel from one resonator to another though evanescent coupling between neighbor rings. The length of resonator and connecting waveguide are specifically chosen so that modes will be confined in the resonators rather than connecting waveguides. Moreover, the upper and lower branches of each coupling ring are different, as a result, the photon acquires different phase shifts when it travels through a connecting waveguide in different directions. The length difference between upper and lower branches are designed so that each photon acquires a $2\pi\alpha$ phase when it travels a around a plaquette, as indicated by the green line. This acquired extra Aharonov-Bohm phase is equivalent to α quanta of magnetic flux penetrating each plaquette [106]. Using this kind of implementation, Hafezi *et al.* successfully realize a photonic topological insulator system.

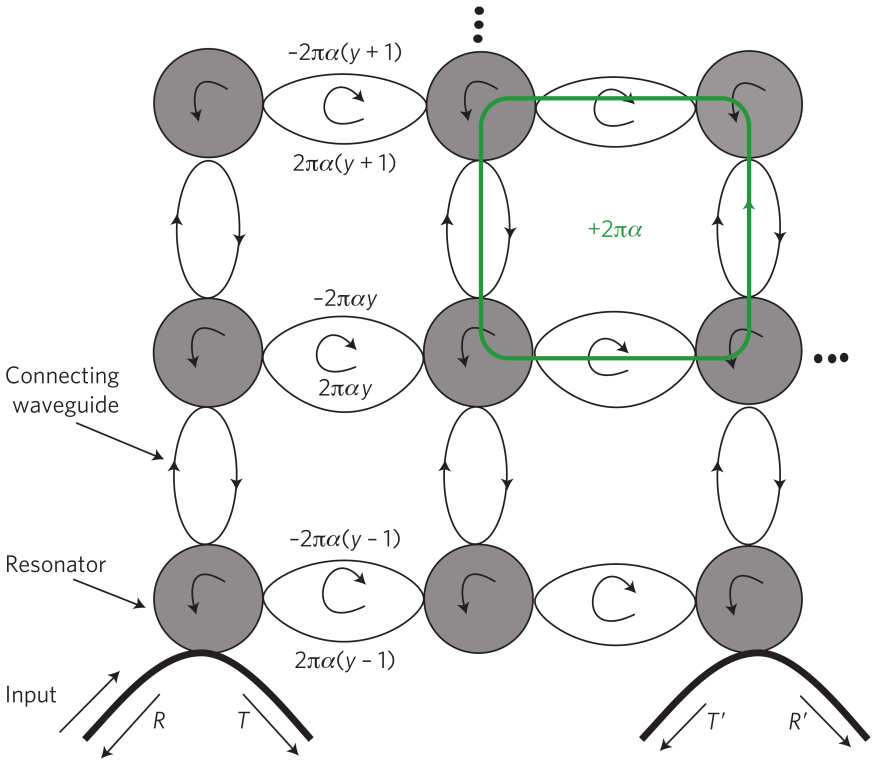

FIGURE 2.2: Hafezi's network model. The network is a 2D arrangement of 1D CROW structure. The length of resonators (dark circles) and connecting waveguides (white ovals) are designed that modes will be confined inside resonators. The connecting position of connecting waveguides are shift through different lines so that a photon will acquire a $2\pi\alpha$ phase when it go around the green line once and this is equivalent to α quanta of magnetic flux penetrating each plaquette. y is the site index in the vertical direction, each shift of the white oval will introduce a phase difference of $2\pi\alpha$, for site y, the corresponding phase introduced by upper edge and lower edge are $-2\pi\alpha y$ and $2\pi\alpha y$. Figure taken from [47].

2.2 Periodic square lattice network model

Our coupled resonator system is shown in Fig. 2.3(b). It is also based on 2D CROW structure, but is fully periodic, there is no position shift for the connecting waveguides which means there is no direct analogy to a magnetic system. As before, the direction of propagation of light within each ring plays the role of a pseudo-spin, and we assume no coupling between different pseudo spins. As shown in Fig. 2.3(a), each resonator can be divided into four quarter rings and each quarter ring introduces ϕ phase delay. Each resonator is coupled with four neighbor resonators; the coupling strength is denoted by θ. The realization of

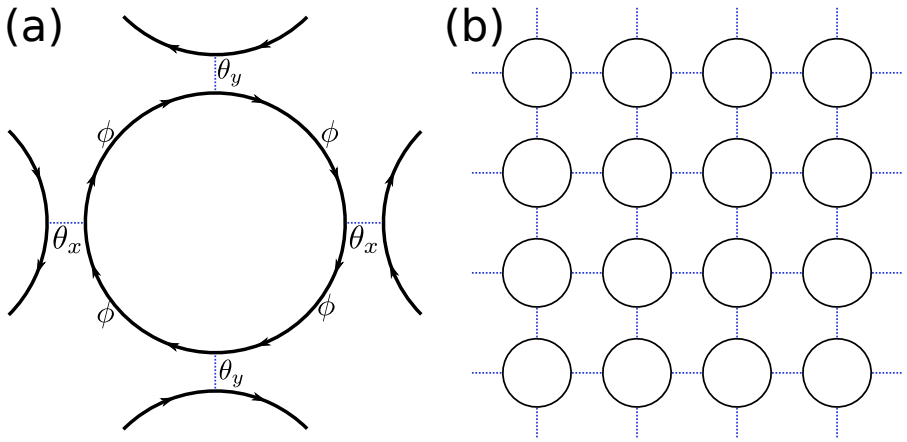

FIGURE 2.3: (a) Schematic of the resonator, each resonator ring is divided into four equal quarter rings with ϕ phase delay. Each resonator is coupled with four neighboring resonators, the coupling strength is depicted using θ. (b) Schematic of our resonator lattice network.

this coupling can be based on either evanescent coupling between adjacent ring resonators, or direct conventional couplers (see Section 2.1.1).

We can compare topologically trivial and topologically non-trivial phases of the network model by calculating their projected band structures. For simplicity, a ten-cell wide strip is used for all calculations in this section. All the couplers in the system are exactly the same with coupling strength described by θ.

As described in the previous section, our coupled resonator lattice is a "zero-magnetic field" system and this kind of system appears to be topologically trivial in tight-binding analysis [47]. However, in fact the system will show a topological insulator phase if the interresonator coupling is strong enough. To be more precise, the coupled resonator lattice in Fig. 2.3(b) is in a topologically trivial states when $\theta < \pi/4$ and in a topologically non-trivial phase when $\theta > \pi/4$ [49, 51]. Detailed calculations will be presented in Section 2.4.

The projected band diagram for a semi-infinite strip is shown in Fig. 2.4. For $\theta < \pi/4$, the system is a trivial insulator. Fig. 2.4(a) shows the result for $\theta = 0.1\pi$. For some ϕ, edges modes exist, but these modes are two-way modes; there are states with both positive and negative velocities, confined to the same edge at different K_x for each ϕ. $\theta = 0.25\pi$ is the critical value where the gap of band structure closes as shown in Fig. 2.4(b). For $\theta > 0.25\pi$, the system is in a topologically non-trivial phase. Fig. 2.4(c,d) shows the bandstructures for $\theta = 0.3\pi$ and $\theta = 0.4\pi$ respectively; it is clear that unidirectional edge modes appear in the bandgaps.

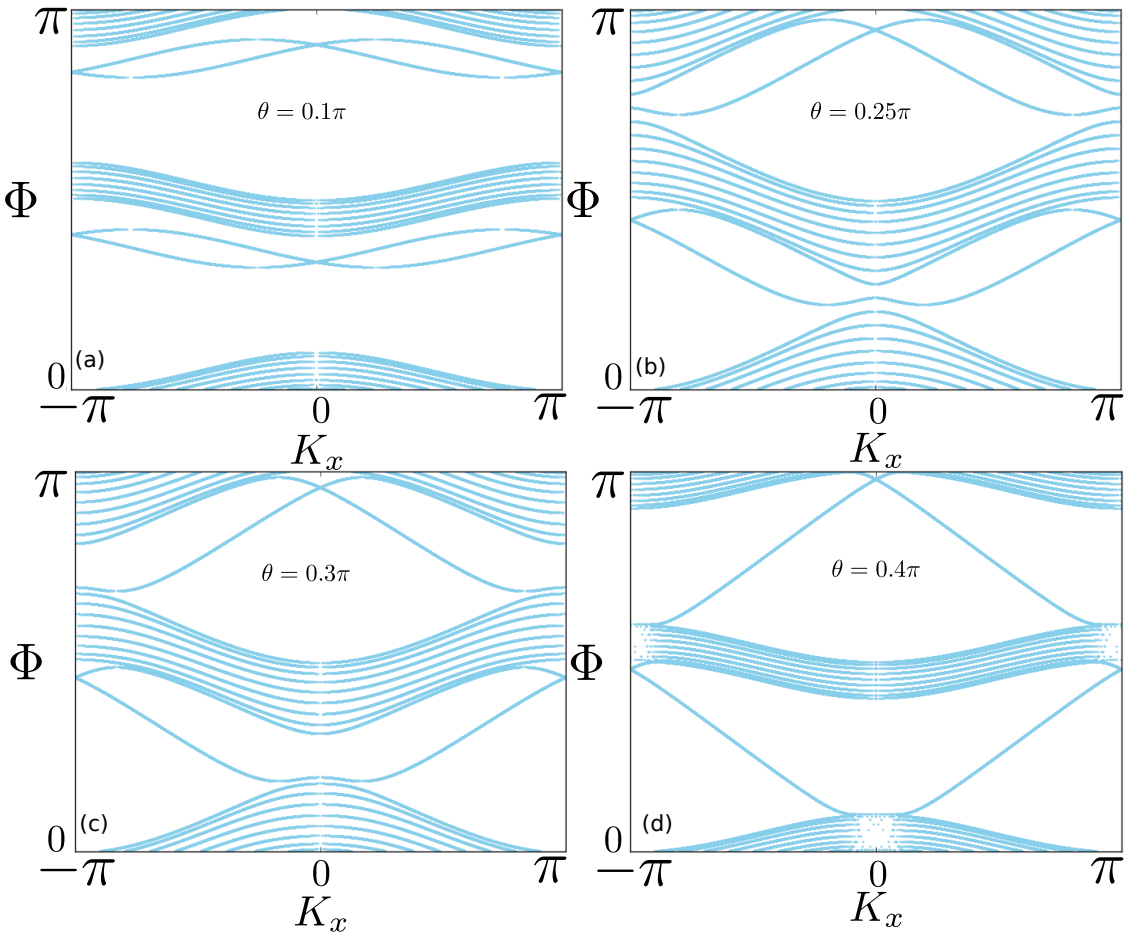

FIGURE 2.4: Projected band structure for coupled resonator system. $\theta = \pi/4$ is the critical point for this system where the band gap closed. For $\theta < 0.25\pi$, two-way edge states exist are confined at same edge. For $\theta > 0.25\pi$, the band gap reopen and uni-directional edge state exists.

To be more specific, there is a positive velocity upper edge state and a negative velocity lower edge state.

2.3 Experiment setup

A topological pump is an experiment that is specially designed to reveal the topological properties of a 2D lattice. As shown in Fig. 2.7(b), it consists of rolling a 2D lattice into a cylinder, inducing a phase "twist" k in the azimuthal boundary conditions, and performing a transport measurement in the axial direction (i.e., at the edges of the cylinder). In the original Laughlin's thought experiment [104], the twist is implemented by adiabatically threading magnetic flux through

the cylinder, which produces an Aharonov-Bohm phase shift while also transporting electron wave functions in the axial direction. Threading one magnetic flux quantum induces a 2π phase shift; by gauge invariance, the number of transported electrons must be an integer. From this, the quantization of the Hall conductance can be derived [104]. A more detailed description of this thought experiment is given below, in Section 2.3.1.

An alternative formulation of the topological pump, based on wave scattering, has been developed by Brouwer and co-workers [107, 108]. Here, one imagines taking a similar cylinder and scattering electron waves (or electromagnetic waves, as the case may be) off one edge, at an energy (or frequency) that lies in a bulk band gap. As the twist angel k advances by 2π, the reflection matrix r is measured. For a sufficiently long cyclinder and/or a sufficiently large band gap, transmission to the opposite edge is negligible and r is unitary; its eigenvalues lie on the unit circle, and their trajectories during a pumping cycle can be topologically characterized by a winding number. A nonzero winding number corresponds to a topologically nontrivial sample. This is tied to the existence of topological edge states.

2.3.1 Laughlin's adiabatic pumping experiment

In 1981, Laughlin proposed a thought experiment for measuring the quantization of quantum Hall conductivity of two-dimensional metals [104]. Fig. 2.5(a) is a schematic diagram of our infinite 2D network model, which can be rolled up into a cylinder like Fig. 2.5(b). The Hamiltonian in y direction can be written as

$$H = \sum_{k_y} H_1(k_y) \tag{2.1}$$

$$= H_1(0) + H_1(\Delta k) + \cdots + H_1((N_y - 1)\Delta k), \tag{2.2}$$

where k_y is the Bloch quasi-momentum. If a vector potential $\vec{A} = A_y\vec{y}$ is introduced into the system, we have $k_y \to k_y + \frac{eA_y}{\hbar}$, then the Hamiltonian becomes

$$H = \sum_{k_y} H_1(k_y + \frac{e}{\hbar}A_y) \tag{2.3}$$

$$= H_1(0 + \frac{e}{\hbar}A_y) + H_1(\Delta k + \frac{e}{\hbar}) + \cdots + H_1((N_y - 1)\Delta k + \frac{e}{\hbar}A_y). \tag{2.4}$$

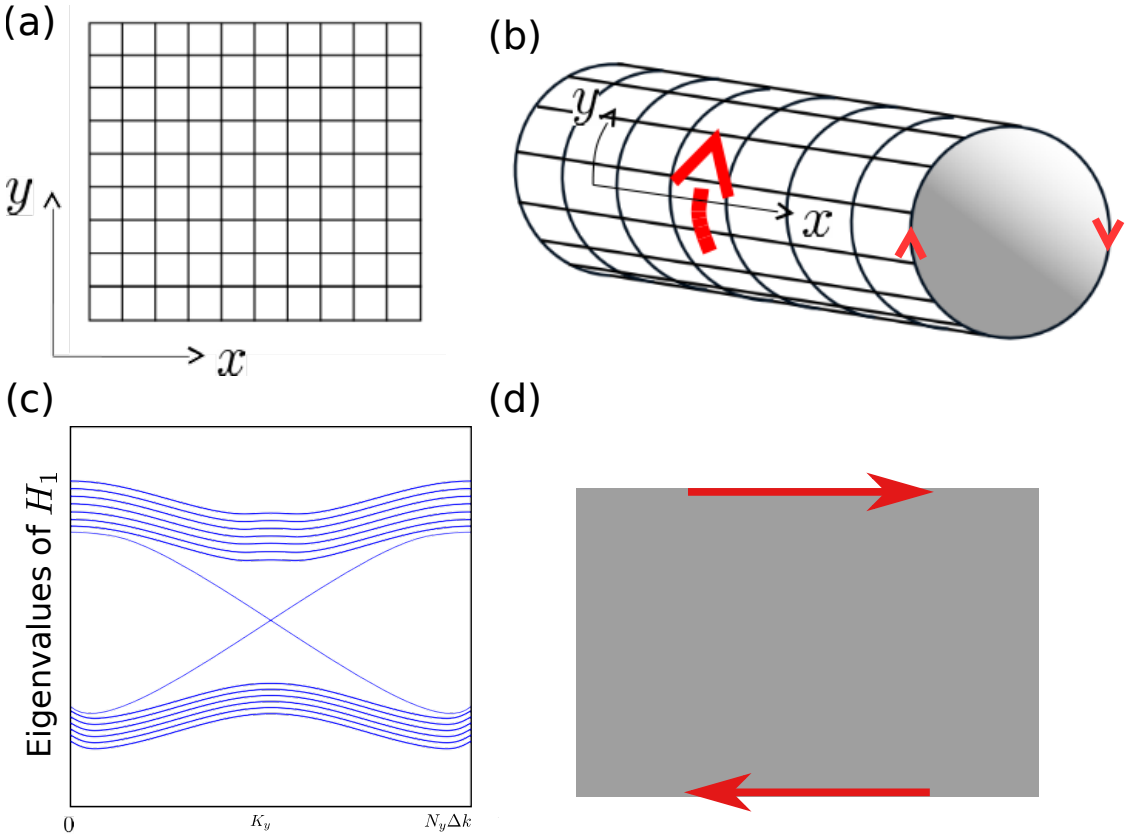

FIGURE 2.5: (a) 2D infinite network model. (b) The network model is rolling into a cyclinder and a vector potential is added to the surface along the y direction. (c) Projected band structure of the system. (d) Edge states appear.

If $\frac{eA_y}{\hbar} = \Delta k_y$, we have

$$H = H_1(\Delta k) + H_1(2\Delta k) + \cdots + H_1(N_y\Delta k). \tag{2.5}$$

Hence, the Hamiltonian comes back to itself under the condition

$$\frac{eA_y}{\hbar} = \Delta k_y = \frac{2\pi}{2\pi R} \quad i.e. \quad A_y = \frac{h}{2\pi eR}. \tag{2.6}$$

Fig. 2.5(c) is the projected band structure for the system. The unidirectional edge states exist at the edge of the system as indicated in Fig. 2.5(d). This adiabatic pumping setup is nice and provide a possible way to measure the quantization of quantum Hall conductivity. To implement this experiment setup, an adiabaticaly threading magnetic flux through the cyclinder is needed, which will introduce the vector potential ($\vec{A}$) in y direction. However, it is not practical to generate such a magnetic flux in experiment and this experiment has never been experimentally

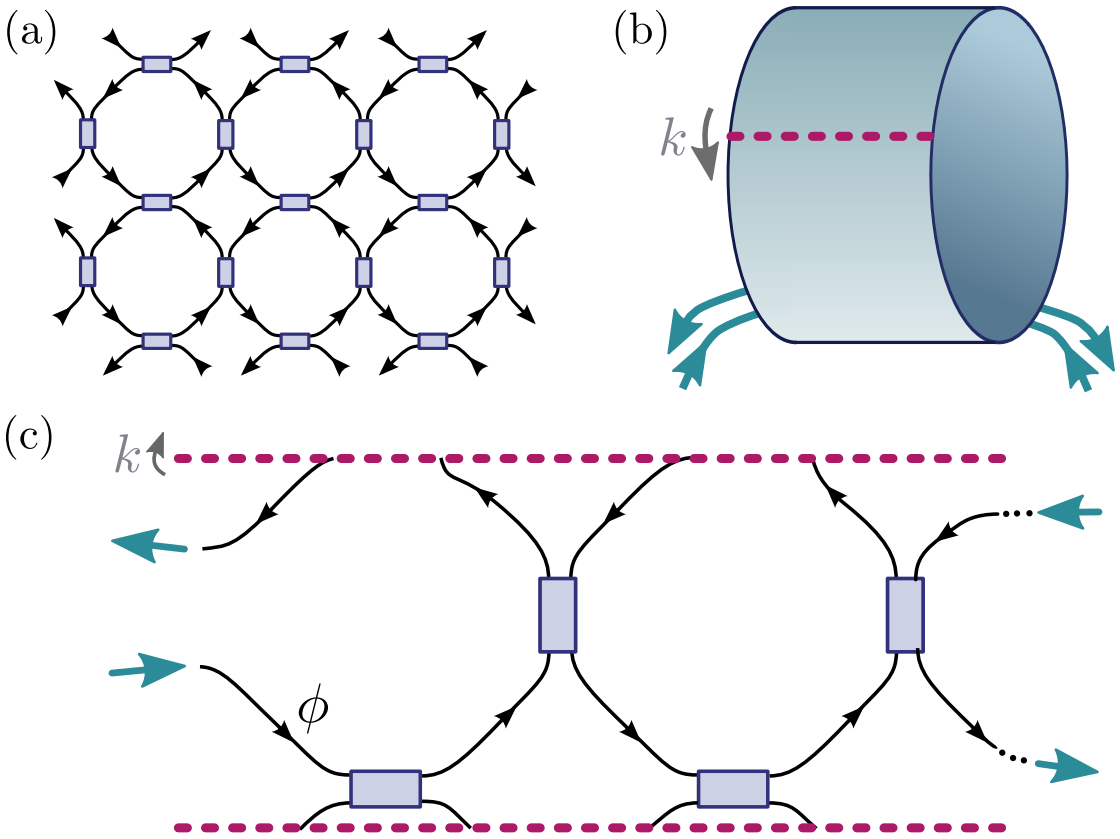

FIGURE 2.6: (a) Schematic of a periodic 2D directed network. Wave amplitudes undergo phase delay ϕ along each directed link (black arrows), and couple through a 2×2 unitary matrix at each node (blue boxes). (b) In a "topological pump" setup, a 2D system is rolled into a cylinder; twisted boundary conditions with tunable twist angle k are applied, and a transport measurement is performed in the axial direction (cyan arrows). (c) Topological pump setup for a network model, with a cylinder comprising one unit cell in the azimuthal direction and two cells in the axial direction.

realized.

2.3.2 Mapping procedure from 2D lattice to 1D network

Following Laughlin's idea, let's think about a specific periodic (disorder-free) network shown in Fig. 2.6(a), which consists of unit cells arranged in a 2D square lattice, each cell containing two nodes and four directed links. A "solution" to the network is a set of wave amplitudes (complex scalars) defined along the links, such that (i) traversing each link incurs a phase delay ϕ (which we take to be the same for all links), and (ii) the amplitudes entering and leaving each node are related by a fixed 2×2 coupling matrix. Let the complex vector $|\psi\rangle$ be the collective set of

wave amplitudes exiting the links, and $|\psi'\rangle = e^{-i\phi}|\psi\rangle$ be the amplitudes entering the links. The individual node coupling matrices can be composed into a matrix U that relates the amplitudes entering and leaving the nodes. These amplitudes must be equal to $|\psi\rangle$ and $|\psi'\rangle$ respectively, so

$$U|\psi\rangle = e^{-i\phi}|\psi\rangle\,. \tag{2.7}$$

For an infinite periodic network, we look for solutions obeying Bloch's theorem. Then Eq. (2.7) reduces to [49, 51]

$$U_k|\psi_{nk}\rangle = e^{-i\phi_n(k)}|\psi_{nk}\rangle\,, \tag{2.8}$$

where n is the band index, k is the quasimomentum, and $\phi_n(k)$ is the band "quasi-energy". In the absence of gain or loss in the network, U_k is unitary, and $\phi_n(k)$ is real. But unlike a usual band energy, it is an angle variable.

Interestingly, Eq. (2.8) has the same form as the evolution equation for a lattice with a time-periodic Hamiltonian, where U_k is the evolution operator over one period and $|\psi_{nk}\rangle$ is a Floquet state of the driven lattice. Recently, several groups have proposed a new class of topological insulators called "Floquet topological insulators", where the topological behavior arises from periodic drives (such as oscillating electric fields). It has been shown that a driven system can have a topologically nontrivial *quasi-energy* bandstructure, even if the undriven *energy* bandstructure is topologically trivial [75, 76, 109–113].

In most respects, quasi-energy bandstructures have the same behaviors as energy bandstructures. If quasi-energy bands have nonzero Chern numbers (as calculated from $|\psi_{nk}\rangle$ in the usual way [91]), topological edge states will exist; this is the case demonstrated in a recent photonic realization of a Floquet topological insulator [74]. However, a quasi-energy bandstructure can also be topologically nontrivial *even if all Chern numbers are zero* [75]. This case, which we call the "anomalous Floquet insulator", is possible because $\phi_n(k)$ is an angle variable; for example, every band can receive +1 to its Chern number from the band above and -1 from the band below, resulting in zero net Chern number even though all bandgaps are topologically nontrivial. For driven systems, Rudner *et al.* have proposed an alternative topological bulk invariant which can characterize this situation [113]. The topological nontriviality of an anomalous Floquet insulator can also be verified

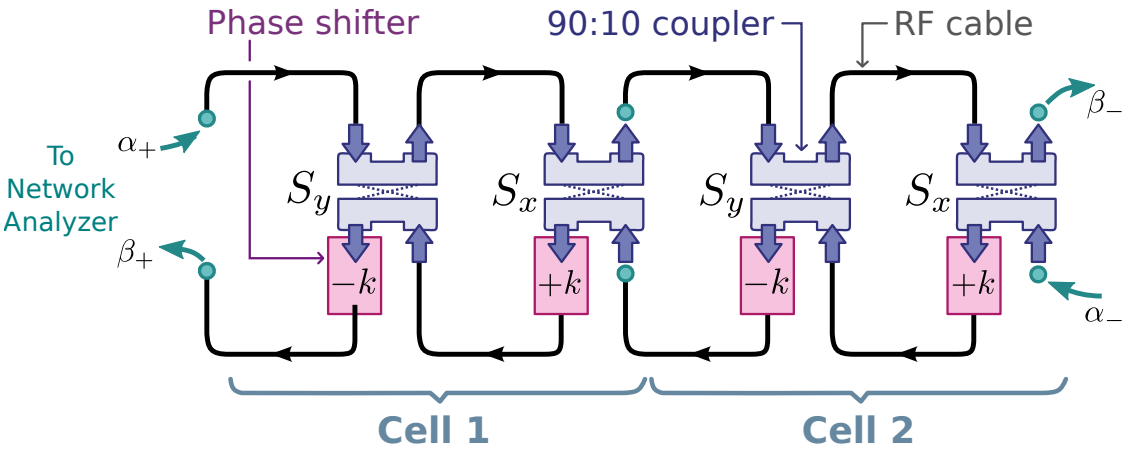

FIGURE 2.7: Experimental setup. Each of the identical units, labeled here "Cell 1" and "Cell 2", corresponds to one cell in the topological pump geometry of Fig. 2.6. A pair of phase shifters in each cell (pink boxes), with shifts of $+k$ and $-k$ respectively, implement the twisted boundary condition. The couplers (blue rods) are depicted in the "strong coupling" configuration; the "weak coupling" configuration is achieved by swapping each coupler's outputs. The isolators connected to coupler ensure the uni-directional tranmission in this network and the energy flow direction is indicated by the arrows. The overall input and output amplitudes are $\alpha_\pm$ and $\beta_\pm$; their scattering parameters are measured with a network analyzer.

from the presence of topological edge states, and from its behavior under topological pumping (as described in the next section) [51].

Let's go back to Laughlin's thought experiment as shown in Fig. 2.6(b), rolling the 2D lattice into a cyclinder, inducing a phase "twist" k in the azimuthal boundary, and performing a transport measurement in the axial direction (i.e., at the edges of the cylinder). To realize this experiment setup, we "cut" the system along the red line as shown in Fig. 2.6(b), and map it into the 1D network model shown in Fig. 2.6(c), which consists of links, couplers, and a phase "twist" k in its edge.

2.3.3 Details of our microwave experiment implementation

Our experimental setup is shown in Fig. 2.7. The network is divided into identical subunits, each consisting of 4 cables, 2 phase shifters, and 2 couplers. By comparison with Fig. 2.6(c), each subunit is equivalent to a "cylinder" in the topological pump setup that is one cell wide and one cell long. Connecting the subunits in series forms a longer cylinder; Fig. 2.7 shows a "two-cell" configuration.

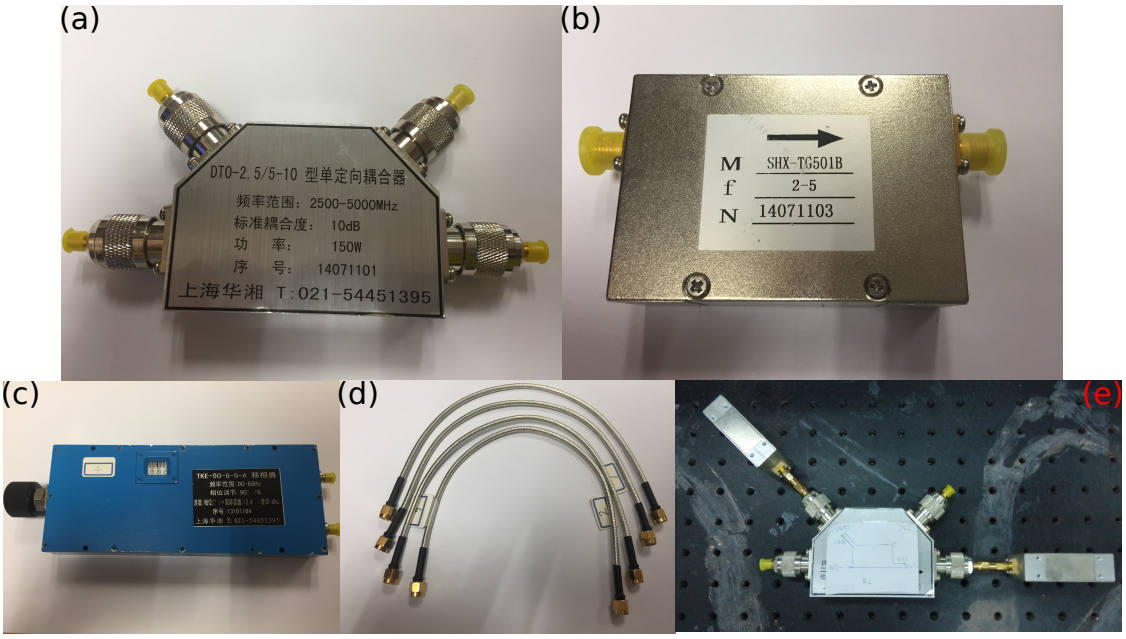

FIGURE 2.8: Photographes for the experimental components. (a) Four port directional coupler. (b) Isolator. (c) Phase shifter. (d) RF cables. (e) directional coupler connected to isolators, two inputs have internal isolator, two isolators are connected to two output ports.

For this experiment to measure topological edge invariant, there are several requirements for our experiment setup:

- Uni-directional transmission must be ensured. Our system is a direct map of a photonic topological insulator, in which both clockwise and counter-clockwise edge states are supported by the system. If energy transmission in both directions are allowed, the energy will neutralize with each other and nothing can be measured. As a result, isolator in our chosen wavelength must exist.

- Phase shift in range of $[0, 2\pi]$ must be achieved. In this experiment, our goal is to measure the topological edge invariant by observing the winding behavior of system eigenvalues. Our system is a direct map of a photonic topological insulator, which maps full k space from $[-\infty, \infty]$ to $[0, 2\pi]$. To get complete eigenvalue trajectory, k must be swept in the range $[0, 2\pi]$. Therefore, the phase shifter must be tunable from 0 to 2π in our chosen wavelength.

- Wavelength must be large enough to ensure the cable length change introduced by mechanical vabriation can be neglected. In our experiement, mechanical vabriation is inevitable, which will introduce a varing length Δl to

each cable. This varing length Δl will introduce a varing phase shift $2\pi\Delta l/\lambda$ (λ is the wavelength). This Δl is in the magnitude of about 0.1% of the cable length. As a result, the chosen wavelength must be much larger than this extra varing length.

In order to fullfill all these requirements, 5GHz is chosen as the experiment wavelength. For which, the wavelength is $\lambda \approx 0.6m \gg \Delta l \approx 10^{-4}m$ and all necessary components are available.

The cables are standard low-loss coaxial RF cables as shown in Fig. 2.8(d). The length of each cable is about $\sim$15 cm, and the cable uses standard SMA connectors. Fig. 2.8(a) is the coupler we used in our experiment, which are four-port single-directional couplers, with isolators built into each input port. The coupling ratio is approximately 90:10, the frequency range is 2.5 GHz - 5 GHz, the model is DTO-2.5/5-10 from Shanghai Huaxiang Computer Ltd. For the two output ports of the coupler, two isolators are connected as shown in Fig. 2.8(b) to ensure the uni-directional transmission in our experiment, the model for the isolators we used is SHX-TG501B from Shanghai Huaxiang Computer Ltd., and it can work in the frequency range of 2 GHz - 5 GHz. Fig. 2.8(c) is the phase shifter we used in our experiment; each phase shifter can be tuned independently which makes it possible to produce $+k$ and $-k$ phase shifts to drive the topological pump. The model of phase shifter is TKE-90-6SA from Shanghai Huaxiang Computer Ltd; the working frequency is DC-6GHz, and the introduced phase shift is 90°/GHz which means at most 2.5π can be added into the system at 5 GHz. As we know, for microwave waveguides, the loss is positively related to the operation frequency; the higher the frequency, the higher the loss. Taking everything into consideration, the operating frequency is chosen to be 5 GHz, low enough to reduce losses in the various components while high enough to allow phase shifts in the full range $k \in [0, 2\pi]$.

Connecting all the components together as indicated in experiment schematic as shown in Fig. 2.7, we get a traditional two-port system. The system's S matrix can be easily measured using a vector network analyzer. The machine we used is an Anritsu 37396C, which can work up to 40 GHz. The S matrix of our network is defined as

$$S \begin{bmatrix} \alpha_+ \\ \alpha_- \end{bmatrix} = \begin{bmatrix} \beta_+ \\ \beta_- \end{bmatrix}, \tag{2.9}$$

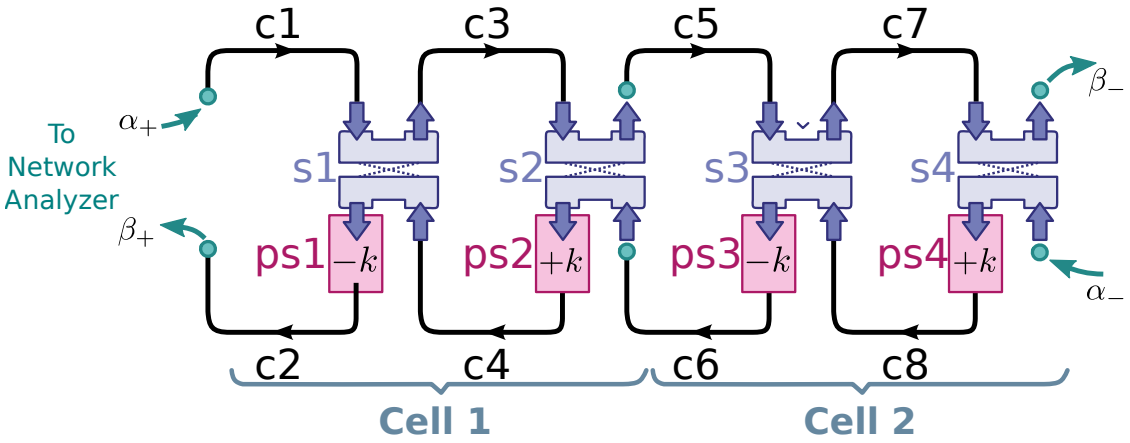

FIGURE 2.9: Experiment setup to measuring a topological edge invariant. All the components are indexed.

where $\{\alpha_\pm, \beta_\pm\}$ are the input and output wave amplitudes at the two edges, as labeled in Fig. 2.7.

Since the couplers have fixed coupling ratios, we are unable to continuously vary the network's coupling strength parameter, on which the bandstructure topology depends. However, by swapping the order of each coupler's output ports, we can switch between the two cases of a topologically trivial and nontrivial bandstructure. As described in Section 2.3.2, the strength of each coupler is described by a parameter $\theta \in [0, \pi/2]$, where $\theta = 0$ corresponds to zero coupling between adjacent unit cells and $\pi/2$ is complete coupling. The bandstructure is topologically trivial for $\theta < \pi/4$, and nontrivial for $\theta > \pi/4$, independent of all other coupling matrix parameters. Our 90:10 couplers thus allow for either $\theta \approx \tan^{-1}(3) \approx 0.40\pi$ (topologically nontrivial; this is the configuration shown in Fig. 2.7) or $\theta \approx \tan^{-1}(1/3) \approx 0.10\pi$ (topologically trivial). At the 5 GHz operating frequency, each cable has phase delay $\approx 0.2\pi$, which lies in a bandgap of the quasi-energy bandstructure for both the strong and weak-coupling cases. The loss in each cable is ≈ 0.4dB.

2.3.4 Experiment measuring procedure

After setting up the experiment described in Section 2.3.3, the next step is to get the data we want. For our experiment, the most important thing is that all the states are repeatable. The measurement procedure of our experiment can be divided into following steps.

cables	loss/dB	phase/rad	complex
c1	-0.34	0.5899	0.7991 + 0.5349i
c2	-1.57	0.6039	0.6871 + 0.4739i
c3	-0.4	0.6021	0.7870 + 0.5409i
c4	-2.32	0.5899	0.8015 + 0.5008i
c5	-0.49	0.5585	0.6835 + 0.4840i
c6	-1.54	0.6161	0.6362 + 0.4259i
c7	-0.6	0.6091	0.7654 + 0.5339i
c8	-1.93	0.6065	0.6579 + 0.4564i

TABLE 2.1: Measured data for RF cables

Step 1: Measuring each component separately. The components are labeled as indicated in Fig. 2.9, then we measure both loss and phase information for each component. These data will be used for simulation and predicting experiment results. For simplicity, each coupler and the isolators connected to it are considered as a whole, and the loss of the phase shifter is added to the RF cable connected to it. For example, the loss of cable c2 is the sum of losses for both cable c2 and phase shifter ps1. The situation for cable c4, c6, and c8 is the same as cable c2. Moreover, the loss of each phase shifter will change as we tune it; hence, the loss for cables with even index will also alter for each value of $\pm k$. Measured data for RF cables (losses of phase shifters at O° is counted), coupler S matrix and losses for phase shifter at different value of k are shown in Table. 2.1, Table. 2.2, and Table. 2.3 respectively. Based on the data shown in Table. 2.3, interpolation is used to generate loss data for all values of k, and the result is shown in Fig. 2.10. This result will be used in simulations.

Step 2: Simulation of experiment results. With all the data we measured at step 1, simulation results can be generated using the transfer matrix method described in Section 2.4. The eigenvalue and phase information are presented in Fig. 2.11 and Fig. 2.12 respectively. It is clear that winding behavior exists for the strong coupling network, but not for the weak coupling network. However, due to limited system size (at most two cells), gaps occurred at the projected curves. Similar information can also be read out from the phase figures. Meanwhile, the losses of components we used make the system non-Hermitian, therefore, the S matrix eigenvalues are located inside the unit circle.

Step 3: Measuring data. We set up the system by connecting all the components together as indicated by our experiment design (Fig. 2.9). For the experiment,

Coupler s1	loss/dB	phase/rad	complex
S11	-1.5397	-0.0855	0.8345 - 0.0715i
S12	-12.0186	1.3842	0.0465 + 0.2463i
S21	-11.8594	1.6092	-0.0098 + 0.2551i
S22	-1.2297	-0.454	0.8671 - 0.0394i
Coupler s2	loss/dB	phase/rad	complex
S11	-1.4803	-0.7802	0.5994 - 0.5932i
S12	-11.6390	1.1921	0.0968 + 0.2433i
S21	-12.5189	0.9408	0.1394 + 0.1912i
S22	-1.3897	0.0104	0.8521 + 0.0089i
Coupler s3	loss/dB	phase/rad	complex
S11	-1.5097	-0.1745	0.8277 - 0.1459i
S12	-11.7395	1.3772	0.0498 + 0.2540i
S21	-11.6293	1.4261	0.0378 + 0.2594i
S22	-1.2996	-0.1204	0.8548 - 0.1034i
Coupler s4	loss/dB	phase/rad	complex
S11	-1.4504	-0.1658	0.8346 - 0.1397i
S12	-11.6786	1.4101	0.0417 + 0.2573i
S21	-11.5805	1.5829	-0.0032 + 0.2636i
S22	-1.6404	-0.0017	0.8279 - 0.0014i

TABLE 2.2: Measured data for couplers

k/π	0	0.2	0.4	0.6	0.8	1.0	1.2	1.4	1.6	1.8	2.0
ps1/dB	0.96	1.01	1.04	1.02	0.96	0.82	0.76	0.8	0.77	0.81	0.8
ps2/dB	0.77	0.72	0.65	0.6	0.55	0.53	0.59	0.7	0.83	0.91	0.89
ps3/dB	0.93	1	1.02	0.92	0.74	0.68	0.65	0.75	0.87	0.89	0.84
ps34/dB	0.83	0.84	0.8	0.7	0.72	0.83	0.96	1	0.95	1.08	0.97

TABLE 2.3: Measured data for phase shifters

we measure data for 31 values of k, 12° stepwidth, in the range of $[0, 2\pi]$. For each point, we measure the S matrix information by collecting both transmission amplitude and phase of S_{11}, S_{12}, S_{21}, and S_{22}. Then, the eigenvalue and eigenvalue phase can be calculated.

2.4 Transfer matrix describe of the system

From Section 2.3.2, we know that a 2D directed network like that shown in Fig. 2.6(a) can be mapped into a 1D two-port network system as shown in Fig. 2.6(c), which can in turn be experimentally realized in microwave realm. For this two-ports

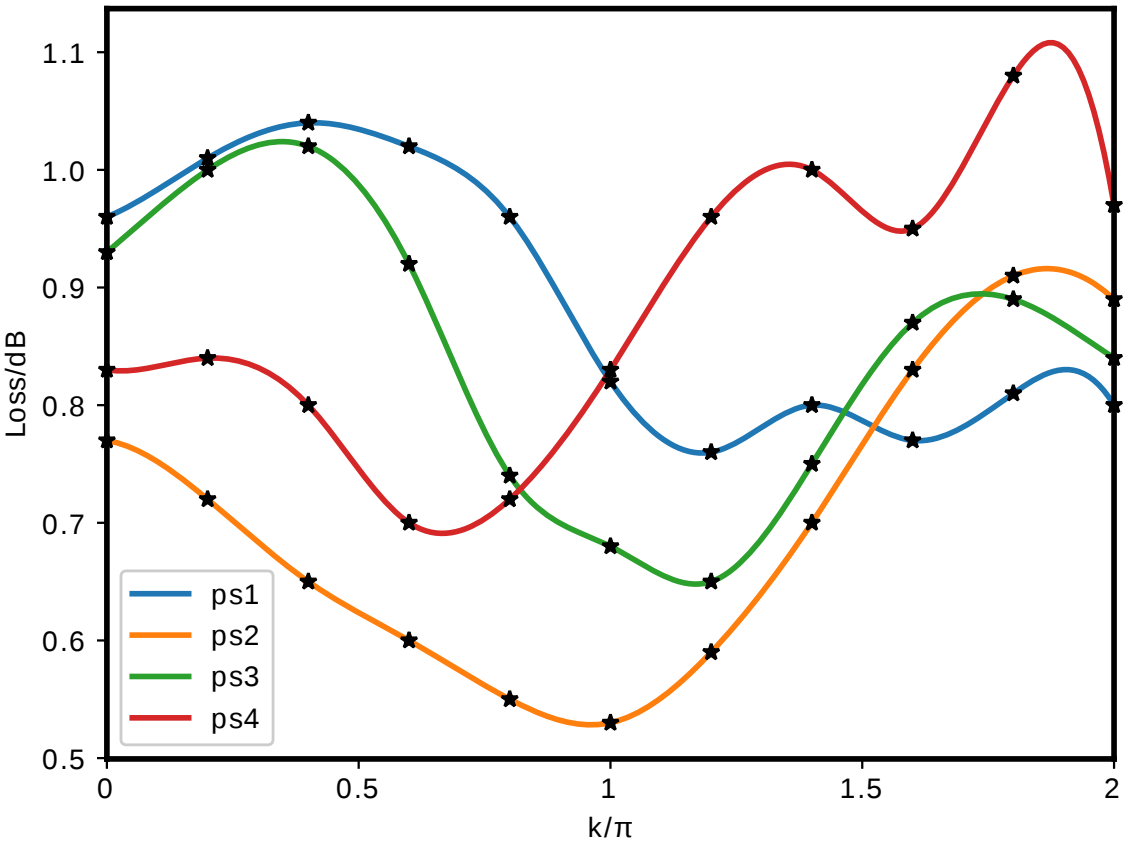

FIGURE 2.10: Losses of phase shifter at different value of k, the data is generated using interpolation method based on the data presented in Table. 2.3.

network system, the behavior can be calculated using the transfer matrix method. This section will present this method in detail.

2.4.1 Definition of the transfer matrix

Fig. 2.13 is a single cell schematic of our 1D two-port network system, and our goal is to calculate the S matrix relation between $[d, b]$ in the left and $[d', b']$ in the right. This S matrix is defined as

$$S(\phi, k) \begin{bmatrix} d \\ b' \end{bmatrix} = \begin{bmatrix} b \\ d' \end{bmatrix}. \tag{2.10}$$

The procedure to compute the $S(\phi, k)$ matrix can be divided into following five steps:

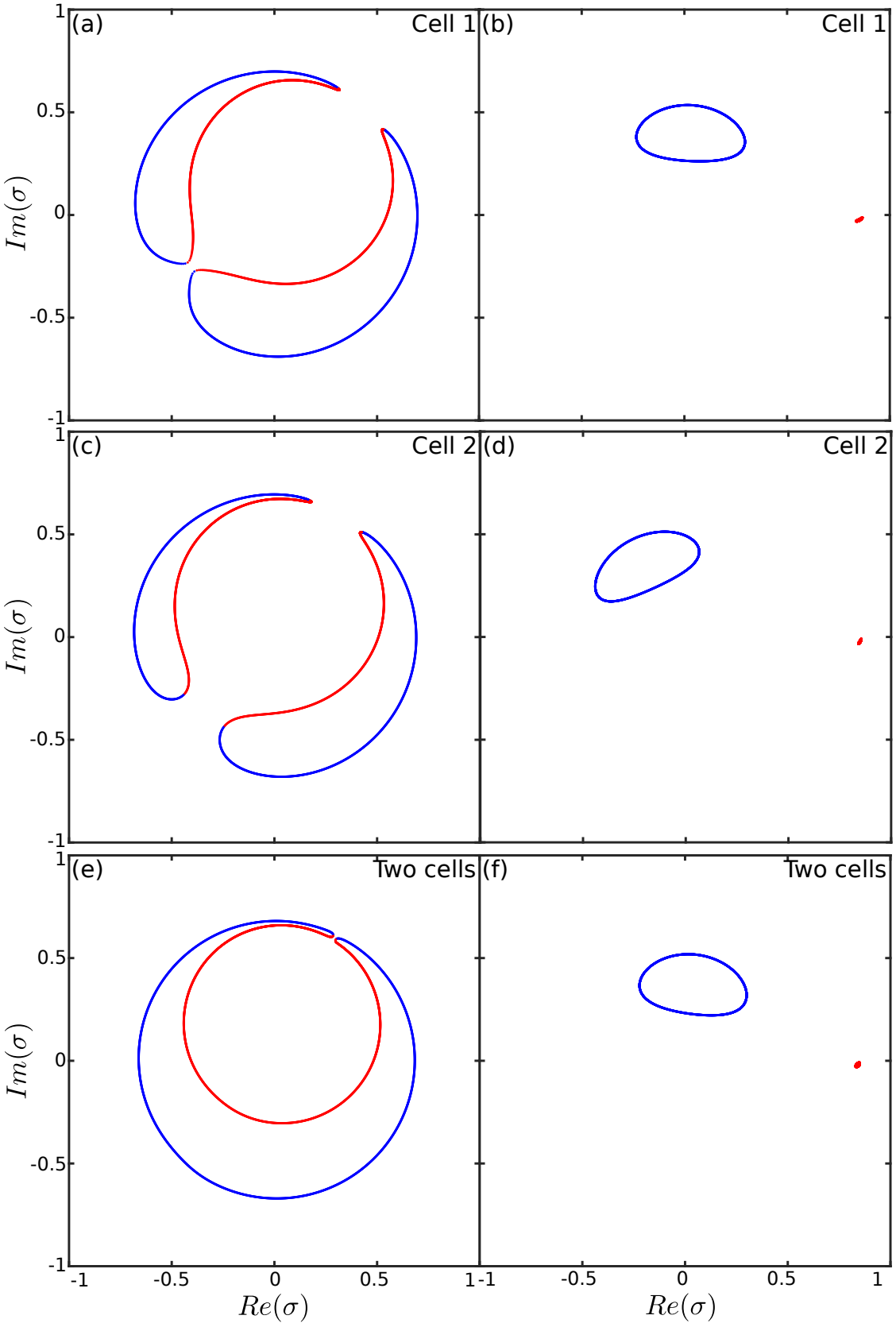

FIGURE 2.11: Simulation results of eigenvalues' moving trajectory for our system. For strong coupling system (a, c, e), winding behavior can be observed. For weak coupling system (b, d, f), there is no winding behavior. Eigenvalues located inside the unit circle due to the existence of losses in our system.

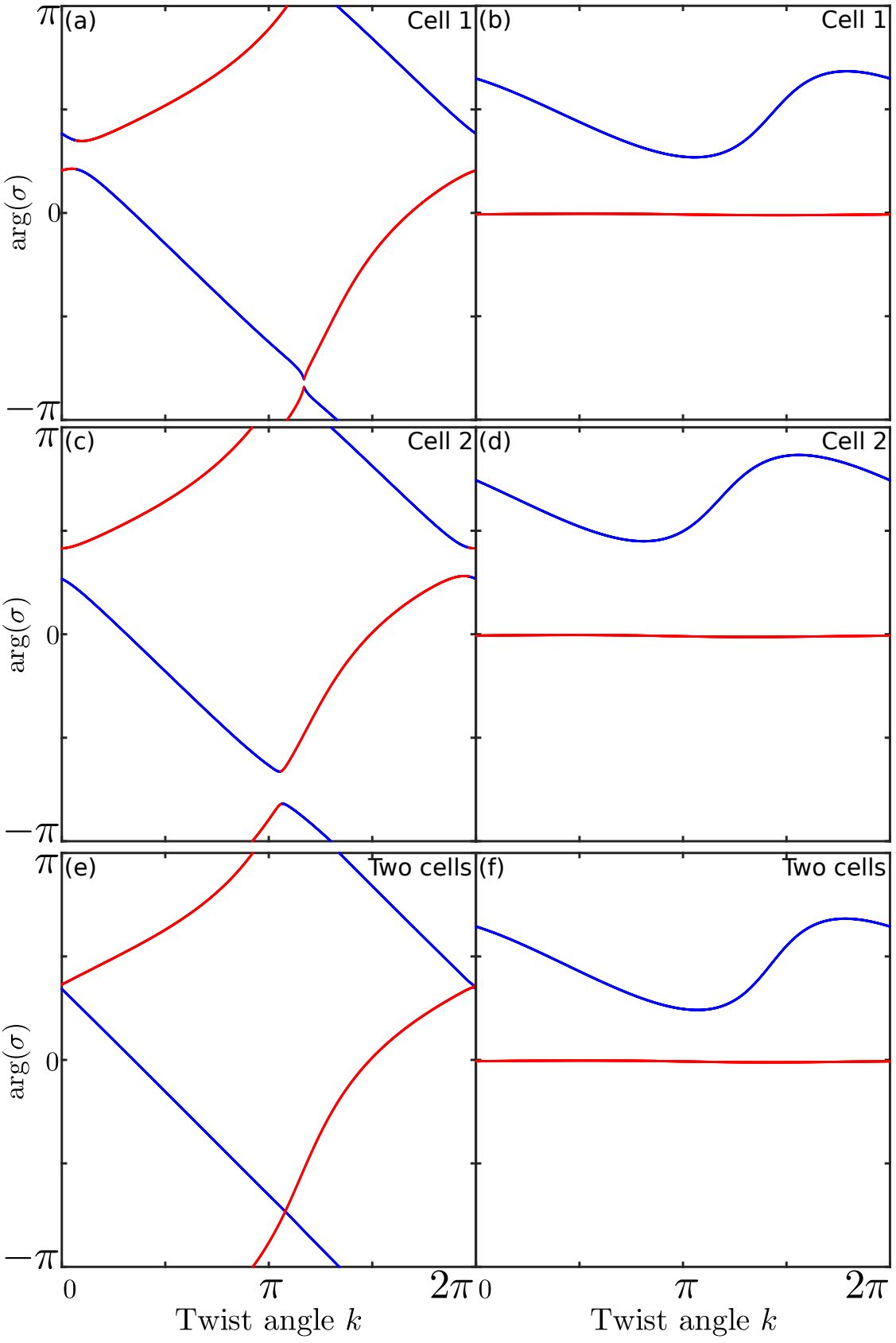

FIGURE 2.12: Phase information of the system. Non-zero winding is observed for strong coupling system and the winding number for weak coupling system is zero. Losses are responsible for the gaps.

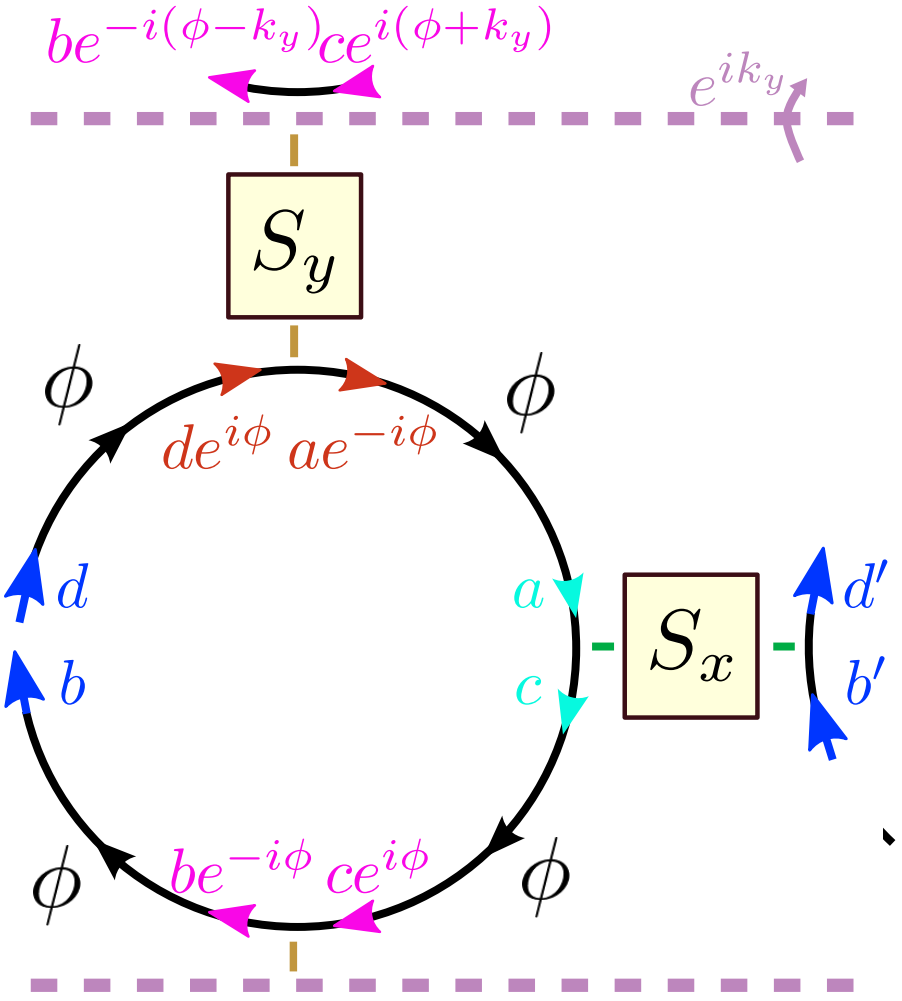

FIGURE 2.13: One cell of the network in our pumping experiment.

Step 1: From $[d, b]$ *to* $[de^{i\phi}, be^{-i\phi}]$. Two quarter rings connect these four points, therefore, we have

$$\begin{bmatrix} de^{i\phi} \\ be^{-i\phi} \end{bmatrix} = \underbrace{\begin{bmatrix} e^{i\phi} & 0 \\ 0 & e^{-i\phi} \end{bmatrix}}_{T_1} \begin{bmatrix} d \\ b \end{bmatrix}. \tag{2.11}$$

Step 2: From $[de^{i\phi}, be^{-i\phi}]$ *to* $[ae^{-i\phi}, ce^{i\phi}]$. Bloch theory is used in this step to connect four points in upper cell and low cell. For the coupler in y direction, we have

$$\begin{bmatrix} be^{-i(\phi-k_y)} \\ ae^{-i\phi} \end{bmatrix} = S_y \begin{bmatrix} de^{i\phi} \\ ce^{i(\phi+k_y)} \end{bmatrix}.$$

Combining these relations gives

$$be^{-i(\phi-k_y)} = be^{-i\phi} \cdot e^{ik_y}, ce^{i(\phi+k_y)} = ce^{i\phi} \cdot e^{ik_y}.$$

Hence,

$$\begin{bmatrix} ae^{-i\phi} \\ ce^{i\phi} \end{bmatrix} = \underbrace{\begin{bmatrix} \frac{-\det(S_y)}{S_y^{12}} & \frac{S_y^{22}e^{iky}}{S_y^{12}} \\ \frac{-S_y^{11}e^{-iky}}{S_y^{12}} & \frac{1}{S_y^{12}} \end{bmatrix}}_{T_2} \begin{bmatrix} de^{i\phi} \\ be^{-i\phi} \end{bmatrix}. \tag{2.12}$$

Step 3: From $[ae^{-i\phi}, ce^{i\phi}]$ *to* $[a, c]$. This step is the same as *step 1*; we have

$$\begin{bmatrix} a \\ c \end{bmatrix} = \underbrace{\begin{bmatrix} e^{i\phi} & 0 \\ 0 & e^{-i\phi} \end{bmatrix}}_{T_3} \begin{bmatrix} ae^{-i\phi} \\ ce^{i\phi} \end{bmatrix}. \tag{2.13}$$

Step 4: From $[a, c]$ *to* $[d', b']$. From the x direction coupler we have

$$\begin{bmatrix} d' \\ c \end{bmatrix} = S_x \begin{bmatrix} a \\ b' \end{bmatrix},$$

and therefore,

$$\begin{bmatrix} d' \\ b' \end{bmatrix} = \underbrace{\begin{bmatrix} \frac{\det(S_x)}{S_x^{22}} & \frac{S_x^{12}}{S_x^{22}} \\ -\frac{S_x^{21}}{S_x^{22}} & \frac{1}{S_x^{22}} \end{bmatrix}}_{T_4} \begin{bmatrix} a \\ c \end{bmatrix}. \tag{2.14}$$

Step 5: From transfer matrix to scattering matrix. Combining Eq. 2.11 — 2.14, we have the transfer matrix for one cell,

$$T(\phi, k) \begin{bmatrix} d \\ b \end{bmatrix} = \begin{bmatrix} d' \\ b' \end{bmatrix},$$

where

$$T(\phi, k) \equiv \begin{bmatrix} \frac{-\det(S_x)\det(S_y)e^{2i\phi} - S_x^{12}S_y^{11}e^{-ik}}{S_x^{22}S_y^{12}} & \frac{\det(S_x)S_y^{22}e^{ik} + S_x^{12}e^{-2i\phi}}{S_x^{22}S_y^{12}} \\ \frac{S_x^{21}\det(S_y)e^{2i\phi} - S_y^{11}e^{-ik}}{S_x^{22}S_y^{12}} & \frac{-S_x^{21}S_y^{22}e^{ik} + e^{-2i\phi}}{S_x^{22}S_y^{12}} \end{bmatrix}. \tag{2.15}$$

Several different quantities can be computed from Eq. 2.15. Firstly, if the stack is infinite in extent, we can look for Bloch solutions satisfying

$$d' = e^{ik_x}d, \quad b' = e^{ik_x}b. \tag{2.16}$$

Hence, the eigenvalues of $T(\phi, k)$ are values for e^{ik_x}, where k_x is the quasimomentum in the x direction, for given values of quasi-energy ϕ and y-quasimomentum k. This is essentially the calculation for the bulk quasi-energy bandstructure. The solution can be obtained analytically, by using the convenient parameterization

$$S_\mu = \begin{bmatrix} \sin(\theta_\mu)e^{i\chi_\mu} & -\cos(\theta_\mu)e^{i(\varphi_\mu-\epsilon_\mu)} \\ \cos(\theta_\mu)e^{i\epsilon_\mu} & \sin(\theta_\mu)e^{i(\varphi_\mu-\chi_\mu)} \end{bmatrix}, \quad \mu = x, y. \tag{2.17}$$

The angle θ_μ describes the "coupling strength", with $\theta = 0$ corresponding to zero coupling between adjacent cells. After tedious calculation, it can be found out that the quasi-energy bandstructure is gapless when $\theta_x + \theta_y = \pi/2$. This defines two distinct insulator phases: a weak-coupling insulator ($\theta_x + \theta_y < \pi/2$) and a strong-coupling insulator ($\theta_x + \theta_y > \pi/2$). These will turn out to be topologically distinct.

Next, we stack n cells to form a one-dimensional lattice. Let d_L, b_L, d_R, b_R be the input/output amplitudes on the left and right edges of the stack. Then

$$T_n(\phi, k) \begin{bmatrix} d_L \\ b_L \end{bmatrix} = \begin{bmatrix} d_R \\ b_R \end{bmatrix}, \quad where\ T_n \equiv [T(\phi, k)]^n. \tag{2.18}$$

This can be re-arranged into a scattering matrix equation,

$$S_n(\phi, k) \begin{bmatrix} d_L \\ b_R \end{bmatrix} = \begin{bmatrix} b_L \\ d_R \end{bmatrix}, \quad where\ S_n \equiv \frac{1}{T_n^{22}} \begin{bmatrix} -T_n^{21} & 1 \\ \det(T_n) & T_n^{12} \end{bmatrix}. \tag{2.19}$$

Without losses, $S_n(\phi, k)$ is unitary and its two eigenvalues are unimodular. The diagonal entries of S_n are the left and right reflection coefficients, and the off-diagonal entries are the transmission coefficients.

Losses can be incorporated into the model by multiplying each entry of the coupling matrices, S_x and S_y, by damping factors. This makes the coupling matrices sub-unitary:

$$S_\mu = \begin{bmatrix} \sin(\theta_\mu)\, e^{i\chi_\mu} e^{-\gamma_\mu^{11}} & -\cos(\theta_\mu)\, e^{i(\varphi_\mu-\xi_\mu)} e^{-\gamma_\mu^{12}} \\ \cos(\theta_\mu)\, e^{i\xi_\mu} e^{-\gamma_\mu^{21}} & \sin(\theta_\mu)\, e^{i(\varphi_\mu-\chi_\mu)} e^{-\gamma_\mu^{22}} \end{bmatrix}, \quad \mu = x, y. \tag{2.20}$$

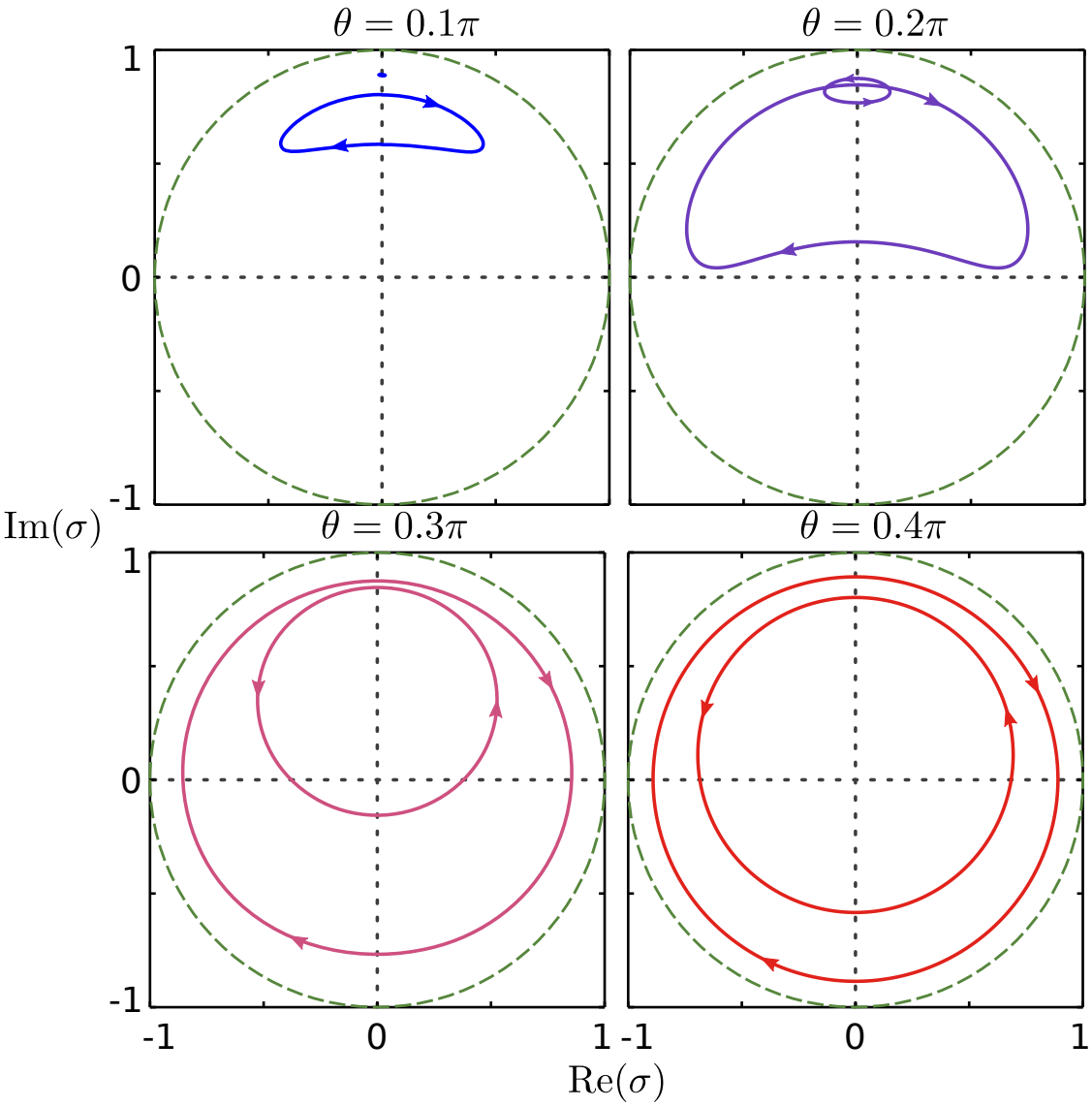

FIGURE 2.14: Trajectories of the S_n matrix eigenvalues in the complex plane, as k advances from 0 to 2π. The network parameters are the same as in Fig. 2.15, except that loss is present: each coupling matrix S_x and S_y is multiplied by a uniform loss factor of $e^{-\gamma} = 0.9$.

In principle, each of the $\exp(-\gamma_\mu^{ij})$ factors can be independent. Losses occurring within the cables (links) or phase shifters can be incorporated into these coupling matrix damping factors, without loss of generality.

When losses are present, the S_n matrix defined in Eq. (2.19) becomes sub-unitary, i.e. its eigenvalues lie inside the unit circle. Hence, in the large-n limit the reflection coefficients have magnitudes smaller than unity, reflecting the fact that the input waves undergo dissipation within the network.

Fig. 2.14 shows the trajectories of the eigenvalues of S_n in the complex plane, as k is wound through 2π, for a lossy network. Here, we have taken a uniform factor $\exp(-\gamma_\mu^{ij}) = 0.9$ in all couplers. It can be seen that the behavior is similar to our experimental results. In particular, deep in the topologically trivial or non-trivial phase ($\theta = 0.1\pi$ and $\theta = 0.4\pi$ respectively), the eigenvalue trajectories are clearly continuable to the zero-winding and nonzero-winding behavior of the lossless system.

2.4.2 Winding numbers

For the scattering matrix S_n calculated in the previous section, we are interested in the variation of its eigenvalues, especially its winding numbers. If ϕ is chosen to be in the bulk bandgap, then for large n (i.e., a long cylinder), the transmission coefficients go to zero and S_n reduces to a diagonal matrix. Then the two eigenvalues are simply the two reflection coefficients, and are predicted to have winding number 0 in the weak-coupling insulator phase, and winding numbers ± 1 in the strong-coupling insulator phase. The numerical results agree, as shown in Fig. 2.15. This winding behavior can be deduced from the principle that bound states induce π phase shifts in the reflection coefficient [108], or by considering how edge state branches are transported across the bandgap in the projected quasi-energy band-structure [51].

It is instructive to see how this works in the limits of very weak or very strong coupling. Firstly, for $\theta_x = \theta_y = 0$, the reflection coefficients are k-independent:

$$\frac{b_L}{d_L} = -e^{i(4\phi+\xi_x+\varphi_y)}, \quad \frac{d_R}{b_R} = -e^{i(\varphi_x-\xi_x)}. \tag{2.21}$$

And for $\theta_x = \theta_y = \pi/2$,

$$\frac{b_L}{d_L} = e^{i(2\phi+\chi_y)}\, e^{-ik}, \quad \frac{d_R}{b_R} = e^{i(2\phi+\varphi_x+\varphi_y-\chi_y)}\, e^{ik}, \tag{2.22}$$

which results in winding numbers of ± 1. For these two limiting cases, the bulk bands are completely flat. For intermediate values of θ, however, it is necessary to choose a value of ϕ that lies in the bulk bandgap, for the topological pumping procedure to make sense.

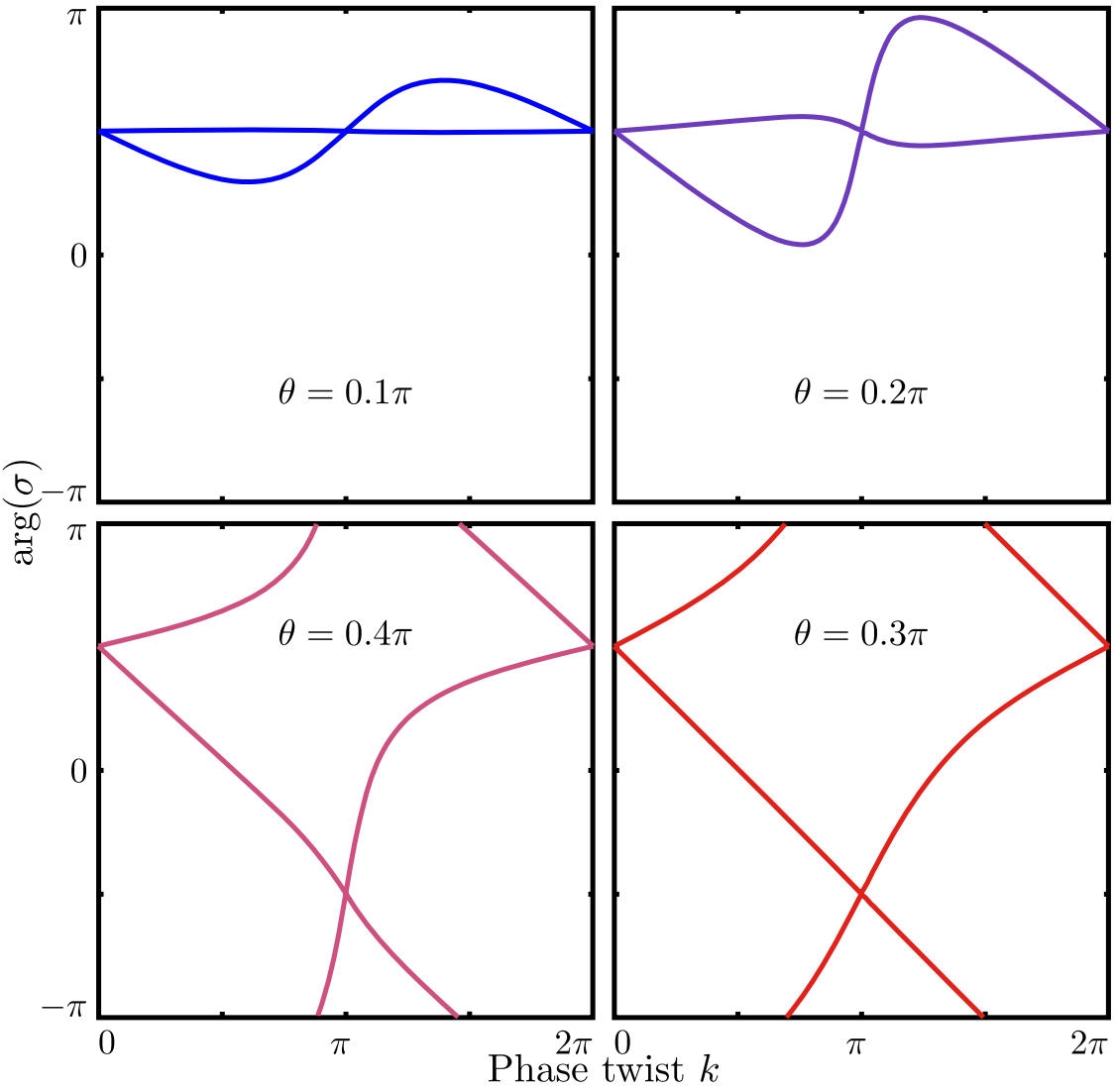

FIGURE 2.15: Complex argument of the S_n matrix eigenvalues, σ, for lossless networks with $n = 10$ cells. Four different values of the coupling strength θ are shown. The S_x and S_y coupling matrices are taken to be equal and lossless with $\varphi = \chi = 0$ and $\xi = \pi/2$. The quasi-energy is $\phi = 0.25\pi$ (mid-gap). The system is topologically trivial for $\theta < \pi/4$, and non-trivial for $\theta > \pi/4$.

Fig. 2.16 plots the arguments of the S matrix eigenvalues versus k, calculated using the transfer matrix method, for several values of n. (As shown in Fig.2.18, the numerical model is in good agreement with the experimental results for $n = 1$ and $n = 2$.) There is no winding for $n = 1$; nonzero winding sets in for $n = 2$, and the winding remains nonzero for larger values of n, such as $n = 50$ or $n = 100$. It may seem surprising that the winding behavior for system size as small as $n = 2$ is essentially equivalent to the behavior in the large-n limit. This is due to the fact that the edges states in this system are tightly localized to the edges, as discussed

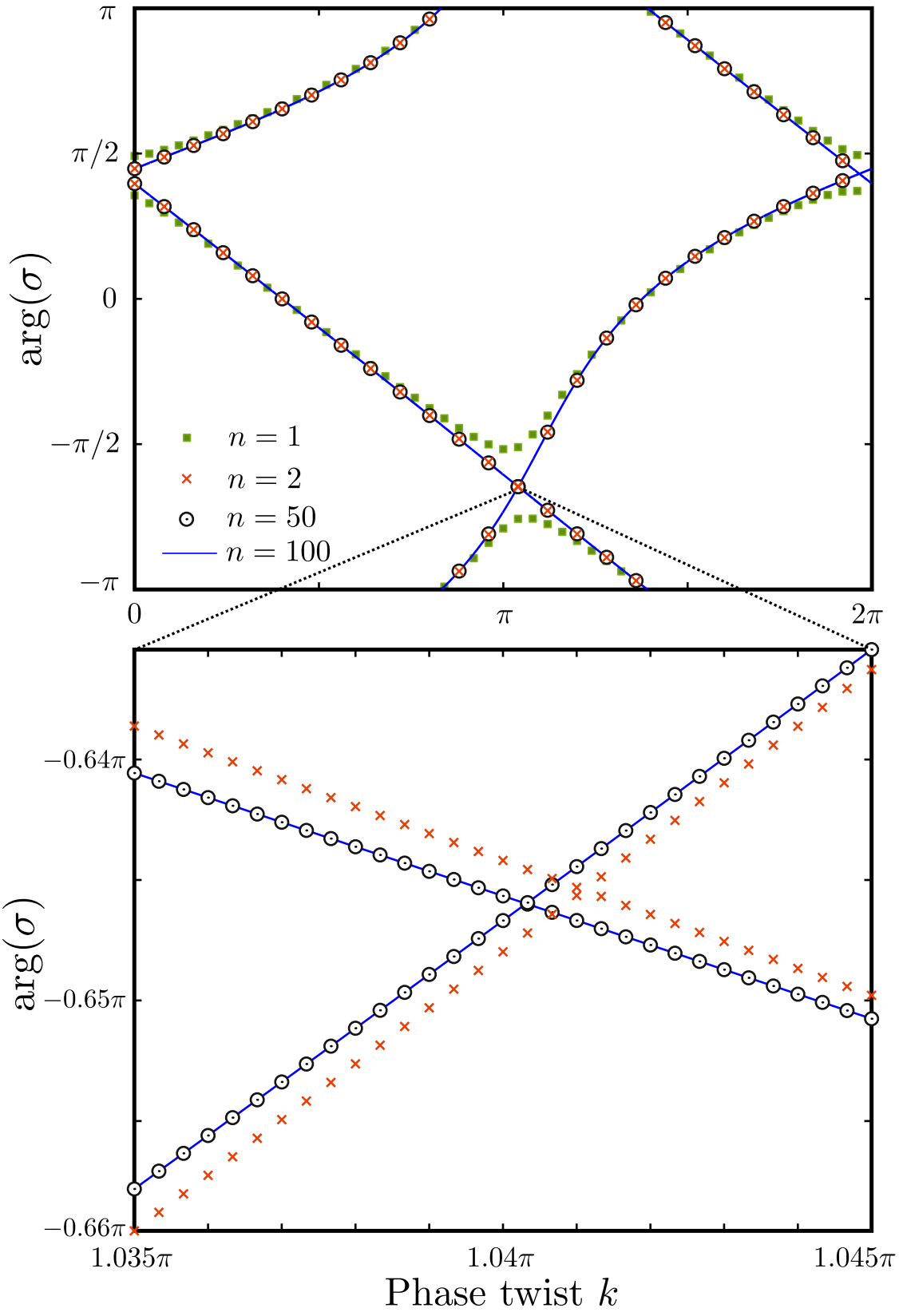

FIGURE 2.16: Complex argument of the S_n matrix eigenvalues versus twist angle k, calculated numerically for different values of the system size n. For $n \geq 2$, nonzero winding is observed. For comparison, see the experimental results shown in Fig. 2.18. The coupling strength here is $\theta = 0.4\pi$, similar to the topologically nontrivial regime of the network in the actual experiment.

in the next section. When the network is in the topologically trivial regime, no winding is observed in any case.

2.5 Simulation and experiment

Based on the theory introduced in Section 2.4 and experiment procedure described in Section 2.3, we finish both the simulation and experiment. In this part, I will present results for both simulation and experiment and analyze them.

2.5.1 Simulation and experiment results

From Section 2.4.2, we know that for a strong coupling network, winding behavior can be observed for a system with at least two cells, while for a weak coupling network, no winding behavior will occur. Fig. 2.17 is the result for both simulation and experiment using the components described in Section 2.3.4. In this figure, solid curves are eigenvalue trajectories from simulation while circles are experimentally measured data. The arrows on the curves indicate the motion direction of trajectories with k increasing from 0 to 2π. The eigenvalue do not lie on the green dashed unit circle because of losses in the network that make the S matrix subunitary. For the one-cell strong coupling system, the two S matrix eigenvalues, $\sigma_{\pm}$, move along distinct closed trajectories as k is increased through 2π, as shown in Fig. 2.17(a). Each individual trajectory does not encircle the origin (i.e., the winding number is zero), even though the network band structure is in the topologically nontrivial regime. This is because topological protection requires the opposite edges in a finite system to be well separated, so as to have negligible overlap between the counterpropagating edge states on each edge. When the separation is increased by connecting two cells in series, the trajectories coalesce into a pair of loops with winding numbers ± 1, as shown in Fig. 2.17(b). By contrast, consider the situation for a weak coupling network, for both the one-cell system shown in Fig. 2.17(c) and the two-cell system shown in Fig. 2.17(d); the eigenvalues move along separate trajectories without encircling the origin, which means the winding number is zero.

The winding numbers can also be visualized by plotting $\arg[\sigma_{\pm}]$ against k, as in Fig. 2.18. It is also worth noting that, in the topologically nontrivial regime,

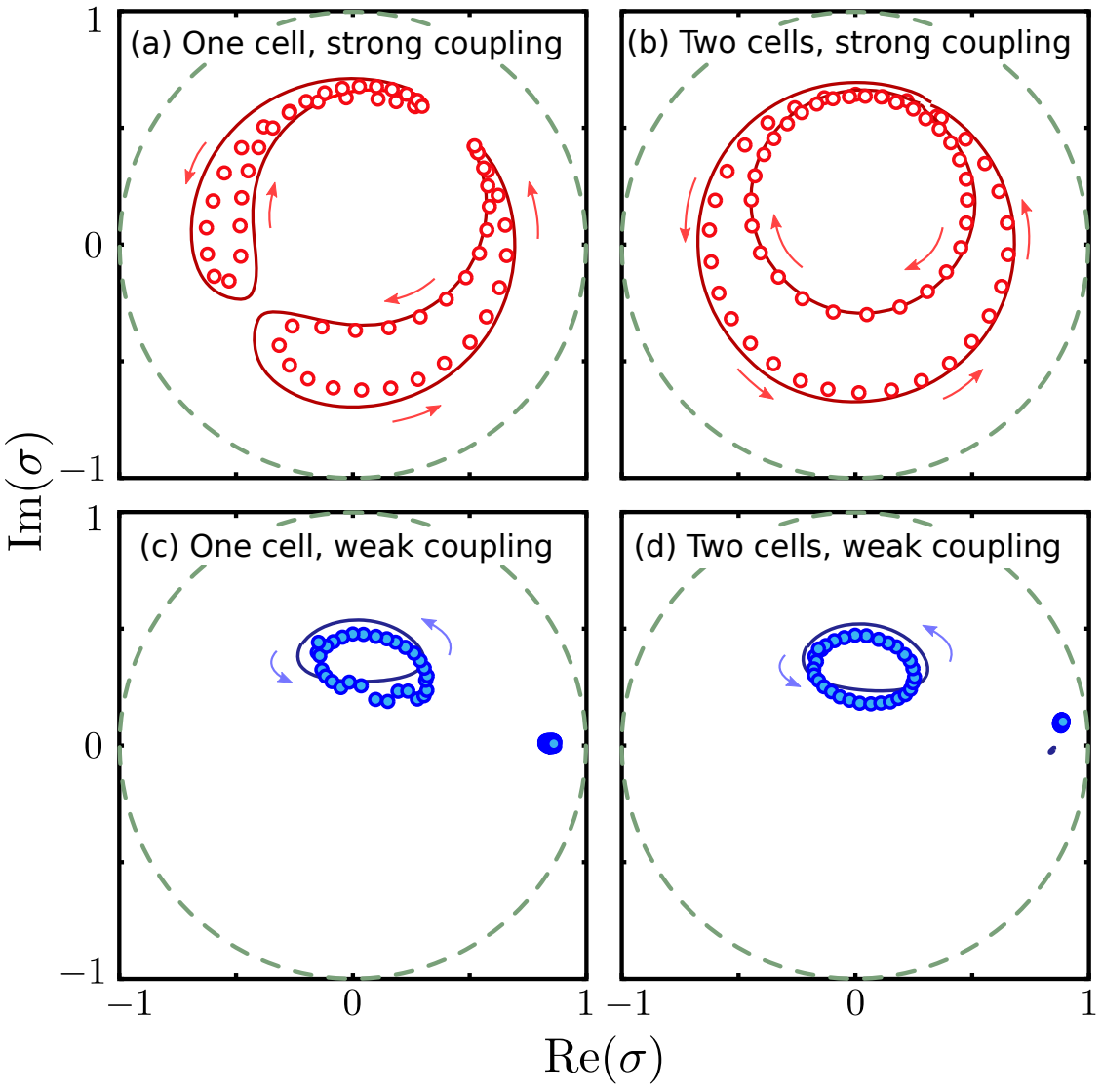

FIGURE 2.17: Scattering matrix eigenvalues measured across one cell(left) and across two cells in series (right). Arrows indicate the direction of motion with increasing k. Circles show experimental data and solid curves show theoretical calculations using the scattering parameters measured for each network component individually (including losses). Nonzero winding numbers can be observed in the strong-coupling two-cell case. The unit circle is indicated by dashed curves.

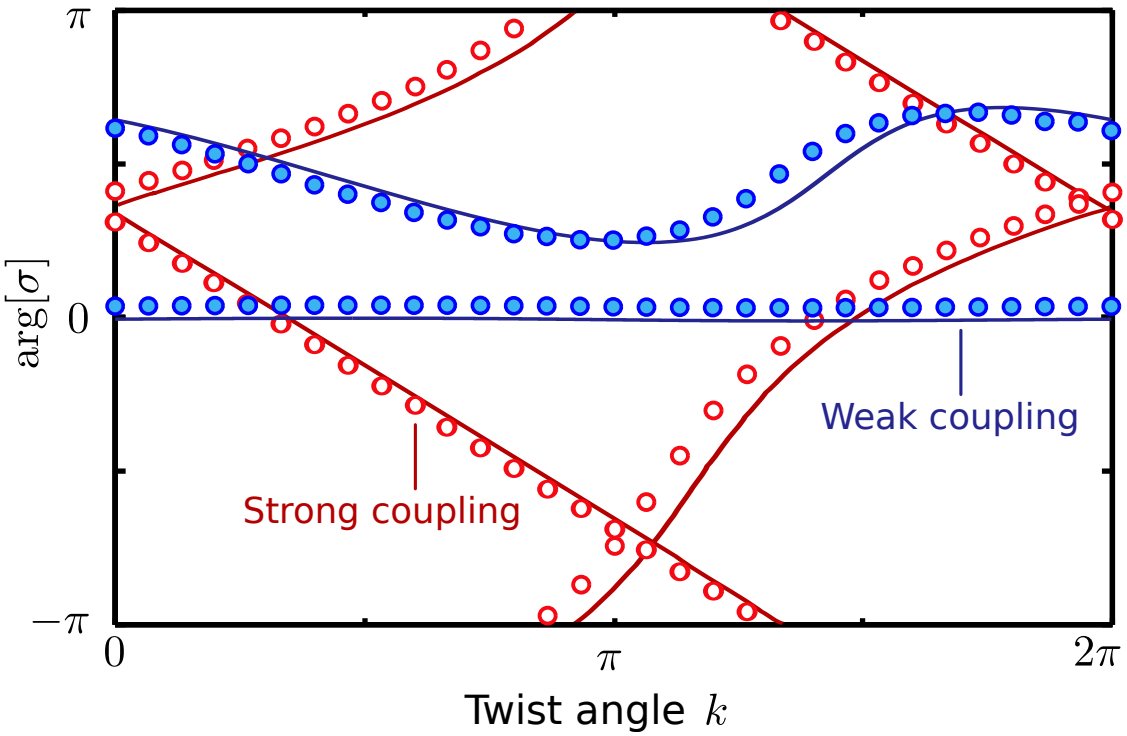

FIGURE 2.18: Arguments of the complex S matrix eigenvalues for the two-cell network, as the phase shift k is tuned through 2π. Empty circles show the strong coupling measurement data, filled circles show the weak coupling data, and solid curves show theoretical calculations. For strong coupling, the two eigenvalues have winding numbers ± 1, corresponding to the bulk band structure being topologically nontrivial.

the two S matrix eigenvalues wind in opposite directions. This corresponds to the fact that the topological edge states on opposite edges have opposite group velocities. In terms of the projected band structure, one branch of the edge state has a dispersion curve that crosses the probed value of ϕ from above and the other from below; hence, the induced scattering phase shifts have opposite signs.

2.5.2 Improved results using a new experiment setup

The results shown in Section. 2.5.1 were achieved based on a system with relatively high loss. As a result, the eigenvalue trajectories located inside the unit circle (ie. the absolute value of eigenvalues) are far less than 1. To improve the result, we implemented an updated version of the network, using amplifiers to compensate the losses in the system, and with operation frequency of 900 MHz (which is much lower than 5 GHz; the lower the frequency, the lower the loss in the microwave regime). Moreover, the new components have much higher precision. All these

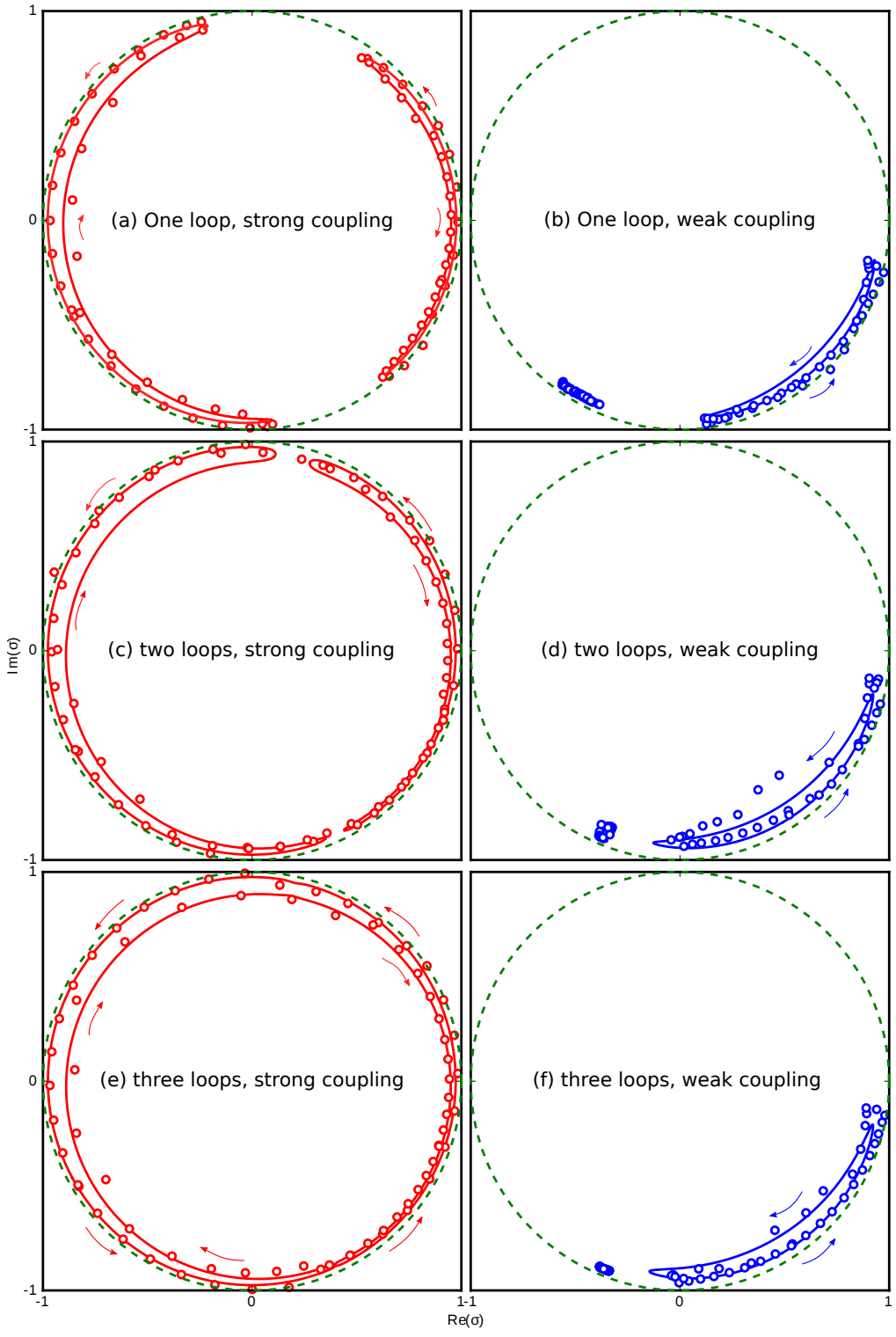

FIGURE 2.19: Improved results for scattering matrix eigenvalues measured for one cell, two cells and three cells system, both strong coupling system (left) and weak coupling system (right). Arrows indicate the direction of motion with increasing k. Circles show experimental data and solid curves show theoretical calculations using the scattering parameters measured for each network component individually. Nonzero winding numbers can be observed in the strong-coupling three-cell case. The unit circle is indicated by dashed curves.

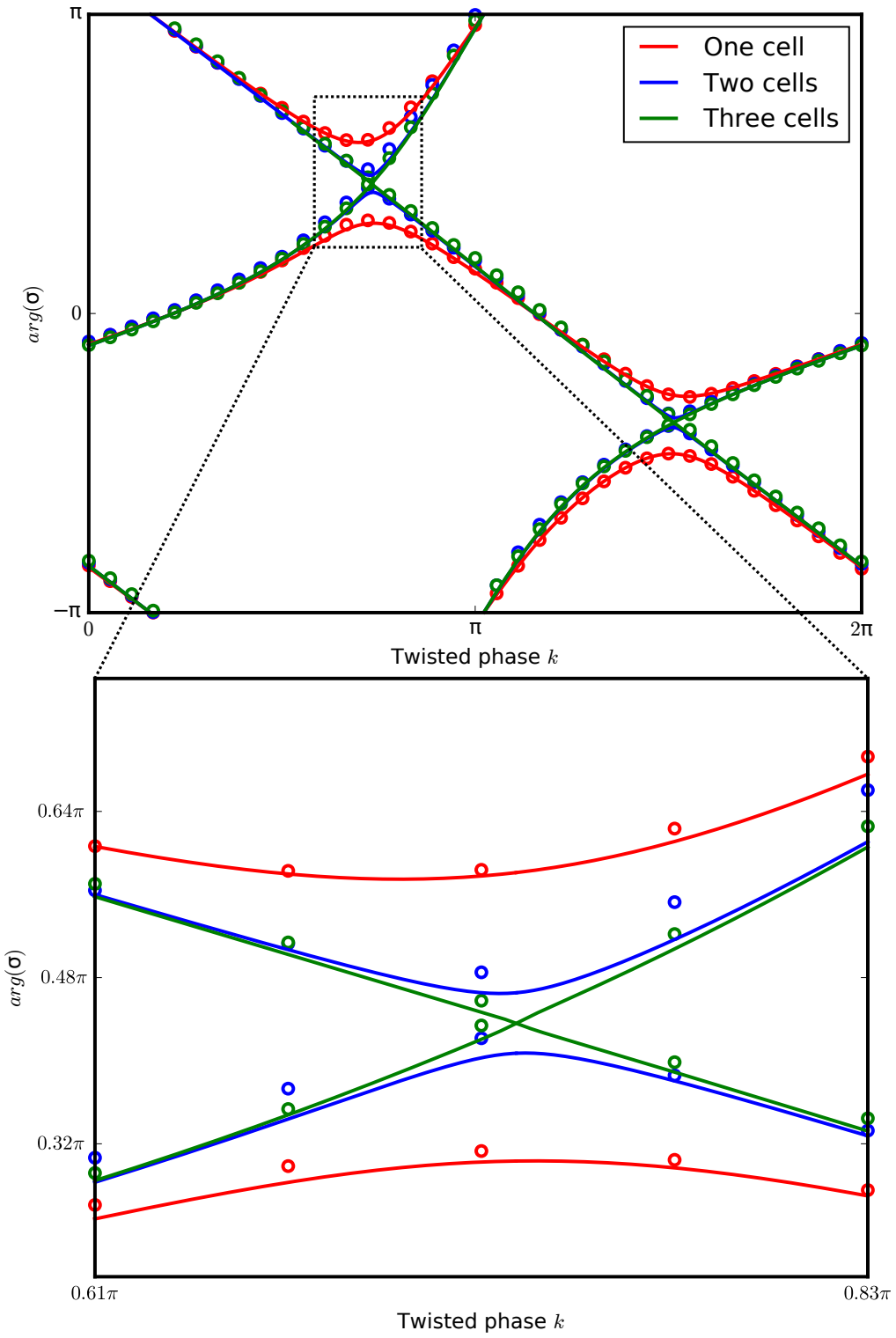

FIGURE 2.20: Improved result for arguments of the complex S matrix eigenvalues for strong coupling system, as the phase shift k is tuned through 2π. Empty circles show the measurement data, and solid curves show theoretical calculations. As the system scale increase from one cell to three cells, the gap between two curves decrease quickly which correspond to the smaller gaps in eigenvalue trajectories. To make it clear, enlarged picture is shown in lower figure.

aspects contribute to much better results, as shown in Fig. 2.19 and Fig. 2.20. A detailed description of the implementation of the new experiment setup will be given in the next chapter.

Fig. 2.19 presents the improved results for the scattering matrix eigenvalues. The dashed line shows the unit circle, solid curves are theoretical eigenvalue trajectories, empty circles are experimentally measured data, and the motion direction of eigenvalue trajectories as increasing k is indicated by arrows. Here, results are shown for one-cell, two-cell and three-cell systems, both in the strong coupling regime and the weak coupling regime. For all the results, the curves are very close to the unit circle, which means the losses are very small. For the one-cell strong coupling network as shown in Fig. 2.19(a), two eigenvalues form two separated closed trajectories due to the small system scale, which suppresses topological protection even though the network parameters are in the topologically nontrivial regime. For the two-cell system shown in Fig. 2.19(c), the situation is similar to the one-cell system except that the gaps between the two closed trajectories are much smaller because of the larger system scale. For the three-cell system shown in Fig. 2.19(e), two trajectories have merged into two loops encircling the origin with winding number ± 1, which demonstrates the emergence of a topologically nontrivial phase. By contrast, in the weak coupling regime of Fig. 2.19(b), 2.19(d) and 2.19(f), the eigenvalues move along separate trajectories without encircling the origin.

Similar information can also be obtained by plotting $\arg[\sigma_{\pm}]$ against k, as in Fig. 2.20. In this figure, the phase information is presented for the strong coupling network, with one cell, two cells, and three cells. It is clear that there are gaps for both the one-cell and two-cell systems, while for the three-cell system, the gap is negligible even in the enlarged figures shown in the lower figure of Fig. 2.20. All these details provide a solid proof of nonzero winding for the three cells strong coupling network.

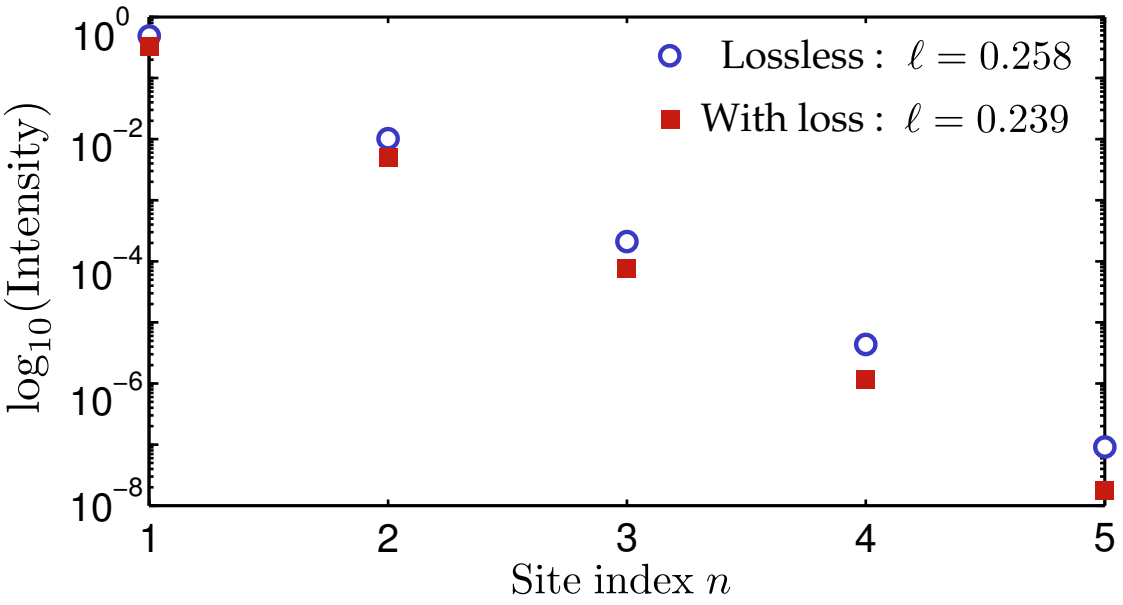

FIGURE 2.21: Semilog plot of the edge state intensity versus ring index n, for lossless (blue circles) and lossy (red squares) networks respectively. The network consists of an infinite strip 5 unit cells wide, with line delay $\phi = 0.2\pi$ and coupler strength $\theta = 0.4\pi$ (which matches the "strong coupling" regime of the experiment). For the lossy system, we add loss $e^{-\gamma}$ to each quarter-ring segment, where $\gamma = 0.25$. For both cases, the edge state at $k = -0.4\pi$ is shown. The intensity at each unit cell is defined as the sum of the absolute squares of the wave amplitudes on the four quarter-ring segments (cf. Fig. 2.13).

2.6 Discussion

2.6.1 Insulation and edge state localization

Strictly speaking, topologically nontrivial behavior emerges in a sample only in the limit where opposite edges are spatially well-separated. In terms of the topological edge states, the wavefunctions for edge states on opposite edges must have negligible overlap.

In order to determine the penetration depth of the edge states, we consider a hypothetical strip with an ample width of 5 unit cells in the $\hat{x}$ direction (and infinite in the $\hat{y}$ direction). Fig. 2.21 shows the semilog plot of the intensity (defined as the absolute square of the wave amplitudes in the links) versus distance along the $\hat{x}$ direction (measured in lattice units), for a typical mid-gap edge state. Two distinct cases are considered: with loss levels similar to those in the experiment, and without loss. All other network parameters, including the coupling constant

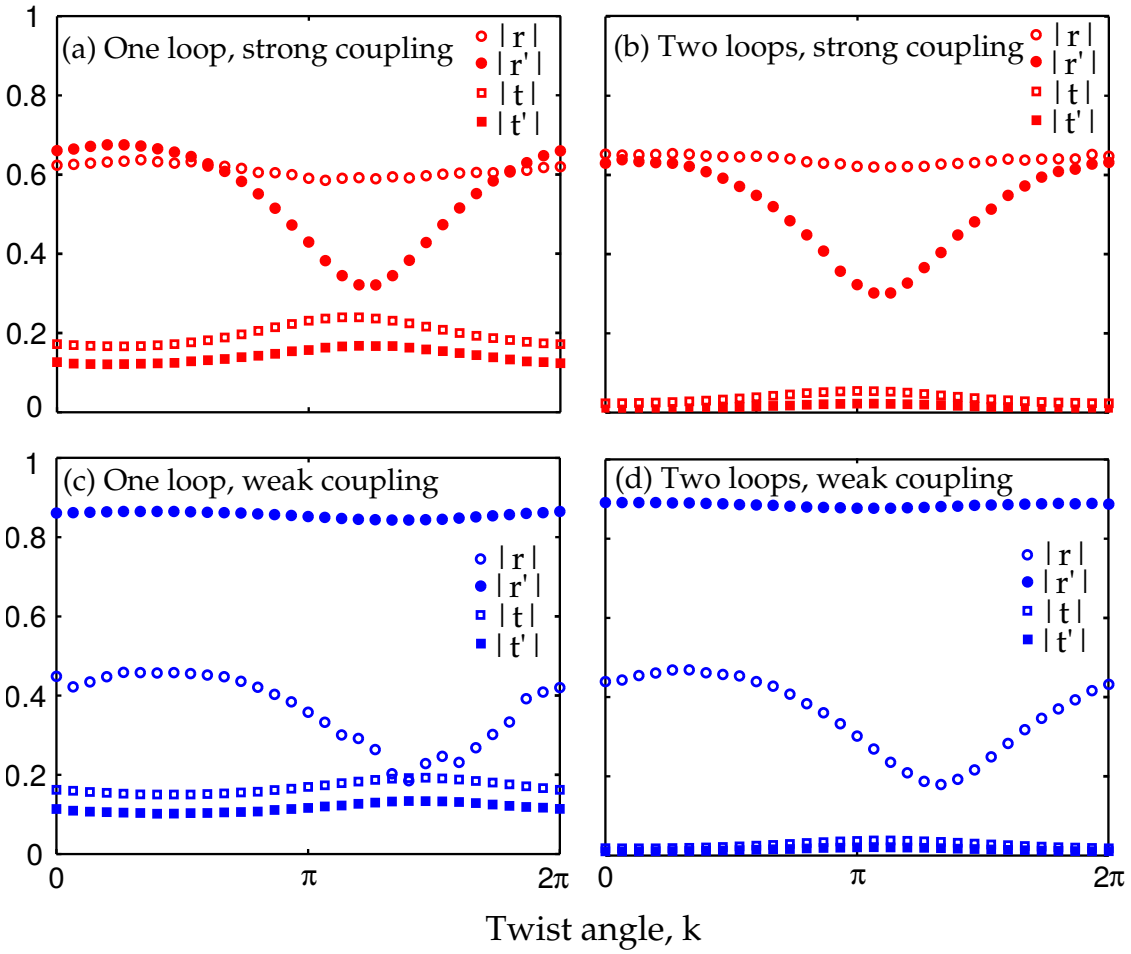

FIGURE 2.22: Experimentally-measured reflection coefficient magnitudes ($|r|$ and $|r'|$, circle symbols) and transmission coefficient magnitudes ($|t|$ and $|t'|$, square symbols), versus phase shift k. Results are shown for the strong and weak coupling regimes, and for the one-loop and two-loop configurations. Unprimed and primed coefficients refer to waves incident on the left and right edges, respectively. In the two-loop configurations, the transmission becomes negligible.

θ, are chosen to be similar to the topologically nontrivial regime of the actual experiment.

From this plot, we see that the edge states in both the lossless and lossy networks are exponentially localized to one edge: the intensity scales as $I_n \propto \exp(-n/\ell)$, where n is the site index in the $\hat{x}$ direction. A numerical fit gives a penetration depth of $\ell \approx 0.258$ unit cells for the lossless network. Introducing losses decreases this only slightly, to $\ell \approx 0.239$ unit cells. Hence, we can conclude that the edge states have negligible overlap even for a network two unit cells wide, as in the experiment. Furthermore, the penetration depth is mainly determined by the bandgap, not by the losses in the network.

We can also verify that the edges are spatially well-separated by using direct experimental data. In the scattering formulation of the topological pump (described in Section 1.2.2), the edges are well-separated if waves incident on one edge of the cylindrical sample have negligible transmission to the opposite edge [108]. Fig. 2.22 shows reflection and transmission coefficients measured by the network analyzer in the experiment. For both strong and weak couplings, the transmission decreases significantly when going from the single-loop configuration (corresponding to a one cell wide cylinder) to the two-loop configuration (corresponding to a two cell wide cylinder). For the latter, the magnitude of the transmission coefficient is less than 0.06 (for strong coupling) and less than 0.04 (for weak coupling). Thus, this line of reasoning likewise indicates that we are justified in interpreting the behavior of the two-loop network in terms of topological insulator physics.

2.6.2 Analysis of the results

Our experiment deviates from an ideal topological pump in several respects. Firstly, as previously mentioned, in the ideal topological pump the edges are separated by a large number of unit cells, so that there is a true "bulk", whereas in our experiment there are only two unit cells. However, this does not make a significant difference to the physical interpretation, as the relevant phenomenon—the emergence of a non-zero winding number—is observed already when going from the one-cell to the two-cell case, shown in Figs. 2.17(a) and (b). This arises from the fact that the system is deep in either the topologically trivial or nontrivial phases, based on our choices of the coupling strength θ; in the nontrivial case, each edge state is strongly confined to one unit cell, with negligible amplitude on the next unit cell. Indeed, calculations based on realistic parameters show no significant changes in the trajectory of the S matrix eigenvalues as the number of cells is increased to 100.

When the edges are well-separated, the S matrix reduces to a pair of reflection coefficients $r_\pm \equiv \beta_\pm/\alpha_\pm$, where $\{\alpha_\pm, \beta_\pm\}$ are the input/output wave amplitudes labeled in Fig. 2.7. This is observed in the small transmission coefficients in the two unit cell systems: $|t| < 0.06$ in the strong coupling system and $|t| < 0.04$ in the weak coupling case. Simulations reveal that the edge states have penetration depths on the order of a unit cell.

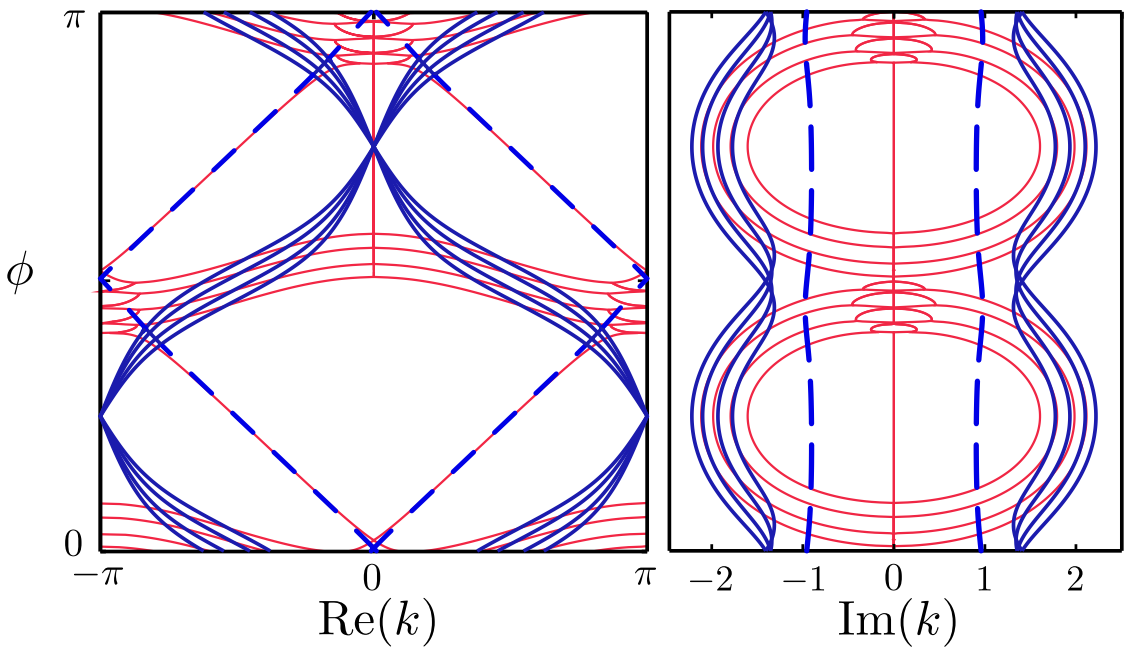

FIGURE 2.23: Complex projected bandstructure of a hypothetical lossy network (blue lines), consisting of an infinite strip 5 unit cells wide. Each link has real tunable phase delay ϕ, each coupler has loss $e^{-\gamma}$ in each output port where $\gamma = 0.25$, and each edge of the strip obeys lossy boundary conditions $r_\pm = \exp(-0.2\pi)$, chosen to be roughly the same as in the experiment. The coupling strength is $\theta = 0.4\pi$, approximately equal to the "strong coupling" (topologically nontrivial) configuration in the experiment. The bandstructure for the lossless network ($\gamma = 0$ and $|r_\pm| = 1$) is plotted for comparison (red lines). The lossy network exhibits edge states whose dispersion relations are almost identical to the lossless network's topological edge states, and have lower loss than all other states (blue dashes).

Another difference between our experiment and the ideal topological pump is the presence of loss in all the network components: the cables, phase shifters, and couplers. As a result, the eigenvalues of the S matrix are not strictly constrained to the unit circle, as seen in Fig. 2.17. Nonetheless, we argue that these eigenvalue trajectories can be meaningfully linked to the existence or non-existence of topological edge states, based on the close relationship between the edge scattering parameters measured in the experiment and the projected bandstructure of the network.

In the experiment, $r_\pm$ is determined based on two parameters ϕ and k, with all other parameters (such as the coupling matrices) fixed; varying k then gives results like those shown in Fig. 2.14 and Fig. 2.17. Alternatively, we could either (i) determine ϕ given $r_\pm$ and k (by finding the eigenvalues of the scattering matrix for one period of an infinite strip [51]), or (ii) determine k given $r_\pm$ and ϕ (by

finding the eigenvalues of the transfer matrix for one period of the strip). Both procedures yield the projected bandstructure, with $r_\pm$ interpreted not as reflection coefficients, but as *boundary conditions* which are applied along the edge of the strip, specifying the phase shifts on the edge links. In the absence of losses, if the scattering experiment yields a non-zero winding number for ϕ in a bulk bandgap, then it can be seen that the projected bandstructure exhibits topological edge states [51].

Now, consider a lossy network. The losses can be described, without loss of generality, by making the coupling matrices sub-unitary, as well as by setting $|r_\pm| < 1$ (lossy boundary conditions). The two procedures described in the preceding paragraph, (i) and (ii), lead to two distinct types of complex projected bandstructure; we focus on procedure (ii), which takes $r_\pm$ and a real ϕ and yields complex wavenumbers k, whose imaginary parts are the attenuation constants of the propagating modes. One such complex bandstructure is shown in Fig. 2.23, generated using representative lossy $r_\pm$ and coupling matrices (a 5-cell-wide strip is used for clarity). The bandstructure contains clearly-defined edge states whose dispersion curves have real parts nearly indistinguishable from the lossless network's topological edge states. Apart from these, there also exist propagating bulk states. Even in the range of ϕ corresponding to the lossless network's bulk bandgap, there are bulk states with $\mathrm{Re}[k] \neq 0$, which are continuable to purely evanescent ($\mathrm{Re}[k] = 0$) states of the lossless system. However, these bulk states have significantly larger attenuation $|\mathrm{Im}(k)|$ compared to the edge states, which can be attributed to the fact that they experience losses over a wider area. If we wind $\arg[r_\pm]$ through 2π, with fixed $|r_\pm| < 1$ (corresponding to a sub-unitary trajectory in the complex plane), the part of the complex projected bandstructure corresponding to the bulk states remains nearly unchanged, in both its real and imaginary parts. For the edge states, the real part of the dispersion curve winds with $\arg[r_\pm]$, whereas the imaginary part remains nearly unchanged. Hence, winding $\arg[r_\pm]$ has the effect of "pumping" a branch of lossy edge states across one quasi-energy period.

2.7 Summary

In summary, this chapter presents my work on measuring a topological edge invariant in a microwave network, in the form of winding numbers of the S matrix eigenvalues. In Section 2.1, we started from network models by introducing CROW structures, Hafezi's coupled resonator model, and our network model. In Section 2.2, the bandstructure of our network model was investigated and it was shown that our system exhibits a topological nontrivial phase when $\theta_x + \theta_y > \pi/2$. In Section 2.3, based on Laughlin's adiabatic pumping idea, we mapped this 2D network model into a 1D two-port microwave network. In Section 2.4, we described the implementation of the experiment, and discussed how we measure the S matrix of the system. In Section 2.5, the experiment and simulation results were presented. In Section 2.6, we discussed the insulation and edge state localization, and the robustness of our results.

Chapter 3

Relation between topological edge invariants and exceptional points

The existence of topologically distinct phases of matter was one of the most profound discoveries of theoretical physics in recent decades [39]. The idea of classifying bandstructures using topological invariants, such as the Chern number [91], arose originally in the study of the quantum Hall effect [3], and subsequently led to the discovery of two- and three-dimensional topologically insulating materials. It has also inspired numerous proposals and experiments for realizing topologically non-trivial bands using light [8], sound [114–116], and other types of waves. According to the topological bulk-edge correspondence principle [117], topologically nontrivial bandstructures imply the existence of topologically-protected edge states, whose unique transport properties may have applications in many fields.

Theories of bandstructure topology typically assume that the underlying system is Hermitian. Yet in settings such as topological photonics, non-Hermitian effects—in the form of gain (wave amplification) and/or loss (wave dissipation)—are easily introduced, and may be both substantial and unavoidable in practical implementations [79]. Broadly speaking, non-Hermiticity poses two problems for standard theories. Firstly, non-Hermitian bands can exhibit exceptional points (EPs) [96, 118] in which case bands cease to be continuously single-valued throughout k-space, which is conceptually troublesome for band invariants such as Chern numbers. Secondly, standard formulations of the bulk-edge correspondence principle rely on

the existence of a real spectral gap in the bulk. For instance, in Hatsugai's well-known derivation of the correspondence between quantum Hall edge states and Chern numbers, it is crucial to assume that a system in a strip geometry has a *real* point spectrum which converges, in the large-system limit, to an integer number of real bands [46].

A number of recent works [103, 119–124] have started to explore how band topological ideas might be extended to non-Hermitian systems. Notably, certain special one- and two-dimensional non-Hermitian lattices have been found to exhibit topological invariants with meaningful bulk-edge correspondences [103, 124]. Some of these novel invariants are based on the winding numbers associated with EPs of the complex band spectrum, as these constitute a natural class of discrete features tied to non-Hermiticity. So far, however, it has been unclear whether there is a connection between invariants based on EP winding numbers and the standard topological invariants previously developed for Hermitian systems.

In this chapter, I describe a theoretical and experimental investigation which reveals a relationship between a Hermitian topological invariant and EP winding numbers. The topological invariant comes from a "topological pump" [104, 107, 108], and consists of the winding numbers of scattering matrix eigenvalues during a pumping cycle [52]. The bulk-edge correspondence principle associates a zero (nonzero) winding number with a topologically trivial (nontrivial) bulk bandgap. Strictly speaking, however, topologically nontrivial behavior can emerge only in the $N \to \infty$ limit, where N is the sample width (i.e., in the limit where opposite edges of the sample are decoupled). We show that when the topological pump is generalized to non-Hermitian lattices, the condition allowing for nonzero windings is

$$|\gamma| \gtrsim e^{-N}, \tag{3.1}$$

where γ parameterizes the non-Hermiticity (gain/loss) in each unit cell. In the Hermitian case ($|\gamma| \to 0$), Eq. (3.1) is satisfied when $N \to \infty$. For non-Hermitian systems ($\gamma \neq 0$), nonzero windings can occur for finite N; moreover, they emerge from a pair of EPs of the non-unitary scattering matrix.

These ideas are realized and confirmed by experiments on a classical electromagnetic network in a topological pumping configuration [104, 107, 108], operating in the microwave frequency range (900 MHz). In the previous chapter, we have shown

that such a network, constructed from radio frequency (RF) cables, couplers, and phase shifters, can be used to implement a topological pump [52]. The windings of the scattering matrix eigenvalues, during a pumping cycle, were found to match the underlying bandstructure of the network, which could be topologically trivial or nontrivial. In the present experiment, we introduce gain to the system using tunable amplifiers, allowing the level of non-Hermiticity to be controlled. This allows us to probe for the theoretically-predicted EPs, and study their effects on the topological pump.

3.1 Exceptional points and topological pumping

We begin with a theoretical analysis of a 2D square-lattice network of directed links joined by nodes, shown in Fig. 3.1(a). Steady-state waves propagating in the links are described by complex scalar amplitudes; at each node, the input and output amplitudes are related by a 2×2 coupling matrix. As shown in Section 2.4, if all links have line delay ϕ, wave propagation in an infinite periodic network is described by the Floquet equation

$$U(k)|\psi(k)\rangle = e^{-i\phi}|\psi(k)\rangle. \tag{3.2}$$

For a Bloch state with real crystal wave-vector k, $|\psi(k)\rangle$ denotes a vector of wave amplitudes exiting the nodes of one unit cell in the network, and $U(k)$ describes the "scattering" of the wave by the unit cell. Eq. (3.2) thus describes a Floquet bandstructure, with $\phi(k)$ as a quasienergy.

The network is "Hermitian" if there is no gain or loss, so that all propagation and scattering processes are unitary. Then $U(k)$ is unitary, and the Floquet Hamiltonian $H_F(k) = i \log[U(k)]$ is Hermitian. Moreover, the quasienergies $\phi(k)$ are real, and the bandstructure can be topologically trivial or non-trivial, depending on system parameters like nodal coupling strengths. (In fact, the topologically non-trivial phase is an "anomalous Floquet insulator", with interesting properties that have been studied in previous works [51, 75, 76, 111, 125–128]).

A topological edge invariant can be formulated for the network by truncating it in the y direction to form a strip N cells wide. Dirichlet boundary conditions are imposed on the upper and lower edges, so that no waves enter or leave via these

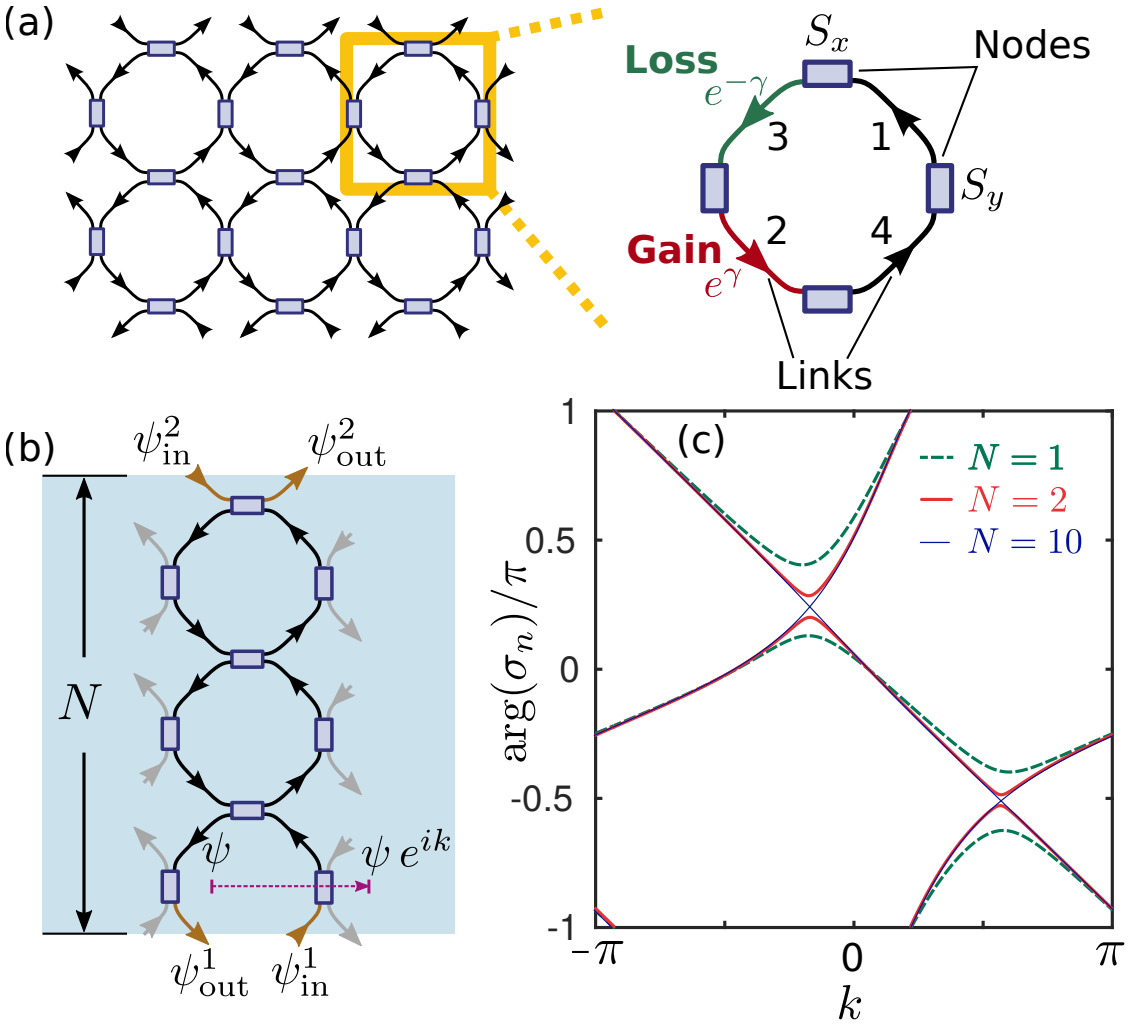

FIGURE 3.1: (a) Schematic of a periodic network of directed links and nodes, with tunable gain and loss in two of the links in each unit cell. (b) Schematic of the setup for the Laughlin-Brouwer topological pump. The network is truncated to N unit cells in the y direction, and twisted boundary conditions are applied in the x direction with tunable twist angle k (corresponding to an infinite strip with fixed wavenumber). (c) Plot of $\arg(\sigma_n)$ versus k, where $\{\sigma_n\}$ are the eigenvalues of the edge scattering matrix. Model parameters are $\gamma = 0$ (Hermitian case), $\theta_x = \theta_y = 3\pi/8$, $\Phi^3_x = \Phi^3_y = -7\pi/10$, and $\phi = 2\pi/5$.

edges. Translational invariance in x gives a conserved wave-number k, equivalent to taking one unit cell along x and imposing twisted boundary conditions. One can then calculate the bandstructure $\phi(k)$, and count the net number of edge states on each edge and in each bandgap. This is a topological invariant, independent of the choice of truncation direction for the strip [46].

Another way to formulate a topological edge invariant is the Laughlin-Brouwer *topological pump* [104, 107, 108]. As shown in Fig. 3.1(b), instead of imposing

Dirichlet boundary conditions on the edges, we attach scattering leads. The wave amplitudes incident on the two edges, $|\psi_{\text{in}}\rangle$, can be related to the output amplitudes $|\psi_{\text{out}}\rangle$ by

$$|\psi_{\text{out}}\rangle = S_{\text{edge}}|\psi_{\text{in}}\rangle \ . \tag{3.3}$$

If the network is Hermitian, S_{edge} is unitary and its eigenvalues $\{\sigma_n\}$ lie on the complex unit circle. To perform topological pumping, we set ϕ in a bandgap and advance k by 2π, and then count the resulting winding number of the σ_n's along the unit circle [107, 108].

Fig. 3.1(c) plots $\arg(\sigma_n)$ versus k for various strip widths N in Hermitian case ($\gamma = 0$). All the other system parameters are chosen so that the underlying bulk bandstructure is topologically *nontrivial* and $\phi \in \mathbb{R}$ lies in a bandgap. We find that for small N, the individual eigenvalues have *zero* winding around the origin during one cycle of the pumping parameter k. This is because, strictly speaking, nonzero windings only appear in the $N \to \infty$ limit [107, 108]. In Fig. 3.2(a), we plot $\Delta \equiv \min\big|\arg[\sigma_1(k)] - \arg[\sigma_2(k)]\big|$, where the minimum is calculated over $k \in [-\pi, \pi]$, for various finite N. This quantifies the minimum separation between the two eigenvalue trajectories, and must vanish if the eigenvalues cross somewhere in $k \in [-\pi, \pi]$, as is necessary for nonzero winding. We see that $\Delta \sim \exp(-N)$, reaching zero only for $N \to \infty$. Physically, this reflects the fact that topological protection is spoiled by the coupling of edge states on opposite edges of the sample; since edge state wavefunctions decay exponentially into the bulk, the coupling strength decreases exponentially with N.

What is the effect of the above topological pumping process on a non-Hermitian network? To study this problem, we focus on non-Hermitian networks with a specific distribution of gain and loss, shown in Fig. 3.1(a): in each unit cell, link 2 has gain factor $\exp(\gamma)$, link 3 has loss factor $\exp(-\gamma)$, and the other links remain unitary. Thus, γ simultaneously tunes gain and loss in links 2 and 3. This arrangement of gain and loss is chosen so that exceptional points (EPs) of the system are easily accessible. In a more symmetric configuration, where links 1 and 3 have balanced gain and loss, and/or links 2 and 4 have balanced gain and loss; with this choice, the network is $\mathcal{PT}$ (parity-time) symmetric [129–132]. However, the edge invariant is unaffected by the non-Hermiticity providing that the introduced gain and loss are $\mathcal{PT}$-symmetric. For this reason, we focus on non-Hermitian networks shown in Fig. 3.1(a), which do not possess $\mathcal{PT}$-symmetry. Using these non-unitary

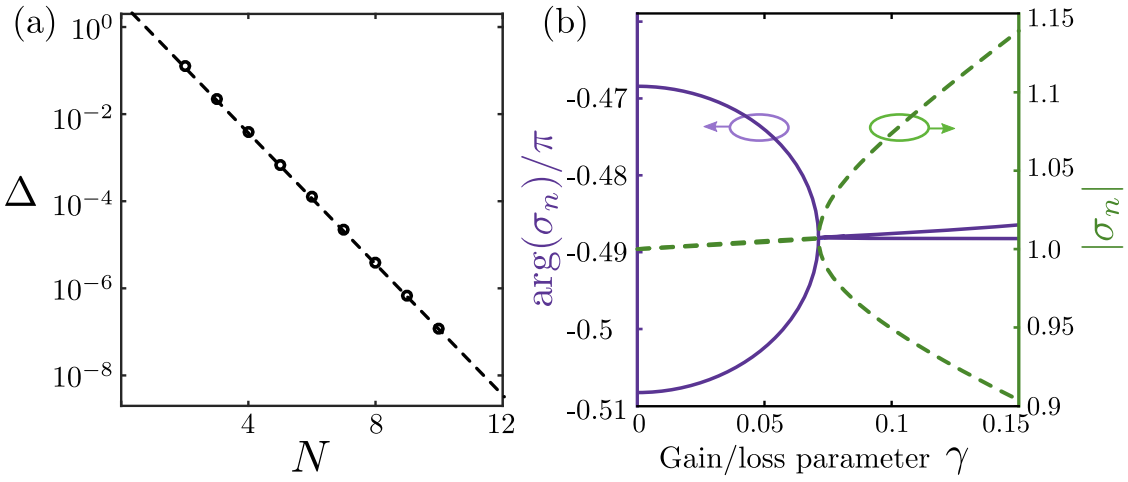

FIGURE 3.2: (a) The gaps between arguments of scattering matrix eigenvalues: $\Delta \equiv \min(|\arg(\sigma_1) - \arg(\sigma_2)|)$ in the Hermitian limit $\gamma = 0$. The circles represent gaps for different N, and the dashline is fit-line in the semilog plot. (b) The non-Hermitian scattering matrix eigenvalues of the 2D network at $k_{ep} \simeq 0.572\pi$ and $N = 2$. The argument and amplitude of the eigenvalues are read from the left and right axes, respectively. The other model parameters are same as in Fig. 3.1 (c): $\theta_x = \theta_y = 3\pi/8$, $\Phi_x^3 = \Phi_y^3 = -7\pi/10$, and $\phi = 2\pi/5$.

S_{edge} matrices, we can fix ϕ and γ, and carry out the "pumping" procedure as before: advance k by 2π, and examine how the trajectories of $\{\sigma_n\}$ wind in the complex plane.

Doing so reveals an interesting feature of the non-Hermitian pump: nonzero windings can occur for *finite* N, due to the existence of EPs of the non-unitary S_{edge} matrix. An EP is a point in a 2D parameter space where a matrix becomes defective and its eigenvectors become linearly dependent; [96, 118] due to the spectral theorem, EPs only appear in non-Hermitian systems. In Fig. 3.2(b), we plot $\arg(\sigma_n)$ and $|\sigma_n|$ against the gain/loss parameter γ, for $N = 2$ and $k = 0.572\pi$. The two eigenvalues exhibit bifurcative behavior characteristic of an EP, coalescing at $\gamma = 0.071$. In this case, S_{edge} possesses a pair of EPs in the 2D parameter space formed by k and γ; one EP is located at $(k = 0.572\pi, \gamma = 0.071)$, as seen in Fig. 3.2(b), while the other EP is located at $(k = -0.1731\pi, \gamma = 0.1132)$.

Fig. 3.3 illustrates how the EPs give rise to the topologically nontrivial regime of the topological pump. Fig. 3.3(a) shows the 2D parameter space, with the gain/loss parameter γ serving as the radial coordinate and the cyclic pumping parameter k serving as the azimuthal coordinate. The two EPs of S_{edge} are labeled EP1 and

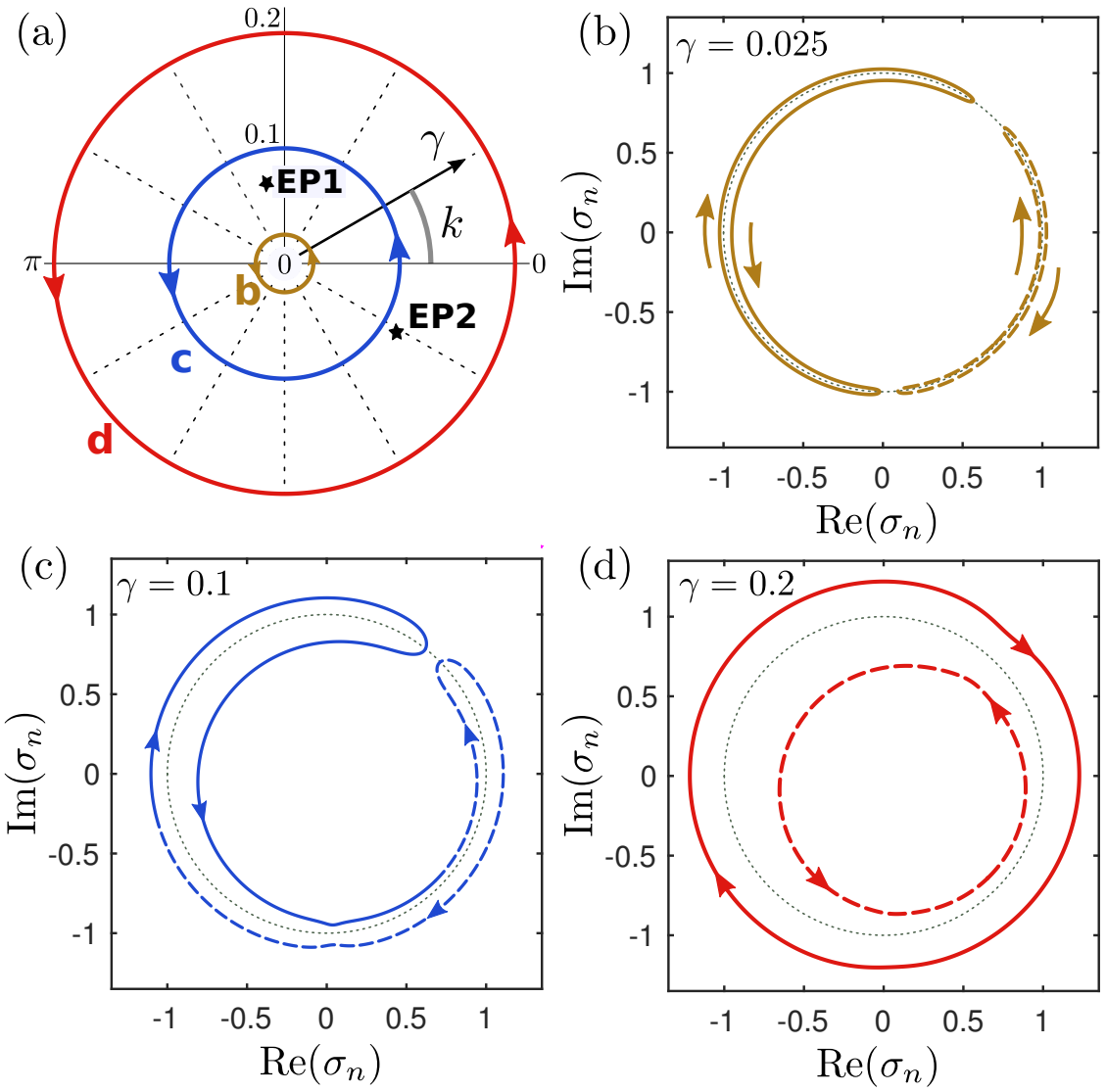

FIGURE 3.3: Relationship between topological pumping and exceptional points, calculated for a network model of width $N = 2$. The underlying band-structure is topologically nontrivial, with ϕ in a bandgap ($\theta_x = \theta_y = 3\pi/8$, $\Phi_x^3 = \Phi_y^3 = -0.7\pi$, and $\phi = 2\pi/5$). (a) Parametric loops in the 2D parameter space formed by the gain/loss parameter γ (radial coordinate) and pumping parameter k (azimuthal coordinate). Exceptional points of S_{edge} are indicated by stars. (b, c, d) Complex plane trajectories of $\{\sigma_n\}$, the eigenvalues of S_{edge}, corresponding to the parametric loops shown in (a). The two distinct eigenvalue trajectories are plotted as solid and dashed curves, and the unit circle is plotted as dots for comparison. The trajectories in (b) have zero winding around the origin, like the Hermitian finite-N limit; the trajectories in (c) join each other under one cycle, because the parametric loop encloses one exceptional point; the trajectories in (d) have nonzero windings, similar to the Hermitian large-N limit.

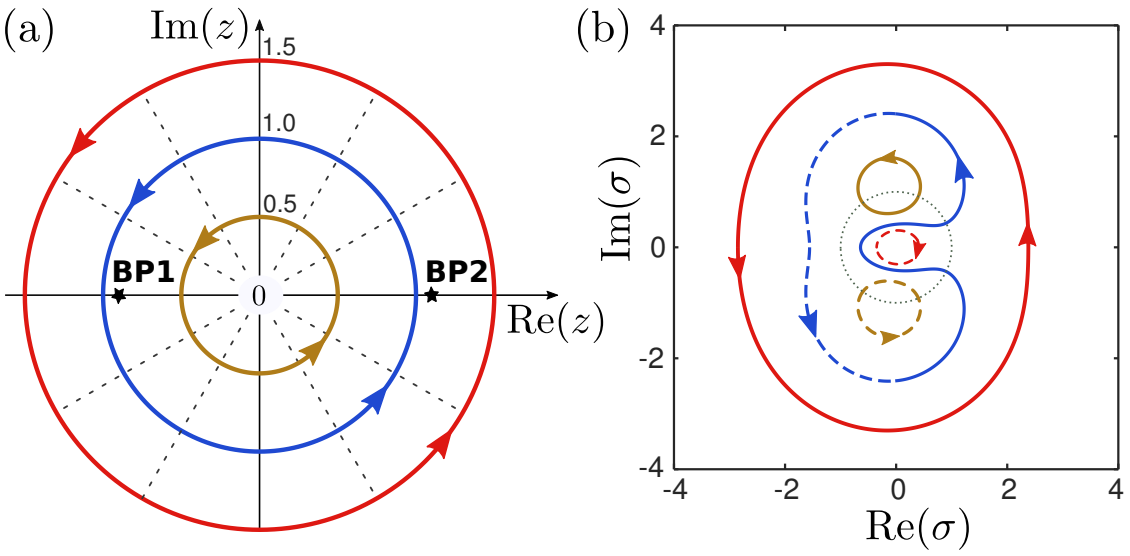

FIGURE 3.4: Behavior of the multi-valued function $\sigma(z)$ given by Eq. (3.4), illustrating how branch points can produce winding and non-winding trajectories. Here, we take $\alpha = 0.1$. (a) Plot of the parameter space formed by the complex variable z, with the branch points of $\sigma(z)$ indicated by stars, along with three parametric loops corresponding to (i) $|z| = 0.5$, (ii) $|z| = 1$, and (iii) $|z| = 1.5$. (b) The corresponding complex plane trajectories of the two branches of $\sigma(z)$.

EP2 (these EP positions depend on N, which is set here to $N = 2$). In Fig. 3.3(b)–(d), we plot the trajectories of $\{\sigma_n\}$ in the complex plane, as the system proceeds along the different parametric loops indicated in Fig. 3.3(a). For a parametric loop at small γ, not enclosing any EP, the eigenvalue trajectories do not wind around the origin, as shown in Fig. 3.3(b). This behavior extends down to the previously-discussed Hermitian limit ($\gamma = 0$). For a parametric loop at large γ, enclosing both EPs, the eigenvalue trajectories have nonzero windings, as shown in Fig. 3.3(d), and is similar to the large-N limit of the Hermitian topological pump. Between these two regimes, there are two points in the parameter space where the eigenvalue trajectories cross, which are EPs of S_{edge}. Fig. 3.3(c) shows the intermediate regime where only one EP is enclosed by the parametric loop. In this case, one pumping cycle induces a continuous exchange of the two eigenvalues, along with their eigenvectors [96].

We can use a simple model to illustrate how such a mathematical relationship between EPs and eigenvalue windings might arise. Consider the multi-valued function

$$\sigma(z) = z - \alpha + \sqrt{(z - \alpha + 1)(z - \alpha - 1)}. \tag{3.4}$$

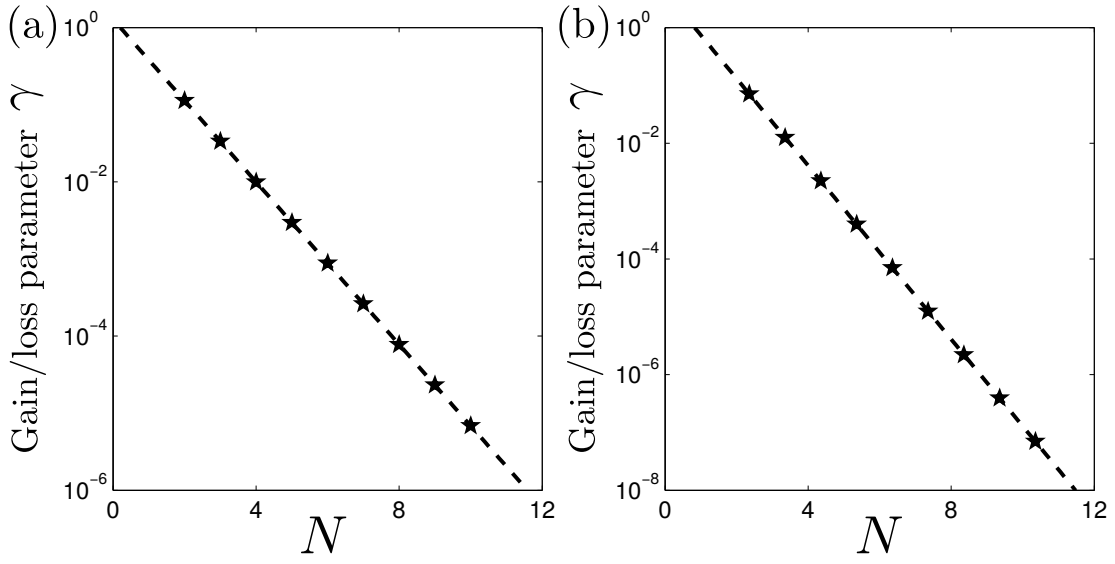

FIGURE 3.5: The gain/loss parameter γ at the EP positions versus N: (a) one of the two EPs labeled EP1, (b) another EP labeled EP2. The pentagons represent γ for different N, and the dashline is fit-line in the semilog plot.

The two branches of $\sigma(z)$, arising from the square root, could represent solutions to a secular equation for the eigenvalues of a 2×2 matrix, parameterized analytically by a variable z; the branch points, $z = \alpha \pm 1$, are EPs of that matrix. Fig. 3.4(a) shows three different loops in the parameter space, centered at $z = 0$ and enclosing zero, one, and two branch points, similar to Fig. 3.3(a). In Fig. 3.4(b), we plot the trajectories of $\sigma(z)$ corresponding to those parametric loops, and observe winding behaviors very similar to Fig. 3.3(b)–(d). In particular, for $|z| \to 0$, branches of Eq. (3.4) reduce to $\sigma_{\pm}(z) \approx -\alpha \pm \sqrt{\alpha^2 - 1}$, exhibiting zero winding during one cycle of $\arg(z)$; whereas for $|z| \to \infty$, the branches reduce to $\sigma_{\pm}(z) = (2z)^{\pm 1}$, which wind in opposite directions around the origin.

The above discussion implies that the topologically nontrivial regime of the Hermitian topological pump[104, 107, 108] emerges from the general behavior of the non-Hermitian topological pump by taking an appropriate order of limits. For given finite N, nonzero windings require sufficiently large γ, as expressed in Eq. (3.1). In Fig. 3.5, we plot the gain/loss parameter γ at the EP positions versus N. With increasing N, the required level of non-Hermiticity decreases exponentially, reaching zero for $N \to \infty$.

In Hatsugai's derivation of the correspondence between quantum Hall edge states

and Chern numbers, the energy eigenvalues of a strip system are analytically continued to complex energies. And the complex energy surface defines the Riemann surface obtained by gluing the two Riemann spheres at branch cuts along which real energy bands sit. The winding number of edge state on the complex energy surface counts the intersection number with the branch cuts, and the correspondence basically says the bulk band Chern number equals the difference between winding numbers above the band top and below the band bottom. The correspondence is derived in the large-system limit. The relationship between a Hermitian topological invariant and EP winding numbers we found is different from Hatsugai's. Firstly, the EP winding number is strictly tied to a non-Hermitian system, as the branch points correspond to the EPs. Secondly, the relationship applies to systems of finite-size, where opposite edges are not completely decoupled.

3.2 Implementation of the experiment

In order to realize the non-Hermitian topological pump, the experiment setup described in chapter 2 was redesigned. The basic setup is shown in Fig. 3.6. Overall, this network is designed according to the topological pumping configuration shown in Fig. 3.1(b). It corresponds to a "column" of the periodic network of width N, composed of identical unit cells each containing four links and two nodes. Fig. 3.6(b) is the schematic of a single cell in our experiment, the cell structure here is the same as the one in our previous experiment in Chapter 2. The difference between our redesigned experiment implementation and previous one in Chapter 2 is the design of the link. In our previous implementation, upper links in each cell are just one RF cable and lower links are one RF cable add one phase shifter. However, in our new experiment implementation, each directional link consists of five low-loss hand-flex coaxial RF cables (086-10SM+/086-15SM+, Mini-Circuits), a bandpass filter (CBC-893+, Mini-Circuits), an isolator (S0091IAD, Nova Microwave), a phase shifter (SPHSA-152+, Mini-Circuits), and a digitally-controlled variable-gain amplifier (DVGA1-242+, Mini-Circuits). Fig. 3.7 presents the picture of the components. These chip-based components are much smaller compared to the ones used in previous experiment which enable us to build a three cells system and add tunable gain and loss to the system.

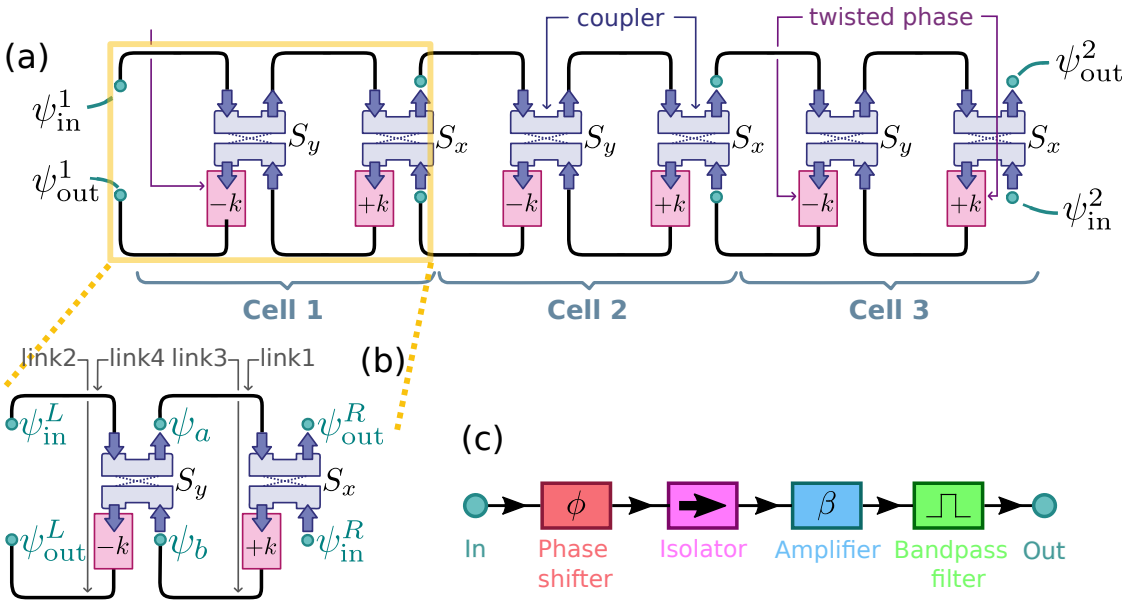

FIGURE 3.6: (a) Experimental setup. Each of the identical units, labeled "Cell 1", "Cell 2" and "Cell 3," corresponds to one cell in the topological pump geometry. The twisted boundary condition is applied by tuning phase shifter (pink boxes) in lower links. The couplers (blue rods) are depicted in the strong-coupling configuration. The weak-coupling configuration is achieved by swapping each coupler's outputs. The overall input and output amplitudes are $\psi^{1,2}_{\text{in}}$ and $\psi^{1,2}_{\text{out}}$. Their scattering parameters are measured with a network analyzer. (b) Each cell is composed of four links ($j = 1, 2, 3, 4$) and two couplers (S_x, S_y). (c) Every link in our system are exactly the same and contain one phase shifter, one isolator, one digital controlled variable gain amplifier, one bandpass filter and five low-loss handflex interconnect coaxial RF cables.

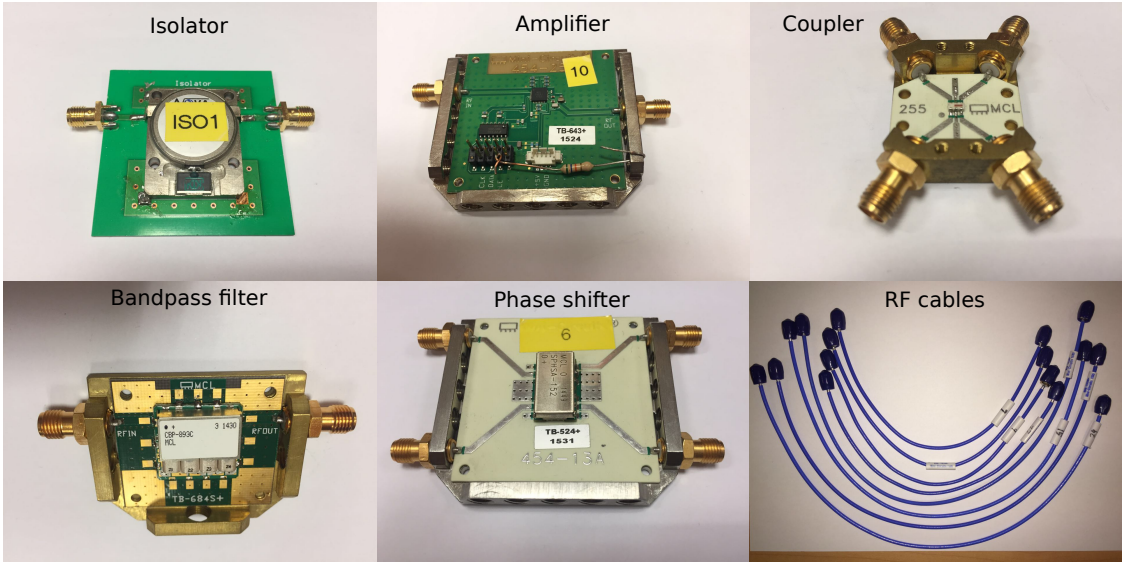

FIGURE 3.7: Photographes of components in our experiment.

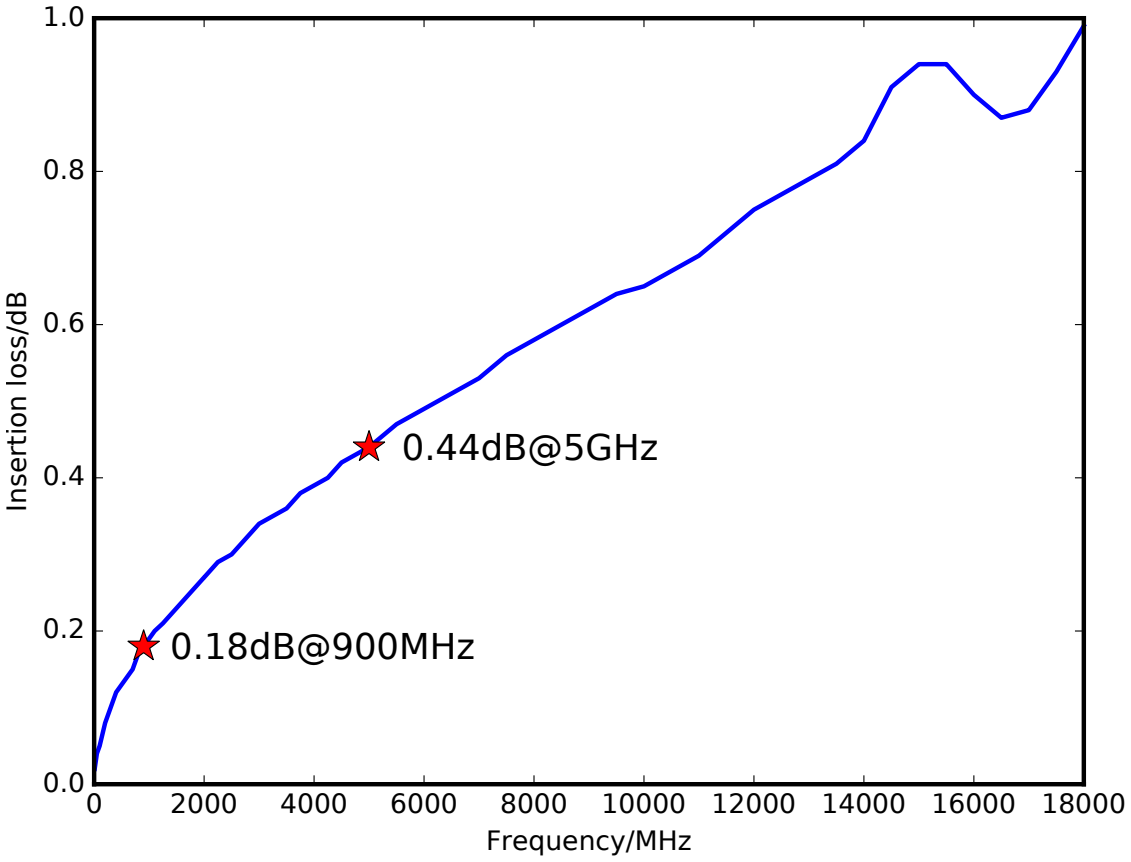

FIGURE 3.8: Insertion loss of 086-10SM+ from Mini-Circuits, data taken from official website of Mini-Circuits.

Based on this new design, the link's transmission coefficient, $t = \beta \exp(i\varphi)$, can be independently tuned in both phase and amplitude. The phase $\varphi \in [0, 2\pi)$ is controlled by the phase shifter with $\pm 1^\circ$ precision, and is used to set the network model quasienergy ϕ and the pumping parameter k. The gain/loss factor β is tunable in the range $[-8\,\mathrm{dB}, 24\,\mathrm{dB}]$ with $\pm 0.25\,\mathrm{dB}$ precision. The $-8\,\mathrm{dB}$ lower bound corresponds to turning off the amplifier, and comes from the intrinsic losses of the components. In our new experiment, the frequency is chosen to be 900 MHz rather than 5 GHz as in our previous experiment in chapter 2, because the loss of same waveguide is positively related to the frequency. Fig. 3.8 presents the insertion loss of one RF cable —086-10SM+, the insertion loss of this cable is 0.18 dB at 900 MHz and 0.44 dB at 5 GHz, which means one cable can introduce an additional 0.26 dB loss at 5 GHz compared to 900 MHz. As a result, to decrease the losses in the system, we decided to implement the experiment at 900 MHz where all the components works well and satisfies experiment requirements.

In each cell, each node consists of an RF coupler (BDCN-7-25+, Mini-Circuits) with $\approx 1:7$ coupling ratio. At 900 MHz, its measured S parameters are

$$S_{\text{coupler}} = \begin{bmatrix} 0.914e^{-i0.622\pi} & 0.348e^{-i0.127\pi} \\ 0.348e^{-i0.127\pi} & 0.914e^{-i0.622\pi} \end{bmatrix}. \tag{3.5}$$

By swapping the order of the output ports, we can realize both topologically trivial and nontrivial phases of the network model's underlying bandstructure [52]. In terms of the coupling parameter θ, this means we can set $\theta \approx 0.12\pi$ (weak-coupling/trivial) or $\theta \approx 0.38\pi$ (strong-coupling/nontrivial), where $\theta = 0.5\pi$ is the topological transition point.

To measure the edge scattering matrix, S_{edge}, we attach the inputs and outputs at the ends of the "column" to a vector network analyzer (Anritsu 37396C). In order to get the winding behavior of the eigenvalues of the S_{edge}, the status of upper links are set to a fixed point (fixed β and φ), the status of lower links are sweeped in a desired range (β is controlled to near a chosen valued with precision of ± 0.25dB while φ is sweeping in the range $[0, 2\pi)$ with precision of $\pm 1^\circ$ to generate $\pm k$). Here, the sweeping step of phase is 10° and 37 points are measured. At each point, we use the analyzer to measure $S_{11}, S_{12}, S_{21}, \text{and} S_{22}$ and finally give us the results of S_{edge}.

3.3 Results

Fig. 3.9 shows the results when $\beta \approx 1$ (i.e., with the amplifiers are tuned so that there is no net gain or loss in each link). In this case, S_{edge} is approximately unitary, and as expected the eigenvalues lie very close to the complex unit circle. Under one cycle of k, we observe no winding in the weak-coupling case. In the strong-coupling case, nonzero windings appear only when the system size is sufficiently large, as shown in Fig. 3.9(d). This is consistent with the results shown in Chapter 2 and with the theoretical discussion of Section 3.1.

Next, we seek to observe the effects of the EPs on the non-Hermitian topological pump, as discussed theoretically in Section 3.1. This is accomplished by selectively applying amplification to some of the links, according to the gain/loss distribution shown in Fig. 3.1(a). The results are shown in Fig. 3.10 for the $N = 2$ case. The

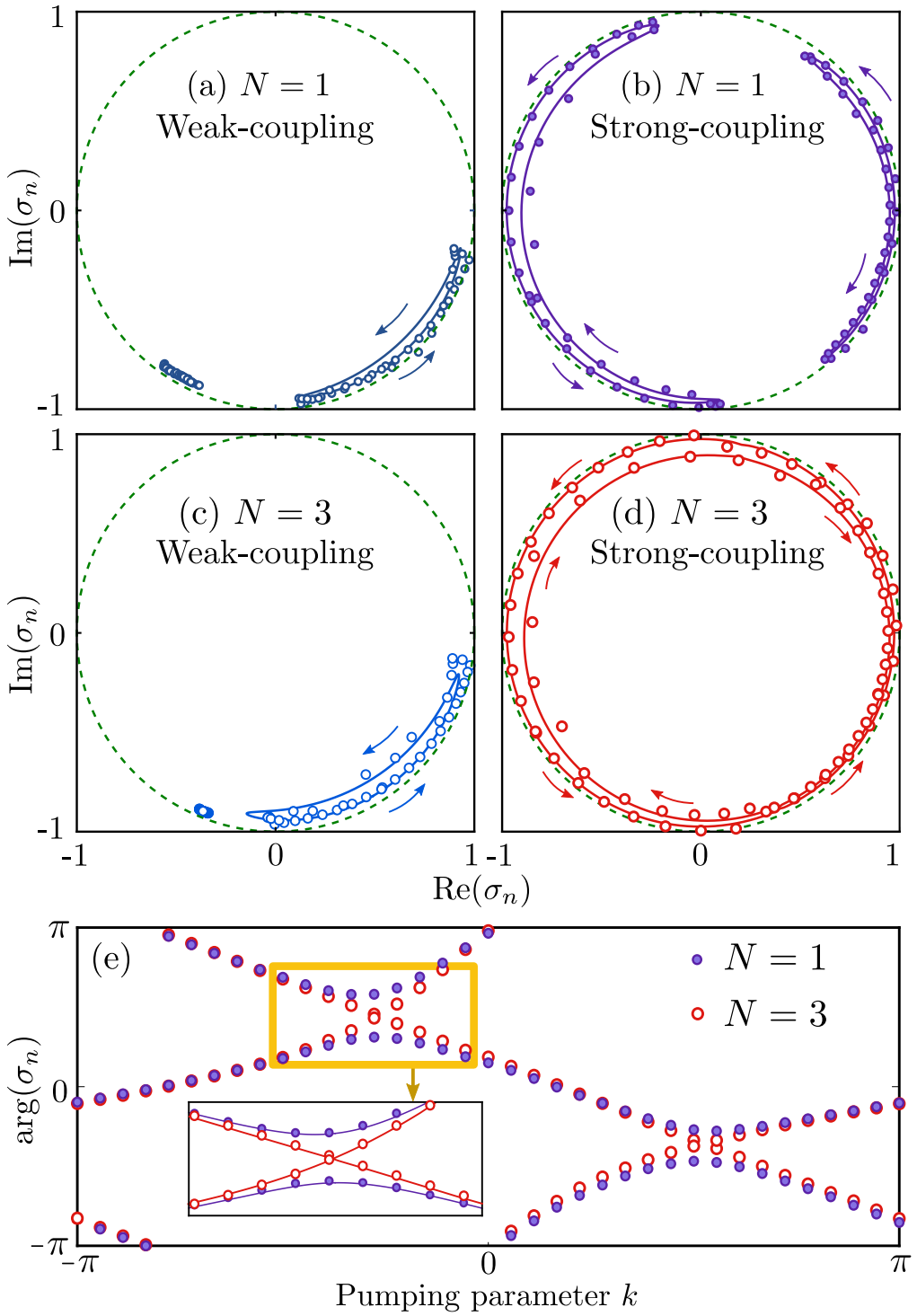

FIGURE 3.9: (a)–(d) Experimentally measured scattering matrix eigenvalues over one pumping cycle, with approximately zero gain/loss. Results are shown for (a,b) $N = 1$ and (c,d) $N = 3$. The weak-coupling regime corresponds to a topologically trivial phase of the underlying network bandstructure, while the strong-coupling regime corresponds to a topologically nontrivial phase. The unit circle is indicated with dashes. (e) Arguments of the measured scattering matrix eigenvalues, $\arg(\sigma_n)$, versus pumping parameter k. Inset: behavior near a crossing point; solid curves show theoretical results calculated using the network components' measured S-parameters, which predict an avoided crossing for $N = 1$ and a crossing for $N = 3$.

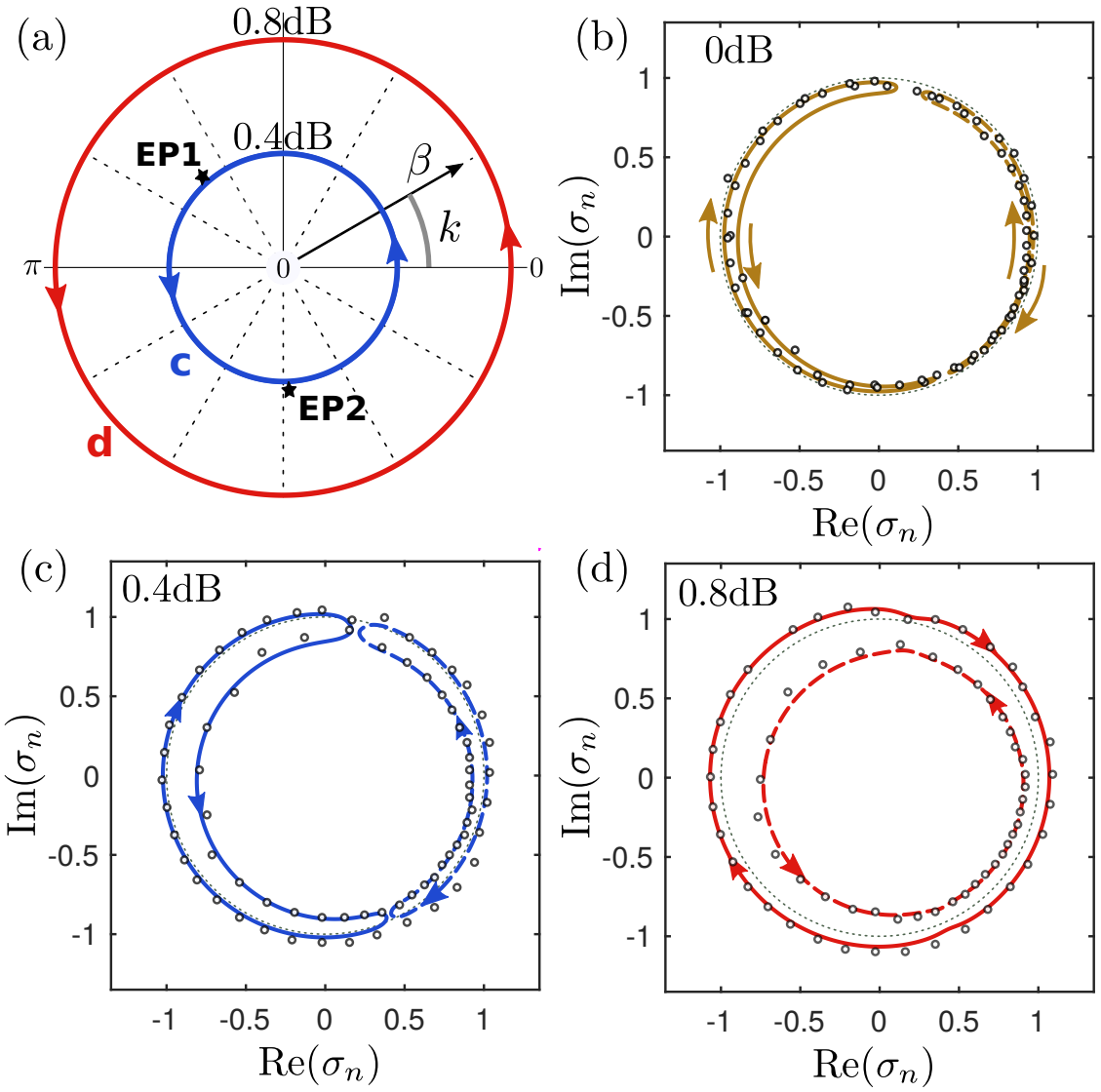

FIGURE 3.10: (a) Parametric loops in the 2D parameter space formed by the gain/loss factor β (radial coordinate) and pumping parameter k (azimuthal coordinate). Exceptional points indicated by stars are calculated based on measured S_{coupler}, see Eq. (3.5). Scatteringvmatrix eigenvalues measured across two cells in series. In each cell, the links are labeled from 1∼4 as shown in 3.6 "Cell 3". Gain is added to link 2 and loss is applied to link 3 in each cell. Link 1 and link 4 are kept almost ideal. The value for gain and loss is exactly the same and equal to β. The β value are 0dB, 0.4dB and 0.8dB for (b), (c), (d) respectively. The two gaps between two curves decrease as we increase the value of β and finally disappear as β larger than a critical value.

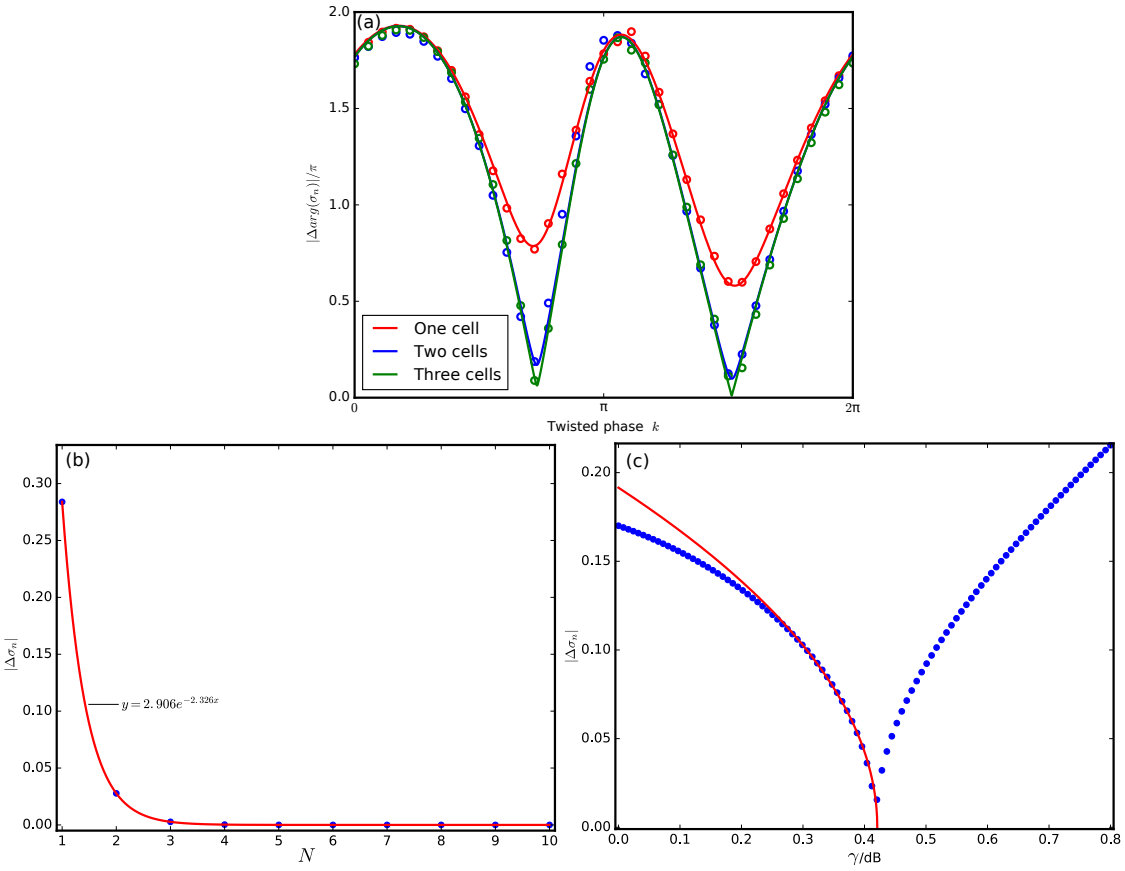

FIGURE 3.11: (a) The distance between the arguments of scattering matrix eigenvalues, the results comes from the experiments when $\beta \approx 1$. (b) Relation between gap width ($|\delta\sigma_n|$) and system scale. (c) Relation between gap width ($|\delta\sigma_n|$) and gain/loss (γ).

subplot (a) shows the parameter loops in the 2D parameter space with exceptional points. The two exceptional points are quite close to the pumping cycle with the gain/loss factor $\beta = 0.4$dB, which makes it difficult to verify the intermediate regime (only one EP is enclosed by the parametric loop) in experiment. In all three subplots (b), (c), and (d), the measured scattering matrix eigenvalues fit the simulated results well.

3.4 Discussion

3.4.1 Gaps

From the discussion in Section 3.1, we know, rigorous speaking, it is impossible for us to observe the winding behavior in our system model because a gap will always

occur in a finite Hermitian system. Figure. 3.11(a) presents the results of the distance between the arguments of scattering matrix eigenvalues in our experiments when $\beta \approx 1$. It is clear that there are two gaps in the eigenvalues even for the system with three cells ($N = 3$) which is consistent with the results shown in Figure. 3.9. Based on our experiment data for couplers and links, we performed simulation for a much larger system and the result is shown in Figure. 3.11(b). We found that the gap width ($|\Delta\sigma_n|$) will drop exponentially as system scale (N) increases but that there will always be a gap. As seen in Fig. 3.10, this gap disappears once the network is sufficiently non-Hermiticity. Figure. 3.11(c) presents the relation between gap width ($|\Delta\sigma_n|$) and gain/loss amplitude (γ). It can be found out that as γ becomes larger, the gap becomes smaller at first, then closed at a particular value (EP), and thereafter the eigenvalue curves remain gapless for increasing γ. This trend in the gap width matches the results shown in Figure. 3.10 well. Therefore, by introducing EPs by adding gain/loss, it is possible for us to demonstrate the winding behavior of an non-Hermitian Floquet topological non-trivial system.

3.4.2 Transmission properties

For a topological non-trivial system, if the system is large enough, the S_{edge} matrix will evolve into two reflections and the transmission from one edge to another edge will become negelectable. Figure. 3.12 presents the transmission (S_{12}) in our system. For small scale systems, both experiment data and simulation data are shown and they match quite well. For large scale system ($N > 3$), simulation results are presented and it is clear that the transmission drops quickly as system scale grows. This result proves that our system can be considered to truly remain in the topologically non-trivial phase.

3.5 Summary

In this chapter, following my previous research to measure a topological edge invariant as shown in Chapter 2, I tried to improve the performance of our system by adding gain to compensate the intrinsic loss introduced by microwave components. However, during my research, I found out that theoretically it is impossible to observe rigorously nonzero topological winding numbers design. Fortunately,

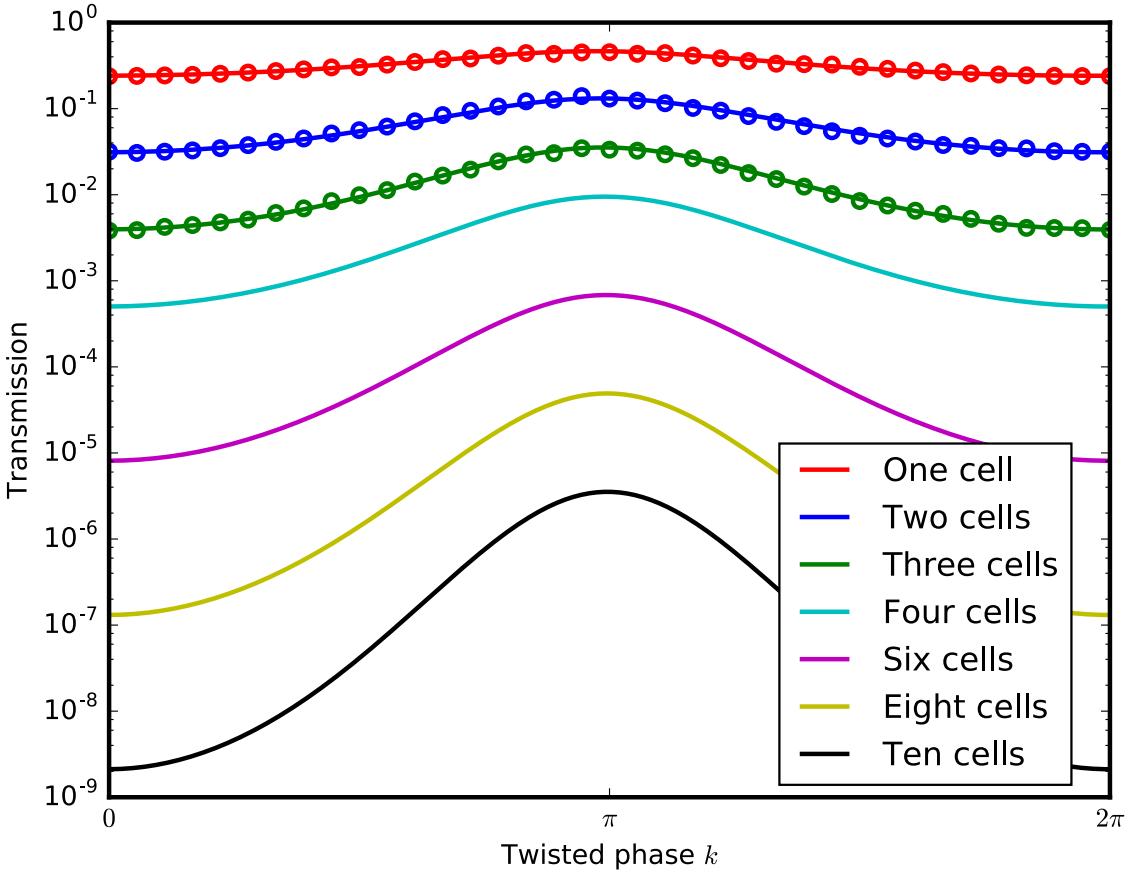

FIGURE 3.12: Transmission from one edge to another edge in our system. Empty circles are experiment data points for one cell, two cells, and three cells system, solid curves are simulation results.

with the new design of our experiment model, it is quite easy for us to control gain and loss in each link in the system. In this way, exceptional points can be easily introduced into our system and we discovered that a relation exists between these topological edge invarants and exceptional points. With more in-depth investigation, we proved both theoretically and experimentally that an interesting connection exists between these two invariants and it is possible to observe non-zero winding behavior of system scatter eigenvalues in a non-Hermitian system.

Chapter 4

Conclusion

4.1 Background

During past several decades, topological insulator is one of the most profound discoveries in theoretical physics [2, 8, 39]. They are "topologically distinct" from conventional insulators, being insulating in the 'bulk' while supporting metallic states on the surfaces. The most extraordinary physical property is the existence, in 2D topological insulators, of uni-directional transmission along the edge, which is robust to imperfections and has no back-reflection. This striking phenomenon has attracted a lot of research attention to topological insulators, and may have future device applications.

The concept of topology originated from mathematical research on preserved properties of space under continuous deformations. In each topological space, the preserved properties can be characterized using a topological invariant. In the early 1980s, the first topological insulator was discovered in the quantum Hall effect and the topological invariants that describe these systems is known as the "Chern number", defined as the integration of the Berry curvature [133] over a 2D Brillouin zone. Topological insulators have bands with non-zero "Chern number" whereas in conventional insulators, all bands have zero "Chern number".

In the earliest topological insulators, strong magnetic fields were required to break the time-reversal symmetry of the system [4] and bring the system into a topological phase. In 1988, Haldane make a breakthrough in this area by theoretically proposed

a topological system without net magnetic flux penetrating through the system [6]. In around 2004, the quantum spin Hall effect [9–11] was discovered, and in 2005, Kane and Mele [12] made a key theoretical breakthrough by finding a new type of topological invariant which can be used to classify topological invariants of systems with time-reversal symmetry. In 2006, the topological insulator idea was brought into 3D systems [15–18]. In 2008, Hsieh discovered the first 3D topological insulator, the alloy Bi_xSb_{1-x} [19, 20].

The idea of band topology was introduced into photonics and the branch of photonic topological insulator was developed [8]. In 2007, the first experimental realization of a photonic topological insulator was reported, showing the existence of robust uni-directional transmission line [54, 55]. In 2011, Hafezi suggested a photonic topological network model without magnetic flux [47] and experimentally implemented it [48]. In 2013, Chong introduced a similar network model which can exhibit topological phase under certain conditions [49]; the topologically nontrivial phase is known as a Floquet topological insulator. A Floquet topological insulator is slightly different from normal topological insulator found in quantum Hall effects. The net "Chern number" of each band is zero but it will become non-zero at both the upper side and lower side of the band which enables the gapless bandstructure of the system.

4.2 Our work and its significance

In all the above works on photonic topological insulators, the observation of uni-directional transmission serves as the only method to judge whether a system is in a topological phase or not. This is because photonic systems lack a direct analog of the Hall conductance or similar linear response-based quantity. In order to provide an alternative method to show the existence of topological nontrivial band structure, we borrow the "topological pump" idea proposed by Laughlin [104], map the photonic topological system into a two-ports network which provide us a new platform to do research in this area.

The topic of my PhD is investigation of two dimensional Floquet topological insulator using microwave networks. This research has fallen into two major sub-topics.

First, based on Chong's previous theoretical research [49, 51] on the Floquet topological insulator, we found it is possible to map such network model into a two-ports netork. In this two-ports network system, all the required condition can be realized in microwave region. Fixed phase delay ϕ can be implemented using RF transmission cable, variable phase twist k can be realized using tunable phase shifter, and coupling between resonators can be applied by bi-directional microwave couplers. The designed network system can be built by connecting all these components together and the S matrix of the system can be measured using a network analyzer. In this way, a edge invariant of this topological system can be measured in the form of winding numbers of the eigenvalues of the S matrix. In our work, a two-cells system is built and winding behavior is successfully observed when the system is in topological non-trivial state and this is the first experimental measurement of a topological edge invariant in photonic topological insulator.

In my first experiment to measure a topological edge invariant in a microwave network, plenty of weaknesses exist in my system and the most extraordinary one is the loss in the system. In order to improve the performance of the system, the experiment setup is redesigned. All the links in the system contains one amplifier and one phase shifter which makes all links tunable in both phase and amplitude. In this way, we not only compensate the intrinsic losses introduced by the components but also enable us to control the gain/loss state of each link in the system. Another drawback of our experiment setup is the system scale which is limited to two cells due to components size. Rigorous speaking, it is impossible to observe the truly non-zero winding behavior in a finite system because there will always be a gap in the eigenvalue curves. The gap width of the gap will decrease exponentially as the system size goes up and hence the gap will become neglectable even for a small system such as two or three cells. Fortunately, we found it is possible to introduce exceptional points into the system and the interaction between topological edge invariant and exceptional points can eliminate the gap in eigenvalue curves and realize the truly non-zero winding in a finite system. These exceptional points are generated by adding gain and loss to system links. In this work, we built a two cells system and apply reasonable gain/loss to each link. By measuring the S matrix of the system, a truly non-zero winding behavior has been observed when the system is in topological non-trivial state. In this work, we demonstrate, theoretically and experimentally, a direct relationship between a Hermitian topological invariant and exceptional point winding numbers.

In summary, three major contribution has been made to the area photonic topological insulator. At first, we map the periodic photonic topological structure into a two-ports network system, which provides a new platform to study the system properties in this area. Then, we successfully measuring an topological edge invariant in this system which demonstrate the existence of topological nontrivial band structure in original system. This work provide a complete new method for the research in this area. At last, we introduce exceptional points into the system by balanced gain and loss and we demonstrate a direct relation between topological edge invariant and exceptional points by both simulation and experiment. This work proves that our platform can be used to investigate not only topological edge invariant but also exceptional points together which make it more powerful in this area.

4.3 Future works

Following current work, there are several topics worth to be investigated. First, the network model of Floquet topological insulator has various forms including square-lattice [49] and hexagon-lattice [51]. The hexagon-lattice is very similar to the square-lattice we used and it should be possible to realize a similar experiment for a hexagon-lattice. In hexagon-lattice, there are more tunable parameters which will give us more freedom and enable richer choices to play with the system. Second, the system scale of our experiment is limited to at most three-cells width network, but larger system such as ten cells can give a more robust results for our observation, is it possible to realize a much larger system in other method, for example, in a printed circuit board rather than using separated microwave components? Third, our initial idea to realize this experiment is in optical region. Unfortunately, it fails because the vibration amplitude is comparable to optical wavelength which breaks the resonating in the system. We are still wondering is it possible to realize a stable photonic topological system in optical frequency which enable us to measure its topological edge invariants? Fourth, all of our work are finished in two-dimension, but currently, the hottest research topic are focused on three-dimensional system, is it possible to bring our system into three-dimension by layering the system up as described in Wang's paper [126] ? Is there any method to prove the existence of Weyl point in this kind of system by experiment? Fifth, so many theoretical

works has been accomplished for two-dimensional and three-dimensional topological insulators. In all these works, plenty of models has been proposed to realize topological phase and many of them has been experimentally implemented. until today, when we talk about topological insulator, we know it is a new phase of material and it has striking characters such as uni-directional edge transmission line for two-dimensional system and Fermi arc for three-dimensional system. However, no practical applications has been reported for topological insulators. Maybe it is time for us to think more about how to apply these phenomenon features of topological insulator to makes our world better.

Author's Publications

Journal Articles

- **Hu Wenchao** et.al., *Measurement of a topological edge invariant in a microwave network*, Phy. Rev. X **5**, 011012 (2015). **Impact factor: 8.701**.
- **Hu Wenchao** et.al., *All-optical implementation of the ant colony optimization algorithm*, Sci. Rep. **6** (2016). **Impact facotr: 5.228**.
- **Hu Wenchao** et.al., *Exceptional point effects in a non-Hermitian topological pump*, Phy. Rev. B. **95** (18), 184306 (2017). **Impact factor: 3.718**.

Conference Proceedings

- **Hu Wenchao** et.al., *Using nonlinear optical networks for optimization: primer of the ant colony algorithm*, CLEO:QELS_Fundamental Science, FM1D–8 (2014).
- **Hu Wenchao** et.al., *Photons as ants: a stigmergic photonic network*, The European Conference on Lasers and Electro-Optics, CI_P_2 (2015).

Bibliography

[1] Topology, January 2017. URL `https://en.wikipedia.org/wiki/Topology`.

[2] Joel E Moore. The birth of topological insulators. *Nature*, 464(7286):194–198, 2010.

[3] Michael Stone. *Quantum Hall Effect*. World Scientific, 1992.

[4] Robert B Laughlin. Anomalous quantum hall effect: an incompressible quantum fluid with fractionally charged excitations. *Physical Review Letters*, 50 (18):1395, 1983.

[5] Michael Stone. Schur functions, chiral bosons, and the quantum-hall-effect edge states. *Physical Review B*, 42(13):8399, 1990.

[6] F Duncan M Haldane. Model for a quantum hall effect without landau levels: Condensed-matter realization of the" parity anomaly". *Physical Review Letters*, 61(18):2015, 1988.

[7] Gordon W Semenoff. Condensed-matter simulation of a three-dimensional anomaly. *Physical Review Letters*, 53(26):2449, 1984.

[8] Ling Lu, John D Joannopoulos, and Marin Soljačić. Topological photonics. *Nature Photonics*, 8(11):821–829, 2014.

[9] Shuichi Murakami, Naoto Nagaosa, and Shou-Cheng Zhang. Spin-hall insulator. *Physical review letters*, 93(15):156804, 2004.

[10] B Andrei Bernevig and Shou-Cheng Zhang. Quantum spin hall effect. *Physical Review Letters*, 96(10):106802, 2006.

[11] Xiao-Liang Qi and Shou-Cheng Zhang. The quantum spin hall effect and topological insulators. *Physics Today*, 63(1):33–38, 2010.

[12] Charles L Kane and Eugene J Mele. Z 2 topological order and the quantum spin hall effect. *Physical review letters*, 95(14):146802, 2005.

[13] B Andrei Bernevig, Taylor L Hughes, and Shou-Cheng Zhang. Quantum spin hall effect and topological phase transition in hgte quantum wells. *Science*, 314(5806):1757–1761, 2006.

[14] Markus König, Steffen Wiedmann, Christoph Brüne, Andreas Roth, Hartmut Buhmann, Laurens W Molenkamp, Xiao-Liang Qi, and Shou-Cheng Zhang. Quantum spin hall insulator state in hgte quantum wells. *Science*, 318(5851): 766–770, 2007.

[15] Liang Fu, Charles L Kane, and Eugene J Mele. Topological insulators in three dimensions. *Physical Review Letters*, 98(10):106803, 2007.

[16] Joel E Moore and Leon Balents. Topological invariants of time-reversal-invariant band structures. *Physical Review B*, 75(12):121306, 2007.

[17] Rahul Roy. Topological phases and the quantum spin hall effect in three dimensions. *Physical Review B*, 79(19):195322, 2009.

[18] Ying Ran, Yi Zhang, and Ashvin Vishwanath. One-dimensional topologically protected modes in topological insulators with lattice dislocations. *Nature Physics*, 5(4):298–303, 2009.

[19] David Hsieh, Dong Qian, Lewis Wray, YuQi Xia, Yew San Hor, RJ Cava, and M Zahid Hasan. A topological dirac insulator in a quantum spin hall phase. *Nature*, 452(7190):970–974, 2008.

[20] David Hsieh, Y Xia, L Wray, Dong Qian, A Pal, JH Dil, J Osterwalder, F Meier, G Bihlmayer, CL Kane, et al. Observation of unconventional quantum spin textures in topological insulators. *Science*, 323(5916):919–922, 2009.

[21] Y Xia, Dong Qian, David Hsieh, L Wray, A Pal, Hsin Lin, Arun Bansil, DHYS Grauer, YS Hor, RJ Cava, et al. Observation of a large-gap topological-insulator class with a single dirac cone on the surface. *Nature Physics*, 5(6): 398–402, 2009.

[22] Haijun Zhang, Chao-Xing Liu, Xiao-Liang Qi, Xi Dai, Zhong Fang, and Shou-Cheng Zhang. Topological insulators in bi2se3, bi2te3 and sb2te3 with a single dirac cone on the surface. *Nature physics*, 5(6):438–442, 2009.

[23] YL Chen, JG Analytis, J-H Chu, ZK Liu, S-K Mo, Xiao-Liang Qi, HJ Zhang, DH Lu, Xi Dai, Zhong Fang, et al. Experimental realization of a three-dimensional topological insulator, bi2te3. *Science*, 325(5937):178–181, 2009.

[24] AH Castro Neto, F Guinea, Nuno MR Peres, Kostya S Novoselov, and Andre K Geim. The electronic properties of graphene. *Reviews of modern physics*, 81(1):109, 2009.

[25] Pedram Roushan, Jungpil Seo, Colin V Parker, YS Hor, David Hsieh, Dong Qian, Anthony Richardella, M Zahid Hasan, RJ Cava, and Ali Yazdani. Topological surface states protected from backscattering by chiral spin texture. *Nature*, 460(7259):1106–1109, 2009.

[26] Zhanybek Alpichshev, JG Analytis, J-H Chu, Ian R Fisher, YL Chen, Zhi-Xun Shen, Alan Fang, and Aharon Kapitulnik. Stm imaging of electronic waves on the surface of bi 2 te 3: topologically protected surface states and hexagonal warping effects. *Physical review letters*, 104(1):016401, 2010.

[27] Tong Zhang, Peng Cheng, Xi Chen, Jin-Feng Jia, Xucun Ma, Ke He, Lili Wang, Haijun Zhang, Xi Dai, Zhong Fang, et al. Experimental demonstration of topological surface states protected by time-reversal symmetry. *Physical Review Letters*, 103(26):266803, 2009.

[28] Kentaro Nomura, Mikito Koshino, and Shinsei Ryu. Topological delocalization of two-dimensional massless dirac fermions. *Physical review letters*, 99 (14):146806, 2007.

[29] Philip W Anderson. Absence of diffusion in certain random lattices. *Physical review*, 109(5):1492, 1958.

[30] Jian Li, Rui-Lin Chu, JK Jain, and Shun-Qing Shen. Topological anderson insulator. *Physical review letters*, 102(13):136806, 2009.

[31] CW Groth, M Wimmer, AR Akhmerov, J Tworzydło, and CWJ Beenakker. Theory of the topological anderson insulator. *Physical review letters*, 103 (19):196805, 2009.

[32] David Hsieh, Y Xia, Dong Qian, L Wray, JH Dil, F Meier, J Osterwalder, L Patthey, JG Checkelsky, NP Ong, et al. A tunable topological insulator in the spin helical dirac transport regime. *Nature*, 460(7259):1101–1105, 2009.

[33] Babak Seradjeh, JE Moore, and Marcel Franz. Exciton condensation and charge fractionalization in a topological insulator film. *Physical review letters*, 103(6):066402, 2009.

[34] Hailin Peng, Keji Lai, Desheng Kong, Stefan Meister, Yulin Chen, Xiao-Liang Qi, Shou-Cheng Zhang, Zhi-Xun Shen, and Yi Cui. Aharonov-bohm interference in topological insulator nanoribbons. *Nature materials*, 9(3): 225–229, 2010.

[35] Yi Zhang, Ke He, Cui-Zu Chang, Can-Li Song, Li-Li Wang, Xi Chen, Jin-Feng Jia, Zhong Fang, Xi Dai, Wen-Yu Shan, et al. Crossover of the three-dimensional topological insulator bi2se3 to the two-dimensional limit. *Nature Physics*, 6(8):584–588, 2010.

[36] Ion Garate and Marcel Franz. Inverse spin-galvanic effect in the interface between a topological insulator and a ferromagnet. *Physical review letters*, 104(14):146802, 2010.

[37] K v Klitzing, Gerhard Dorda, and Michael Pepper. New method for high-accuracy determination of the fine-structure constant based on quantized hall resistance. *Physical Review Letters*, 45(6):494, 1980.

[38] D Co Tsui and AC Gossard. Resistance standard using quantization of the hall resistance of gaas-alxga1- xas heterostructures. *Applied Physics Letters*, 38(7):550–552, 1981.

[39] M Zahid Hasan and Charles L Kane. Colloquium: topological insulators. *Reviews of Modern Physics*, 82(4):3045, 2010.

[40] Xiao-Liang Qi and Shou-Cheng Zhang. Topological insulators and superconductors. *Reviews of Modern Physics*, 83(4):1057, 2011.

[41] FDM Haldane and S Raghu. Possible realization of directional optical waveguides in photonic crystals with broken time-reversal symmetry. *Physical review letters*, 100(1):013904, 2008.

[42] S Raghu and FDM Haldane. Analogs of quantum-hall-effect edge states in photonic crystals. *Physical Review A*, 78(3):033834, 2008.

[43] John D Joannopoulos, Steven G Johnson, Joshua N Winn, and Robert D Meade. *Photonic crystals: molding the flow of light*. Princeton university press, 2011.

[44] Mikio Nakahara. *Geometry, topology and physics*. CRC Press, 2003.

[45] Winding number, January 2017. URL `https://en.wikipedia.org/wiki/Winding_number`.

[46] Yasuhiro Hatsugai. Chern number and edge states in the integer quantum hall effect. *Physical review letters*, 71(22):3697, 1993.

[47] Mohammad Hafezi, Eugene A Demler, Mikhail D Lukin, and Jacob M Taylor. Robust optical delay lines with topological protection. *Nature Physics*, 7(11): 907–912, 2011.

[48] Mohammad Hafezi, S Mittal, J Fan, A Migdall, and JM Taylor. Imaging topological edge states in silicon photonics. *Nature Photonics*, 7(12):1001–1005, 2013.

[49] GQ Liang and YD Chong. Optical resonator analog of a two-dimensional topological insulator. *Physical review letters*, 110(20):203904, 2013.

[50] GQ Liang and YD Chong. Optical resonator analog of a photonic topological insulator: a finite-difference time-domain study. *International Journal of Modern Physics B*, 28(02):1441007, 2014.

[51] Michael Pasek and YD Chong. Network models of photonic floquet topological insulators. *Physical Review B*, 89(7):075113, 2014.

[52] Wenchao Hu, Jason C Pillay, Kan Wu, Michael Pasek, Perry Ping Shum, and YD Chong. Measurement of a topological edge invariant in a microwave network. *Physical Review X*, 5(1):011012, 2015.

[53] JT Chalker and PD Coddington. Percolation, quantum tunnelling and the integer hall effect. *Journal of Physics C: Solid State Physics*, 21(14):2665, 1988.

[54] Zheng Wang, YD Chong, John D Joannopoulos, and Marin Soljačić. Reflection-free one-way edge modes in a gyromagnetic photonic crystal. *Physical review letters*, 100(1):013905, 2008.

[55] Zheng Wang, Yidong Chong, JD Joannopoulos, and Marin Soljačić. Observation of unidirectional backscattering-immune topological electromagnetic states. *Nature*, 461(7265):772–775, 2009.

[56] YD Chong, Xiao-Gang Wen, and Marin Soljačić. Effective theory of quadratic degeneracies. *Physical Review B*, 77(23):235125, 2008.

[57] Kejie Fang, Zongfu Yu, and Shanhui Fan. Microscopic theory of photonic one-way edge mode. *Physical Review B*, 84(7):075477, 2011.

[58] Scott A Skirlo, Ling Lu, and Marin Soljačić. Multimode one-way waveguides of large chern numbers. *Physical review letters*, 113(11):113904, 2014.

[59] Yin Poo, Rui-xin Wu, Zhifang Lin, Yan Yang, and CT Chan. Experimental realization of self-guiding unidirectional electromagnetic edge states. *Physical review letters*, 106(9):093903, 2011.

[60] Kexin Liu, Linfang Shen, and Sailing He. One-way edge mode in a gyromagnetic photonic crystal slab. *Optics letters*, 37(19):4110–4112, 2012.

[61] Ara A Asatryan, Lindsay C Botten, Kejie Fang, Shanhui Fan, and Ross C McPhedran. Local density of states of chiral hall edge states in gyrotropic photonic clusters. *Physical Review B*, 88(3):035127, 2013.

[62] Cheng He, Xiao-Lin Chen, Ming-Hui Lu, Xue-Feng Li, Wei-Wei Wan, Xiao-Shi Qian, Ruo-Cheng Yin, and Yan-Feng Chen. Tunable one-way cross-waveguide splitter based on gyromagnetic photonic crystal. *Applied Physics Letters*, 96(11):111111, 2010.

[63] Xiaofei Zang and Chun Jiang. Edge mode in nonreciprocal photonic crystal waveguide: manipulating the unidirectional electromagnetic pulse dynamically. *JOSA B*, 28(3):554–557, 2011.

[64] Jin-Xin Fu, Rong-Juan Liu, and Zhi-Yuan Li. Robust one-way modes in gyromagnetic photonic crystal waveguides with different interfaces. *Applied Physics Letters*, 97(4):041112, 2010.

[65] Wenjun Qiu, Zheng Wang, and Marin Soljačić. Broadband circulators based on directional coupling of one-way waveguides. *Optics express*, 19(22):22248–22257, 2011.

[66] Yan Yang, Yin Poo, Rui-xin Wu, Yan Gu, and Ping Chen. Experimental demonstration of one-way slow wave in waveguide involving gyromagnetic photonic crystals. *Applied Physics Letters*, 102(23):231113, 2013.

[67] Fengnian Xia, Lidija Sekaric, and Yurii Vlasov. Ultracompact optical buffers on a silicon chip. *Nature photonics*, 1(1):65–71, 2007.

[68] Brent E Little, JS Foresi, G Steinmeyer, ER Thoen, ST Chu, HA Haus, EP Ippen, LC Kimerling, and W Greene. Ultra-compact si-sio 2 microring resonator optical channel dropping filters. *IEEE Photonics Technology Letters*, 10(4):549–551, 1998.

[69] Andrea Melloni and Mario Martinelli. Synthesis of direct-coupled-resonators bandpass filters for wdm systems. *Journal of Lightwave Technology*, 20(2): 296–303, 2002.

[70] Atsushi Sakai, Tatsuhiko Fukazawa, and Toshihiko Baba. Estimation of polarization crosstalk at a micro-bend in si-photonic wire waveguide. *Journal of lightwave technology*, 22(2):520, 2004.

[71] Pieter Dumon, Wim Bogaerts, Vincent Wiaux, Johan Wouters, Stephan Beckx, Joris Van Campenhout, Dirk Taillaert, Bert Luyssaert, Peter Bienstman, Dries Van Thourhout, et al. Low-loss soi photonic wires and ring resonators fabricated with deep uv lithography. *IEEE Photonics Technology Letters*, 16(5):1328–1330, 2004.

[72] Yurii Vlasov and Sharee McNab. Losses in single-mode silicon-on-insulator strip waveguides and bends. *Optics express*, 12(8):1622–1631, 2004.

[73] Qianfan Xu, Bradley Schmidt, Sameer Pradhan, and Michal Lipson. Micrometre-scale silicon electro-optic modulator. *nature*, 435(7040):325–327, 2005.

[74] Mikael C Rechtsman, Julia M Zeuner, Yonatan Plotnik, Yaakov Lumer, Daniel Podolsky, Felix Dreisow, Stefan Nolte, Mordechai Segev, and Alexander Szameit. Photonic floquet topological insulators. *Nature*, 496(7444): 196–200, 2013.

[75] Takuya Kitagawa, Erez Berg, Mark Rudner, and Eugene Demler. Topological characterization of periodically driven quantum systems. *Physical Review B*, 82(23):235114, 2010.

[76] Netanel H Lindner, Gil Refael, and Victor Galitski. Floquet topological insulator in semiconductor quantum wells. *Nature Physics*, 7(6):490–495, 2011.

[77] Victor I Kopp, Victor M Churikov, Jonathan Singer, Norman Chao, Daniel Neugroschl, and Azriel Z Genack. Chiral fiber gratings. *Science*, 305(5680): 74–75, 2004.

[78] Shu Jia and Jason W Fleischer. Nonlinear light propagation in rotating waveguide arrays. *Physical Review A*, 79(4):041804, 2009.

[79] Fei Gao, Zhen Gao, Xihang Shi, Zhaoju Yang, Xiao Lin, Hongyi Xu, John D Joannopoulos, Marin Soljačić, Hongsheng Chen, Ling Lu, et al. Probing topological protection using a designer surface plasmon structure. *Nature communications*, 7, 2016.

[80] Jean Dalibard, Fabrice Gerbier, Gediminas Juzeliūnas, and Patrik Öhberg. Colloquium: Artificial gauge potentials for neutral atoms. *Reviews of Modern Physics*, 83(4):1523, 2011.

[81] Dieter Jaksch and Peter Zoller. Creation of effective magnetic fields in optical lattices: the hofstadter butterfly for cold neutral atoms. *New Journal of Physics*, 5(1):56, 2003.

[82] Michael Schmidt, Vittorio Peano, and Florian Marquardt. Optomechanical metamaterials: Dirac polaritons, gauge fields, and instabilities. *arXiv preprint arXiv:1311.7095*, 2013.

[83] Ningyuan Jia, Clai Owens, Ariel Sommer, David Schuster, and Jonathan Simon. Time reversal invariant topologically insulating circuits. *arXiv preprint arXiv:1309.0878*, 2013.

[84] Wen-Jie Chen, Zhi Hong Hang, Jian-Wen Dong, Xiao Xiao, He-Zhou Wang, and CT Chan. Observation of backscattering-immune chiral electromagnetic modes without time reversal breaking. *Physical review letters*, 107(2):023901, 2011.

[85] Ling Lu, John D Joannopoulos, Marin Soljačić, et al. Waveguiding at the edge of a three-dimensional photonic crystal. *Physical review letters*, 108(24): 243901, 2012.

[86] AA Burkov, MD Hook, and Leon Balents. Topological nodal semimetals. *Physical Review B*, 84(23):235126, 2011.

[87] Steve M Young, Saad Zaheer, Jeffrey CY Teo, Charles L Kane, Eugene J Mele, and Andrew M Rappe. Dirac semimetal in three dimensions. *Physical review letters*, 108(14):140405, 2012.

[88] Xiangang Wan, Ari M Turner, Ashvin Vishwanath, and Sergey Y Savrasov. Topological semimetal and fermi-arc surface states in the electronic structure of pyrochlore iridates. *Physical Review B*, 83(20):205101, 2011.

[89] Ling Lu, Zhiyu Wang, Dexin Ye, Lixin Ran, Liang Fu, John D Joannopoulos, and Marin Soljačić. Experimental observation of weyl points. *Science*, 349 (6248):622–624, 2015.

[90] Hongming Weng, Chen Fang, Zhong Fang, B Andrei Bernevig, and Xi Dai. Weyl semimetal phase in noncentrosymmetric transition-metal monophosphides. *Physical Review X*, 5(1):011029, 2015.

[91] DJ Thouless, Mahito Kohmoto, MP Nightingale, and M Den Nijs. Quantized hall conductance in a two-dimensional periodic potential. *Physical Review Letters*, 49(6):405, 1982.

[92] Sunil Mittal, Sriram Ganeshan, Jingyun Fan, Abolhassan Vaezi, and Mohammad Hafezi. Measurement of topological invariants in a 2d photonic system. *Nature Photonics*, 2016.

[93] Mohammad Hafezi. Measuring topological invariants in photonic systems. *Physical Review Letters*, 112(21):210405, 2014.

[94] Mark J Ablowitz and Athanassios S Fokas. *Complex variables: introduction and applications*. Cambridge University Press, 2003.

[95] Riemann surface, January 2017. URL `https://en.wikipedia.org/wiki/Riemann_surface`.

[96] WD Heiss. The physics of exceptional points. *Journal of Physics A: Mathematical and Theoretical*, 45(44):444016, 2012.

[97] WD Heiss. Exceptional points of non-hermitian operators. *Journal of Physics A: Mathematical and General*, 37(6):2455, 2004.

[98] WD Heiss and HL Harney. The chirality of exceptional points. *The European Physical Journal D-Atomic, Molecular, Optical and Plasma Physics*, 17(2): 149–151, 2001.

[99] Dieter Heiss. Mathematical physics: Circling exceptional points. *Nature Physics*, 2016.

[100] Tosio Kato. *Perturbation theory for linear operators*, volume 132. Springer Science & Business Media, 2013.

[101] Jörg Doppler, Alexei A Mailybaev, Julian Böhm, Ulrich Kuhl, Adrian Girschik, Florian Libisch, Thomas J Milburn, Peter Rabl, Nimrod Moiseyev, and Stefan Rotter. Dynamically encircling exceptional points in a waveguide: asymmetric mode switching from the breakdown of adiabaticity. *Nature*, 537 (7618):76–79, 2016.

[102] Haitan Xu, David Mason, Luyao Jiang, and JGE Harris. Topological energy transfer in an optomechanical system with exceptional points. *Nature*, 537 (7618):80–83, 2016.

[103] Tony E Lee. Anomalous edge state in a non-hermitian lattice. *Physical review letters*, 116(13):133903, 2016.

[104] Robert B Laughlin. Quantized hall conductivity in two dimensions. *Physical Review B*, 23(10):5632, 1981.

[105] Amnon Yariv, Yong Xu, Reginald K Lee, and Axel Scherer. Coupled-resonator optical waveguide:? a proposal and analysis. *Optics letters*, 24 (11):711–713, 1999.

[106] Douglas R Hofstadter. Energy levels and wave functions of bloch electrons in rational and irrational magnetic fields. *Physical review B*, 14(6):2239, 1976.

[107] PW Brouwer. Scattering approach to parametric pumping. *Physical Review B*, 58(16):R10135, 1998.

[108] Dganit Meidan, Tobias Micklitz, and Piet W Brouwer. Topological classification of adiabatic processes. *Physical Review B*, 84(19):195410, 2011.

[109] Takashi Oka and Hideo Aoki. Photovoltaic hall effect in graphene. *Physical Review B*, 79(8):081406, 2009.

[110] Jun-ichi Inoue and Akihiro Tanaka. Photoinduced transition between conventional and topological insulators in two-dimensional electronic systems. *Physical review letters*, 105(1):017401, 2010.

[111] Takuya Kitagawa, Mark S Rudner, Erez Berg, and Eugene Demler. Exploring topological phases with quantum walks. *Physical Review A*, 82(3):033429, 2010.

[112] Zhenghao Gu, HA Fertig, Daniel P Arovas, and Assa Auerbach. Floquet spectrum and transport through an irradiated graphene ribbon. *Physical review letters*, 107(21):216601, 2011.

[113] Mark S Rudner, Netanel H Lindner, Erez Berg, and Michael Levin. Anomalous edge states and the bulk-edge correspondence for periodically driven two-dimensional systems. *Physical Review X*, 3(3):031005, 2013.

[114] Zhaoju Yang, Fei Gao, Xihang Shi, Xiao Lin, Zhen Gao, Yidong Chong, and Baile Zhang. Topological acoustics. *Physical review letters*, 114(11):114301, 2015.

[115] Romain Fleury, Alexander B Khanikaev, and Andrea Alù. Floquet topological insulators for sound. *Nature Communications*, 7, 2016.

[116] Bryan Gin-ge Chen, Nitin Upadhyaya, and Vincenzo Vitelli. Nonlinear conduction via solitons in a topological mechanical insulator. *Proceedings of the National Academy of Sciences*, 111(36):13004–13009, 2014.

[117] B Andrei Bernevig and Taylor L Hughes. *Topological insulators and topological superconductors*. Princeton University Press, 2013.

[118] Tosio Kato. Perturbation theory for linear operators, volume 132 of grundlehren der mathematischen wissenschaften, 1966.

[119] MS Rudner and LS Levitov. Topological transition in a non-hermitian quantum walk. *Physical review letters*, 102(6):065703, 2009.

[120] Kenta Esaki, Masatoshi Sato, Kazuki Hasebe, and Mahito Kohmoto. Edge states and topological phases in non-hermitian systems. *Physical Review B*, 84(20):205128, 2011.

[121] Yi Chen Hu and Taylor L Hughes. Absence of topological insulator phases in non-hermitian p t-symmetric hamiltonians. *Physical Review B*, 84(15): 153101, 2011.

[122] CE Bardyn, MA Baranov, CV Kraus, E Rico, A İmamoğlu, P Zoller, and S Diehl. Topology by dissipation. *New Journal of Physics*, 15(8):085001, 2013.

[123] Kun Ding, ZQ Zhang, and Che Ting Chan. Coalescence of exceptional points and phase diagrams for one-dimensional p t-symmetric photonic crystals. *Physical Review B*, 92(23):235310, 2015.

[124] Daniel Leykam, Konstantin Y Bliokh, Chunli Huang, YD Chong, and Franco Nori. Edge modes, degeneracies, and topological numbers in non-hermitian systems. *arXiv preprint arXiv:1610.04029*, 2016.

[125] Clément Tauber and Pierre Delplace. Topological edge states in two-gap unitary systems: a transfer matrix approach. *New Journal of Physics*, 17 (11):115008, 2015.

[126] Hailong Wang, Longwen Zhou, and YD Chong. Floquet weyl phases in a three-dimensional network model. *Physical Review B*, 93(14):144114, 2016.

[127] Tetsuyuki Ochiai. Floquet–weyl and floquet-topological-insulator phases in a stacked two-dimensional ring-network lattice. *Journal of Physics: Condensed Matter*, 28(42):425501, 2016.

[128] Pierre Delplace, Michel Fruchart, and Clément Tauber. Phase rotation symmetry and the topology of oriented scattering networks. *arXiv preprint arXiv:1612.05769*, 2016.

[129] Carl M Bender and Stefan Boettcher. Real spectra in non-hermitian hamiltonians having p t symmetry. *Physical Review Letters*, 80(24):5243, 1998.

[130] Carl M Bender, MV Berry, and Aikaterini Mandilara. Generalized pt symmetry and real spectra. *Journal of Physics A: Mathematical and General*, 35 (31):L467, 2002.

[131] R El-Ganainy, KG Makris, DN Christodoulides, and Ziad H Musslimani. Theory of coupled optical pt-symmetric structures. *Optics letters*, 32(17): 2632, 2007.

[132] Konstantinos G Makris, Ramy El-Ganainy, Demetrios N Christodoulides, and Ziad H Musslimani. Beam dynamics in p t symmetric optical lattices. *Physical Review Letters*, 100(10):103904, 2008.

[133] Michael V Berry. Quantal phase factors accompanying adiabatic changes. In *Proceedings of the Royal Society of London A: Mathematical, Physical and Engineering Sciences*, volume 392, pages 45–57. The Royal Society, 1984.